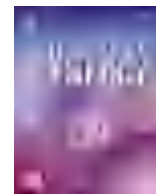


中国石油大学 (北京)

2025 年申报硕士研究生指导教师评审材料目录

[illegible]



Electronic synergy between CoP/NiCoP heterostructure and Co, Ni single atoms for efficient hydrogen evolution and overall water splitting

Hongchen Liu^{a,1}, Xingru Yan^{a,1}, Fan Yang^{a,*}, Sai Che^a, Jianfeng Wang^a, Jinxiu Qian^a, Xiaoyun Zhang^a, Siyuan Sun^a, Yang Sun^a, Ni Wu^a, Shuyang Wang^b, Yongfeng Li^{a,**}

^a State Key Laboratory of Heavy Oil Processing, China University of Petroleum, Beijing, 102249, China

^b China Petroleum Engineering & Construction Corporation Beijing Company, Beijing, 100085, China

ARTICLE INFO

Handling Editor: Dr. M. Djukic

Keywords:

Transition metal phosphides
Heterostructure
Single atomic catalysts
Heavy oil ingredient
Overall water splitting

ABSTRACT

Transition metal phosphides (TMPs) are considered as potential electrocatalysts for hydrogen evolution (HER) and overall water splitting (OWS), but their excessively strong adsorption property toward H^{*} limits the reaction kinetics. Herein, we design a bifunctional electrocatalyst (CoP/NiCoP/Co–Ni–N–C) supported by CoP/NiCoP heterostructure and Co, Ni single atoms, which was prepared via facile one-pot pyrolysis process. The interfacial electronic synergy between the high-electropositive Co–N–C, Ni–N–C and the electron-rich CoP/NiCoP heterostructure balanced the hydrogen binding strength, resulting in fast kinetics and high intrinsic activity. Besides, the g-C₃N₄ was applied as a self-sacrificial template to construct the N doped hierarchical porous carbon carrier, which provided abundant mass transfer pathways and enhanced the charge transfer efficiency. Additionally, the fluid catalytic cracking (FCC) slurry was intelligently applied as extra carbon source, which not only limited the size of CoP/NiCoP nanoparticles, but also increased the loading of Co and Ni single atoms. Benefit from those advantages, the optimized CoP/NiCoP/Co–Ni–N–C exhibited low overpotentials of 40 mV at 10 mA cm^{−2} toward HER in 1 M KOH. Meanwhile, the two-electrode system only need 1.54 V to achieve the current density of 10 mA cm^{−2}. This work provided a kind of potential electrocatalyst for efficient water splitting and a method for low-cost catalyst design.

1. Introduction

Nowadays, The global energy crisis and environmental pollution promote development of sustainable green energy [1,2]. Hydrogen, in particular, has attracted broad attention due to its large energy density and non-polluting combustion product (water) [3]. Electrocatalytic overall water splitting (OWS) is recognized as the most ideal method for hydrogen production, which consists of the cathodic hydrogen evolution reaction (HER) and the anodic oxygen evolution reaction (OER) [4]. Up to now, the noble metal-based electrocatalysts (Pt-based materials for HER and Ru/Ir-based materials for OER) are still the benchmarks for OWS, but the low reserves and high costs of the raw materials limit their scale-up applications [5]. Therefore, it is crucial to develop non-noble metal based electrocatalyst with low cost, high performance, and long-term stability for efficient OWS.

Among various active substances, transition-metal phosphides

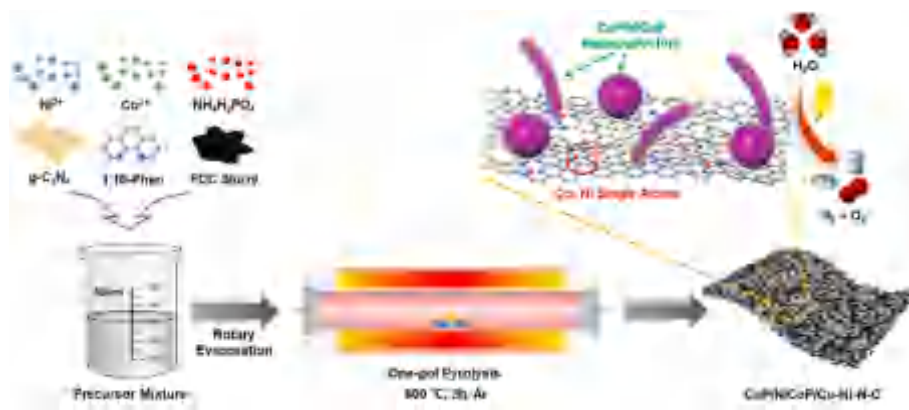
(TMPs) are emerging as one of the most promising choices for HER, owing to their high intrinsic conductivities and distinctive [NiFe] hydrogenase-like structures [6]. However, the application of pristine TMPs in bifunctional electrocatalytic OWS still suffers from the following two challenges. To be specific, TMPs always exhibit the hydrogen adsorption Gibbs free energy (ΔG_{H^*}) that less than 0, indicating the strong binding toward H^{*} and resulting in the sluggish dissociation of H₂ product and the blocking of the active sites [7,8]. Moreover, the P sites in TMPs tend to be strongly electronegative, which is not favorable for binding OH[−] and reconstitution, and thus their performances toward OER are relatively weak [9,10]. In response to these problems, many recent studies have adopted the strategy of constructing heterostructure to optimize the adsorption energy of TMPs toward reactant intermediates, enhance the electron transport efficiency and couple the active substances with high OER activities, so as to improve the bifunctional electrocatalytic OWS performances [7,11–17].

* Corresponding author.

** Corresponding author.

E-mail addresses: yangfan@cup.edu.cn (F. Yang), yfli@cup.edu.cn (Y. Li).

¹ These authors contributed equally to this work.



Scheme 1. Schematic illustration for the synthesis of CoP/NiCoP/Co-Ni-N-C.

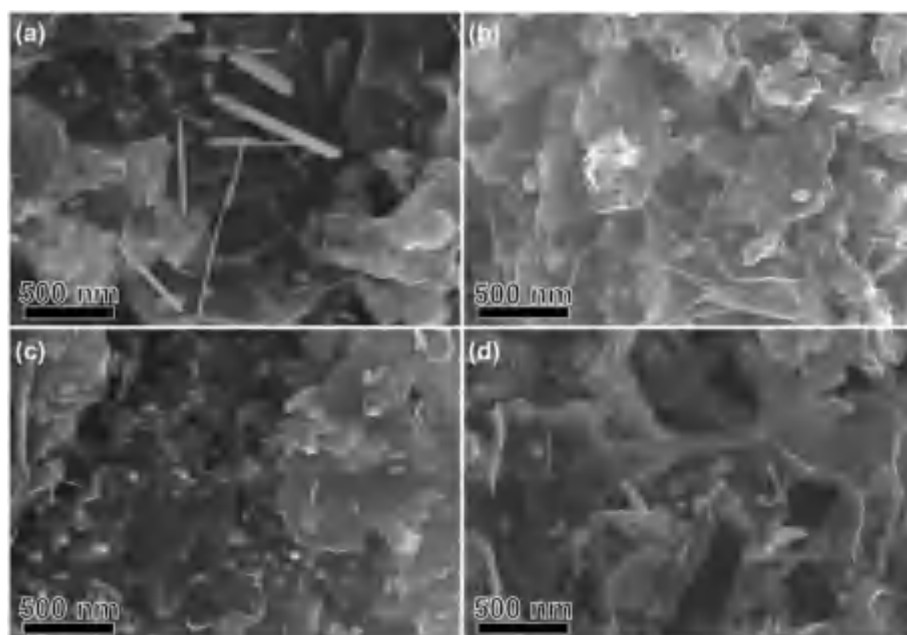


Fig. 1. SEM images of Co₂P/Co-N-C (a), Ni₂P/Ni-N-C (b), NiCoP/Co-Ni-N-C (c) and CoP/NiCoP/Co-Ni-N-C (d).

For instance, Wang et al. build the Ni₂P/NiSe₂ heterostructure, in which the NiSe₂ is susceptible site for anodic reconstruction and provided high OER activity [18]. Besides, Boppella et al. design a CoP/NiCoP heterostructure by adjusting the mole ratio of Ni and Co in the precursor, where the rapid transfer of electrons from CoP to NiCoP leads to more moderate adsorption property toward H⁺ at the heterointerface than that of the two components [19]. Nevertheless, it is difficult to modify the excessive H⁺ adsorption properties of TMPs only by constructing heterostructure. In this regard, coupling the substances with robust H⁺ desorption performance ($\Delta G_{H^*} > 0$) to the TMPs is a more effective scheme [20,21]. Single atoms (SAs), in particular, are extensively researched with the optimal use of metal atom, and their high chemical valence, strong electronic effects and structural stability make them ideal for the H⁺ adsorption modulation [22,23]. In previous studies, transition metal SAs with strong desorption properties have been coupled with active components such as NiFe alloys, NiSe, CoSe, et al. [24–26], and resulted in optimized active sites with ideal ΔG_{H^*} that close to 0. However, the synergistic effect between TMPs based heterostructure and SAs, and the OWS performance in TMPs/SAs compound are still unclear, hindering the rational catalyst design in the future.

In addition to the regulation of the intrinsic activities, it is also crucial to optimize the structure of the catalytic material to expose rich

mass transfer pathways and to obtain good cycling stability [27,28]. To achieve this target, nanostructured TMPs-based electrocatalysts with controlled size and morphology have been demonstrated [29–31]. For example, Ni₂P nanoparticles (NPs) have been synthesized through the controllable pyrolysis of phosphine metal-organic frameworks (MOFs), where the isolated Ni₂P particles are anchored by well-ordered N doped carbon layers in small size format, providing abundant exposed active sites [32]. Additionally, Lv et al. construct a Fe-Co₂P@Fe-N-C electrocatalyst with core-shell structure, in which the Fe SAs doped carbon cladding layer not only protects the Co₂P active site during the electrocatalytic reactions, but also regulates its excessive ΔG_{H^*} in HER. Obviously, the above modulation strategies are valuable to further enhance the catalytic performance of TMPs [33]. Therefore, it is feasible and of research significance to construct high-performance electrolytic water catalysts by coupling morphology adjustment with heterostructures and SAs doping strategies.

Herein, we developed a highly efficient and cost-effective bifunctional electrocatalyst consisting of multi-morphology CoP/NiCoP heterostructure that loaded on hierarchical porous carbon layer with Co, Ni SAs (referred to as CoP/NiCoP/Co-Ni-N-C). The CoP/NiCoP heterostructure provided favorable active sites toward both HER and OER, which was further optimized by the high electropositive Co-N-C and

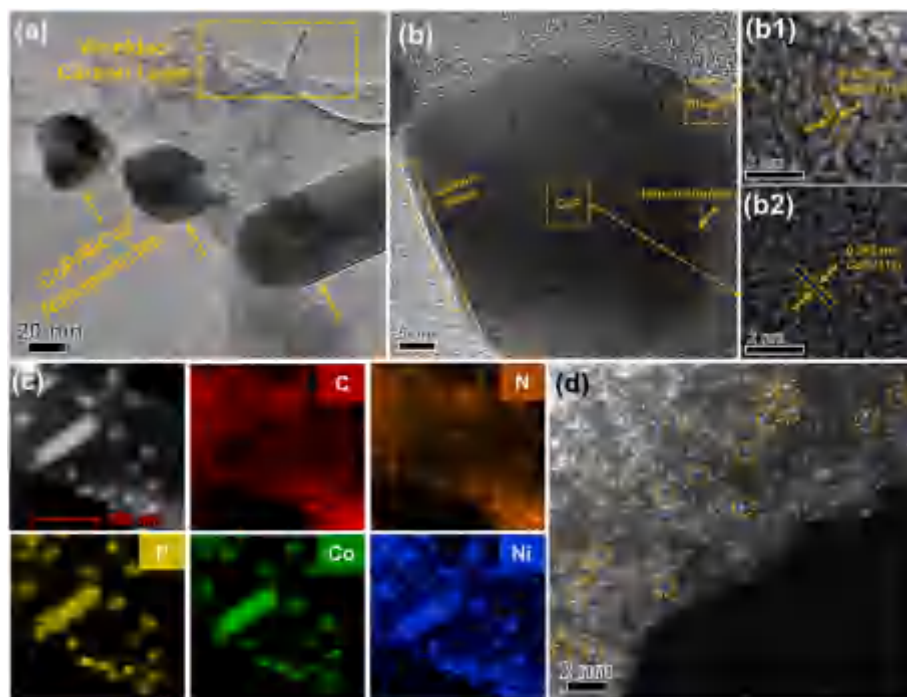


Fig. 2. HRTEM images of CoP/NiCoP/Co-Ni-N-C with lattice fringe of CoP and NiCoP (a–b). AC HAADF-STEM image of CoP/NiCoP/Co-Ni-N-C (c). STEM image of CoP/NiCoP/Co-Ni-N-C and its corresponding EDS mapping of C, N, P, Co, and Ni (d).

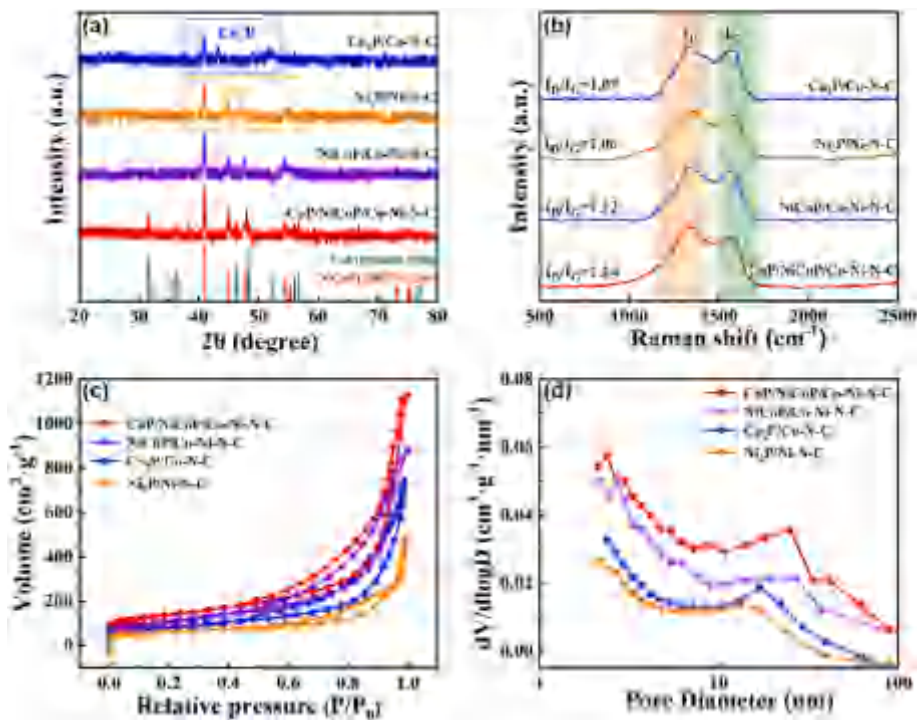


Fig. 3. XRD patterns (a), Raman spectra (b), N_2 adsorption isotherms (c) and pore size distributions (d) of CoP/NiCoP/Co-Ni-N-C and comparison samples.

Ni-N-C. Moreover, $g-C_3N_4$ and inexpensive FCC slurry were used in the synthesis of materials, where the former worked as self-sacrificing template to induce the synthesis of N-doped porous carbon carriers with abundant mass transfer pathways, and the latter acted as an additional carbon source to build carbon coating structures and enhance the loading of Co and Ni SAs. As expected, the CoP/NiCoP/Co-Ni-N-C exhibited good performance toward HER and OER with low

overpotential, and an ultralow voltage requirement to drive OWS. Our work offered a new perspective in the development of high-performance transition metal compound/SAs synergistic electrocatalysts.

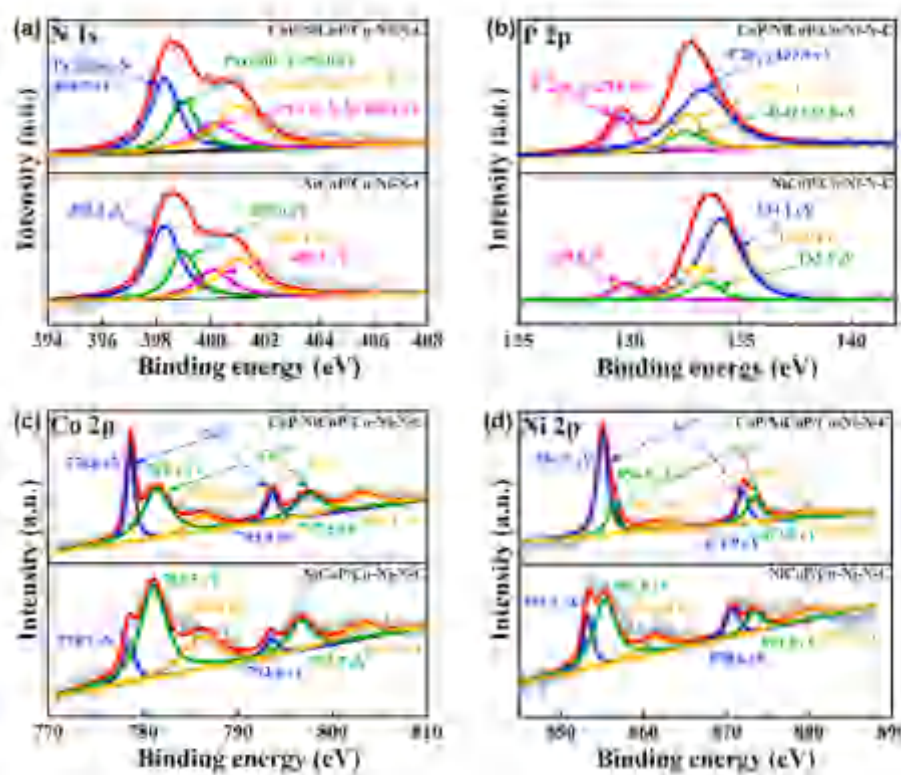


Fig. 4. N 1s (a), P 2p (b), Co 2p (c) and Ni 2p (d) XPS survey spectra of NiCoP/Co-Ni-N-C and CoP/NiCoP/Co-Ni-N-C.

2. Experimental section

2.1. Synthesis of $g\text{-C}_3\text{N}_4/\text{FCC}$

Prior to material synthesis, $g\text{-C}_3\text{N}_4$ (self-sacrificing template) was prepared by pyrolysis of urea according to the reported methods. To produce the $g\text{-C}_3\text{N}_4/\text{FCC}$, 200 mg of FCC slurry (low-cost carbon source for heavy oil) was first dissolved in 100 mL of petroleum ether. Then, 500 mg of $g\text{-C}_3\text{N}_4$ was added in the mixture, which was further sonicated for 30 min to achieve homogeneous solution. Finally, the powder of $g\text{-C}_3\text{N}_4/\text{FCC}$ was obtained through removing the solvent by rotary evaporation.

2.2. Synthesis of CoP/NiCoP/Co-Ni-N-C

The typical synthesis of CoP/NiCoP/Co-Ni-N-C sample was based on the following steps. First of all, a suspension S1 of $g\text{-C}_3\text{N}_4/\text{FCC}$ (700 mg, including 500 mg of $g\text{-C}_3\text{N}_4$ and 200 mg of FCC slurry), $\text{NiCl}_2\cdot 6\text{H}_2\text{O}$ (0.33 mM) and $\text{CoCl}_2\cdot 6\text{H}_2\text{O}$ (0.67 mM, Co:Ni = 2:1, for the generation of CoP and NiCoP) in the 100 mL ethanol was sonicated for 30 min to achieve homogeneity. At the same time, another suspension S2 was prepared by dissolving 1, 10-phenanthroline (2 mM, organic ligand of single atom), $\text{NiCl}_2\cdot 6\text{H}_2\text{O}$ (0.33 mM) and $\text{CoCl}_2\cdot 6\text{H}_2\text{O}$ (0.67 mM, Co:Ni = 2:1, for the generation of single atom) in the 100 mL of mixed solution with ethanol/ H_2O (9:1). The two mixtures (S1 and S2) were then combined and stirred for 6 h before the solvent was removed by rotary evaporation. The resulting solid was mixed with $\text{NH}_4\text{H}_2\text{PO}_4$ powder (0.218 g, 1.65 mmol, for the generation of CoP and NiCoP) and pyrolyzed at 800 °C for 2 h under an Ar flow of 100 mL min^{-1} with a heating rate of 5 °C min^{-1} to obtain the CoP/NiCoP/Co-Ni-N-C. Besides, materials with different Co over Ni molar ratios (1:1, 0:1 and 1:0) were prepared by regulating the amount of $\text{NiCl}_2\cdot 6\text{H}_2\text{O}$ and $\text{CoCl}_2\cdot 6\text{H}_2\text{O}$ in S1 and S2, which were named as NiCoP/Co-Ni-N-C, $\text{Ni}_2\text{P}/\text{Ni-N-C}$ and $\text{Co}_2\text{P}/\text{Co-N-C}$, respectively. In addition, to demonstrate the synergistic

effect between phosphide particles and single atoms, the pure single atom sample (Co-Ni-N-C) was prepared by removing the $\text{NiCl}_2\cdot 6\text{H}_2\text{O}$ and $\text{CoCl}_2\cdot 6\text{H}_2\text{O}$ from S1, eliminating the $\text{NH}_4\text{H}_2\text{PO}_4$ adding and removing the agglomerated metal particles by acid washing. Meanwhile, the ligand 1, 10-phenanthroline was replaced by triphenylmethane to construct the control sample of pure phosphide heterostructure (CoP/NiCoP). Other experimental details (including reagents, conditions of test and theoretical calculations) are described in the supporting information.

3. Results and discussion

3.1. Materials synthesis and characterization

The synthesis of CoP/NiCoP/Co-Ni-N-C followed the facile precursor mixing and one-pot pyrolysis technique (Scheme 1). The mixture included Co^{2+} , Ni^{2+} , $\text{NH}_4\text{H}_2\text{PO}_4$, 1,10-phenanthroline, $g\text{-C}_3\text{N}_4$, and FCC slurry was subjected to pyrolysis at 800 °C under an Ar atmosphere. The pre-chelated Ni and Co-phenanthroline induced the construction of single atomic Co and Ni into the carbon framework as Co-N₄ and Ni-N₄ moieties. Meanwhile, the unliganded Co and Ni were phosphorated by the PH_3 generated from $\text{NH}_4\text{H}_2\text{PO}_4$ decomposition to produce the CoP/NiCoP active site. Moreover, the self-sacrificing template $g\text{-C}_3\text{N}_4$ led to the formation of the wrinkled carbon carrier with hierarchical pores, and the N-rich gas generated from its decomposing yielded abundant N atoms doping [34,35]. Besides, the FCC slurry not only resulted in the formation of carbon coated CoP/NiCoP heterostructure, but also assisted anchoring of more single atoms [36].

The morphologies of CoP/NiCoP/Co-Ni-N-C was initially investigated by scanning electron microscope (SEM) and high-resolution transmission electron microscope (HR-TEM). The wrinkled carbon thin layers could be observed in all the samples shown in Fig. 1 and Fig. S1, which were generated from the induction of $g\text{-C}_3\text{N}_4$ template. Expect for the sample of pure SAs (Co-Ni-N-C, Fig. S1(a)), the nanoparticles (NPs)

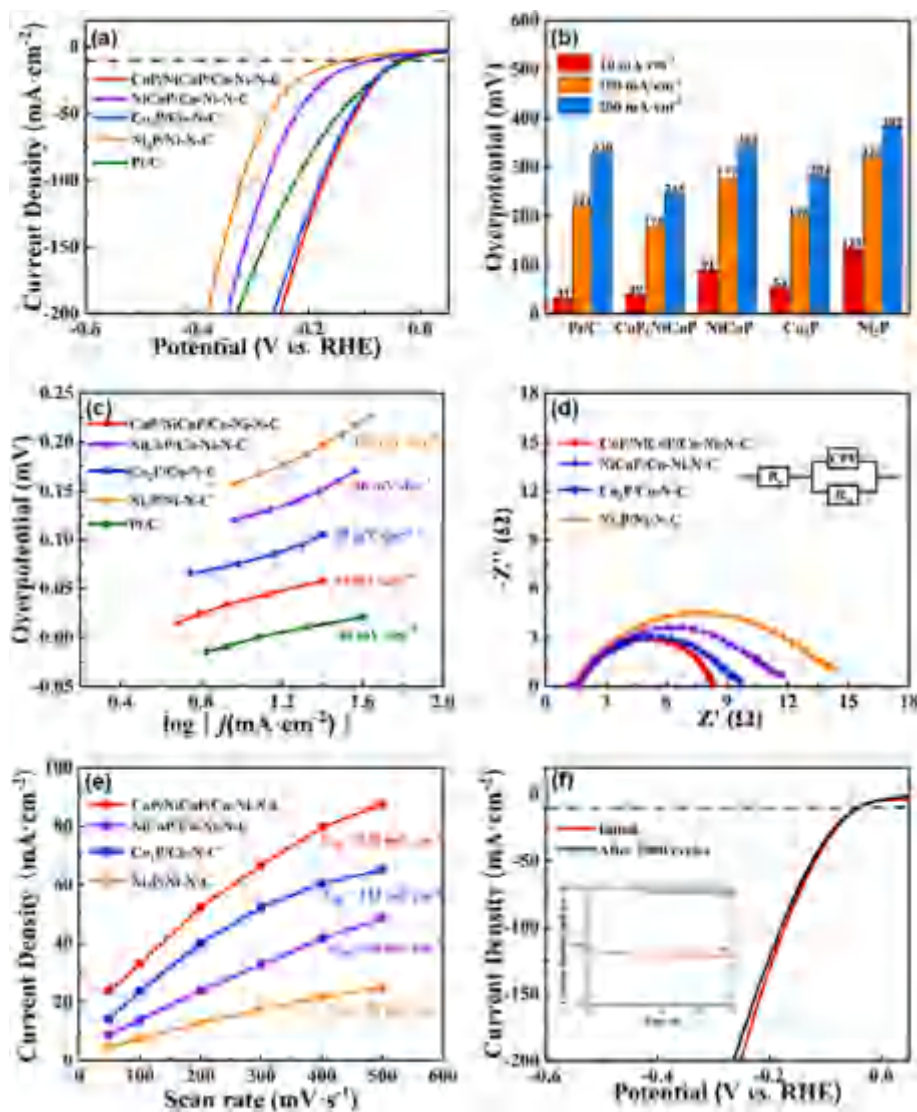


Fig. 5. Polarization LSV curves (a), performance comparison (b), Tafel slopes (c), EIS measurement (d), and C_{dl} values (e) of CoP/NiCoP/Co-Ni-N-C and comparison samples toward HER. Stability tests of CoP/NiCoP/Co-Ni-N-C toward HER (f).

of Co or Ni phosphides were found to be anchored by the carbon layer with large surface, leading to abundant and even-distributed active sites [37]. The induction of viscous FCC slurry during pyrolysis provided tight carbon shells outside the NPs of phosphides, which avoided the agglomeration and reduced the electrochemical corrosion at harsh conditions. It is noteworthy that the FCC slurry limited the diameter increasing of NPs, inducing their longitudinal growth and rod-like structure (Fig. 1(a) and (d)) [38]. Furthermore, in the samples without the addition of SAs ligand (CoP/NiCoP, Fig. S1(b)), the formation of large-sized particles was observed, suggesting that the 1, 10-phenanthroline also contributed to restrict the size of NPs. The TEM images further revealed that the NPs and small amount of nanorods of CoP/NiCoP were uniformly distributed on the wrinkled carbon layer (Figs. S2 and 2(a)). Furthermore, the thin carbon layers coated on the NPs could be observed in the HR-TEM image (Fig. 2(b)). The lattice stripes on both sides of heterointerface with d spacing values of 0.227 and 0.247 nm corresponded to the (111) crystal planes of NiCoP and CoP, respectively, demonstrating the generation of CoP/NiCoP heterostructure (Fig. 2(b1) and (b2)). Besides, the presence of Ni, Co and P signals matched the corresponding CoP/NiCoP nanostructures well in the energy-dispersive X-ray spectroscopy mapping (EDS), while the C, N, P, Co, and Ni elements were uniformly distributed in the carbon framework (Fig. 2(c)). In

addition, the image of aberration-corrected high-angle annular darkfield scanning transmission electron microscopy (AC HAADF-STEM) presented the homogeneous dispersion of bright dots on carbon shells, which proved the generation of SAs (Co or Ni SAs, Fig. 2(d)). To further illustrate the existence of SAs, the ICP-OES test was utilized to analyze the mass fraction of Co and Ni in Co-Ni-N-C and CoP/NiCoP/Co-Ni-N-C (Table S1). After sufficient acid washing to remove metal nanoparticles, the Co content and Ni content of the Co-Ni-N-C still reached 1.46 and 0.63 wt%, respectively, indicating that the Co and Ni single atoms were anchored in carbon layer [39,40]. In the CoP/NiCoP/Co-Ni-N-C sample, the content of Co and Ni increased to 8.43 and 3.90 wt% due to the inclusion of CoP/NiCoP heterostructure NPs.

The crystalline structures of CoP/NiCoP/Co-Ni-N-C and other obtained samples were investigated by X-ray diffraction (XRD). The CoP/NiCoP (Fig. S3) and CoP/NiCoP/Co-Ni-N-C (Fig. 3(a)) samples exhibited signals that corresponded well with the standard peaks of CoP (PDF#89-2958) and NiCoP (PDF#71-2336), which further indicated the construction of the expected heterostructure. It was notable that when the metal in the raw material was pure Co or Ni, the phosphide produced after pyrolysis was Co_2P or Ni_2P ($\text{Co}_2\text{P}/\text{Co-Ni-N-C}$ and $\text{Ni}_2\text{P}/\text{Ni-Ni-N-C}$ samples). On the contrary, the Co doped Ni_2P (NiCoP) would be formed

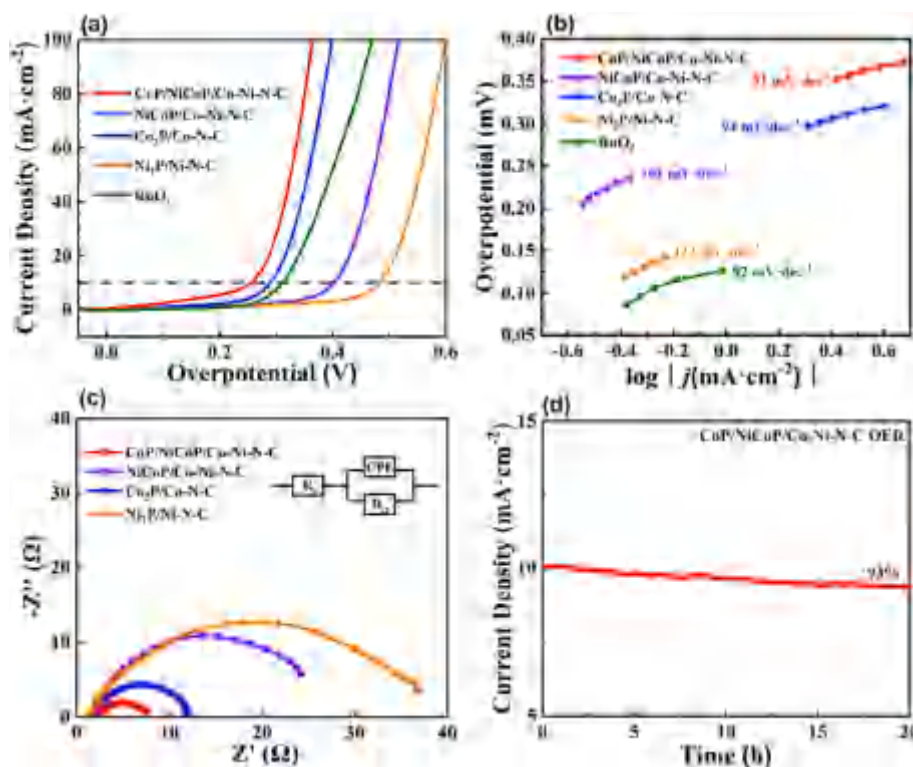


Fig. 6. Polarization LSV curves of CoP/NiCoP/Co-Ni-N-C and comparison samples toward OER (a), Tafel slopes (b) and EIS measurement (c). Stability tests of CoP/NiCoP/Co-Ni-N-C toward OER (d).

as both Ni and Co were in the precursor, and the extra Co translated to CoP and constituted the CoP/NiCoP heterostructure [12,41]. Besides, the XRD pattern of Co-Ni-N-C sample exhibited the peak of C and revealed the absence of Co and Ni peaks. Combined with the ICP-OES results discussed above, the metal particles in this sample were sufficiently removed by acid washing, and the remaining Co and Ni were come from the SAs in the carbon layer. The structural properties of obtained samples were further revealed by Raman spectra (Fig. 3(b)), which presented the characteristic D band (1350 cm^{-1}) and G band (1580 cm^{-1}) that originated from sp^2 hybridized carbon with ordered structure, as well as defects and edge structures of graphitic carbon, respectively [42,43]. Compared with the samples of $\text{Co}_2\text{P}/\text{Co-N-C}$ (1.09) and $\text{Ni}_2\text{P}/\text{Ni-N-C}$ (1.06), the higher I_D/I_G values of 1.12 and 1.14 were observed in the spectra of NiCoP/Co-Ni-N-C and CoP/NiCoP/Co-Ni-N-C, respectively, demonstrating that the electronic interaction between the dual SAs affected the M–N (metal-nitrogen bond) structure and resulted in more defects on the carbon layer [44, 45]. In addition, the porous structures were confirmed by the N_2 adsorption experiments (Fig. 3(c)), which showed that CoP/NiCoP/Co-Ni-N-C had the highest BET surface area and porosity. Based on the further analysis of pore size distribution, the hierarchical porous structure of CoP/NiCoP/Co-Ni-N-C composed by the microporosity and mesoporosity (Fig. 3(d)), which provide enriching pathways for electrolyte and reaction products transfer.

The in-depth information of chemical composition was analyzed by X-ray photoelectron spectroscopy (XPS) to reveal the electronic synergy between CoP/NiCoP heterostructure and Co, Ni SAs. To be specific, the spectra of NiCoP/Co-Ni-N-C and CoP/NiCoP/Co-Ni-N-C were compared to illustrate the effect of constructing heterostructure. Both two samples possessed similar composition of carbon layer that included C–C, C–N, C–P and C–O (surface absorbed O) bonds (Fig. S4). Meanwhile, the N 1s and P 2p spectra of the two samples also exhibited the parallel characteristic peaks (Fig. 4(a) and (b)). Among them, the N 1s spectra of the two samples revealed three types of N signals: pyridinic N,

pyrrolic N, and graphitic N. Notably, a distinctive peak at 400.1 eV was assigned to N–Co or N–Ni, suggesting the presence of single atomic Co and Ni sites in the carbon frameworks [46]. Moreover, both Co 2p and Ni 2p spectra consisted of 6 peaks (Fig. 4(c)–(d)) for the NiCoP/Co-Ni-N-C and CoP/NiCoP/Co-Ni-N-C samples, which corresponded to the, $\text{Co}^{2+}/\text{Ni}^{2+} 2p_{3/2}$, $\text{Co}^{3+}/\text{Ni}^{3+} 2p_{3/2}$, $\text{Co}^{2+}/\text{Ni}^{2+} 2p_{1/2}$, $\text{Co}^{3+}/\text{Ni}^{3+} 2p_{1/2}$ and the satellite peaks of $2p_{3/2}$ and $2p_{1/2}$, respectively. Notably, the Co $2p_{3/2}$ peaks in the NiCoP/Co-Ni-N-C sample were at higher binding energy (778.7 and 781.5 eV for Co^{2+} and Co^{3+}) than that of CoP/NiCoP/Co-Ni-N-C (778.6 and 781.4 eV for Co^{2+} and Co^{3+}), proving the higher valence state of Co element. On the contrary, the Ni $2p_{3/2}$ peaks in the NiCoP/Co-Ni-N-C sample exhibited lower binding energy (853.5 and 855.5 eV for Ni^{2+} and Ni^{3+}) than that of CoP/NiCoP/Co-Ni-N-C (854.9 and 855.6 eV for Ni^{2+} and Ni^{3+}). Such phenomenon in electronic structure indicate the electron exchange between CoP and NiCoP heterostructure, which enabled higher charge transport efficiency in electrocatalytic processes [11,41]. Additionally, the Co 2p and Ni 2p spectra of CoP/NiCoP/Co-Ni-N-C were compared with the pure heterostructure (CoP/NiCoP) and the pure SAs (Co-Ni-N-C) samples (Fig. S5). As expected, the Co and Ni element in CoP/NiCoP presented lower binding energy and valence, resulting in excessive adsorption toward H^* . On the contrary, the higher positive oxidation state of Co and Ni in Co-Ni-N-C were more favorable for the H^* desorption. As the electronic synergy between the heterostructure and the SAs was generated, the Co and Ni sites in the CoP/NiCoP/Co-Ni-N-C samples showed moderate chemistry valence, which was more beneficial for efficient electrocatalytic HER [47,48].

3.2. Electrocatalytic activity toward HER, OER and OWS

The electrocatalytic HER activities of CoP/NiCoP/Co-Ni-N-C were investigated through LSV in 1.0 M KOH under a scan rate of 5 mV s^{-1} (Fig. 5(a)–(b)). Based on the similar carbon substrate with SAs doping, the CoP/NiCoP/Co-Ni-N-C exhibited a lower overpotential of 40

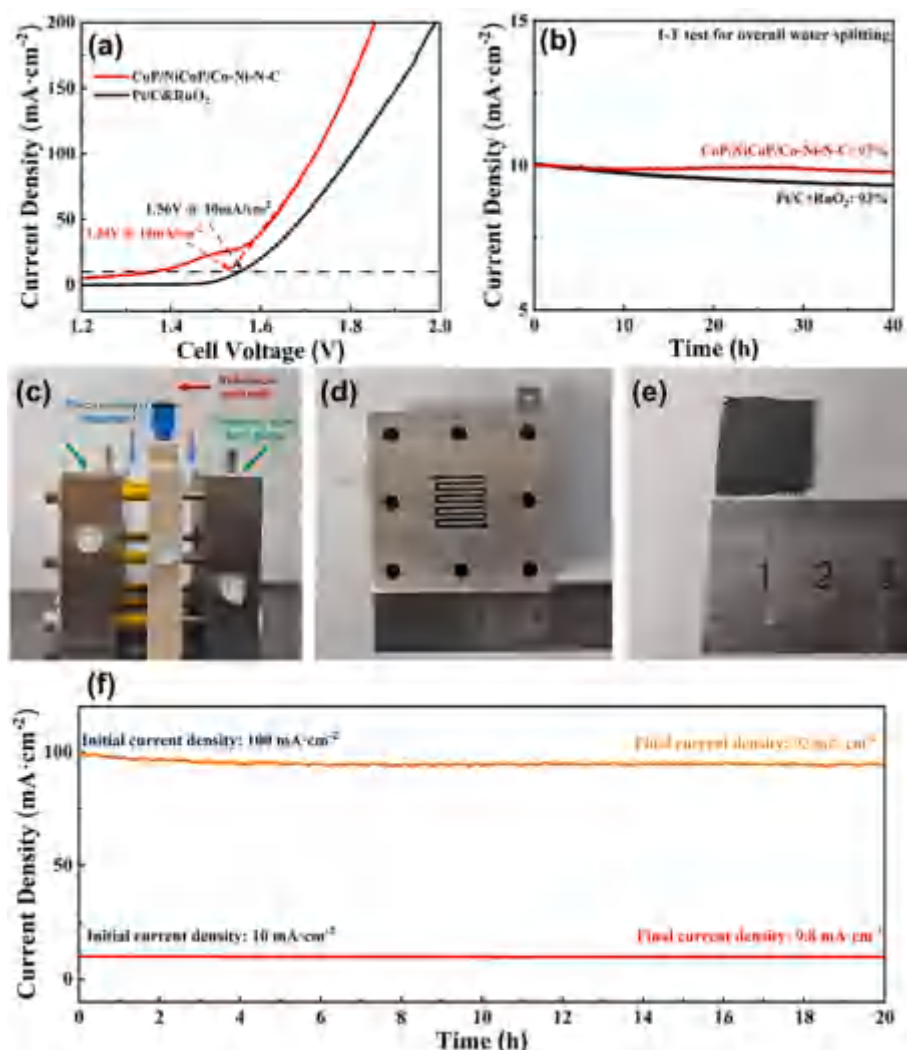


Fig. 7. Polarization LSV curves of CoP/NiCoP/Co-Ni-N-C and noble-metal catalysts toward OWS (a). Stability tests of CoP/NiCoP/Co-Ni-N-C and noble-metal catalysts toward OWS (b). Photos of water electrolysis device (c), stainless steel pole planes (d) and carbon cloth coated with CoP/NiCoP/Co-Ni-N-C (e). Stability test result of CoP/NiCoP/Co-Ni-N-C at the initial current density of 10 and 100 mA cm⁻² for 20 h (f).

mV@10 mA cm⁻² than that of the Co₂P/Co-N-C (53 mV@10 mA cm⁻²), Ni₂P/Ni-N-C (135 mV@10 mA cm⁻²) and NiCoP/Co-Ni-N-C samples (91 mV@10 mA cm⁻²), indicating that the CoP/NiCoP heterostructure possessed the optimal HER performance. Compared with the CoP/NiCoP (213 mV@10 mA cm⁻²) and Co-Ni-N-C (135 mV@10 mA cm⁻²), the CoP/NiCoP/Co-Ni-N-C revealed better HER performance, which proved the electronic synergy between the heterostructure NPs and SAs (Fig. S6(a)). Benefit from the effects discussed above, the HER performance of CoP/NiCoP/Co-Ni-N-C was close to that of Pt/C (34 mV) at 10 mA cm⁻², while the overpotentials at high current densities (178 mV@100 mA cm⁻² and 245 mV@200 mA cm⁻²) were significantly superior to those of the noble-metal catalyst (221 mV@100 mA cm⁻² and 330 mV@200 mA cm⁻²). In contrast with recently reported electrocatalysts with similar compositions or structures, the CoP/NiCoP/Co-Ni-N-C exhibited better HER performance as well (Fig. S7)). The kinetics of HER was further analyzed by the values of Tafel slope (Fig. 5 (c) and Fig. S6(b)). The Tafel slope value of CoP/NiCoP/Co-Ni-N-C was 55 mV·dec⁻¹, indicating that the HER process followed the Volmer-Heyrovsky mechanism [49,50]. Meanwhile, the CoP/NiCoP/Co-Ni-N-C possessed the lowest Tafel slope among the obtained samples, which demonstrated its fast reaction kinetics. On the other side, the CoP/NiCoP/Co-Ni-N-C presented the lower R_{ct} (8.26 Ω) than that of Co₂P/Co-N-C (9.64 Ω), Ni₂P/Ni-N-C (14.21 Ω) and

NiCoP/Co-Ni-N-C (11.70 Ω), suggesting that heterostructure composed by CoP and NiCoP enhanced the charge transfer efficiency during HER process (Fig. 5(d)) [51]. Furthermore, the electrochemical surface area (ECSA) of all the samples was measured by the corresponding double layer capacitances (C_{dl} , Fig. 5(e) and Fig. S8). The CoP/NiCoP/Co-Ni-N-C exhibited higher C_{dl} value of 128 mF cm⁻² than other samples, demonstrating that the wrinkled and defective carbon carrier provided larger surface area for charge transfer, which was consistent with the results of Raman and BET [52,53]. In addition, the cyclic stability of the CoP/NiCoP/Co-Ni-N-C was measured by the LSV tests that before and after 2000 CV cycles (Fig. 5(f)), where the negligible attenuation of LSV curves demonstrated its excellent cyclic stability toward HER. Meanwhile, the current density retained 95% and 91% of the initial value after 20 h and 100 h chronoamperometry test (Fig. S9), which further proved the favorable durability of CoP/NiCoP/Co-Ni-N-C.

The OER activities of CoP/NiCoP/Co-Ni-N-C and control samples were also evaluated through LSV (Fig. 6(a)). Benefit from the efficient charge transfer and enhanced OH⁻ adsorption on the CoP/NiCoP heterointerface, the CoP/NiCoP/Co-Ni-N-C exhibited good OER performance with the overpotential of 255 mV@10 mA cm⁻², lower than that of Co₂P/Co-N-C (290 mV@10 mA cm⁻²), Ni₂P/Ni-N-C (482 mV@10 mA cm⁻²) and NiCoP/Co-Ni-N-C (402 mV@10 mA cm⁻²).

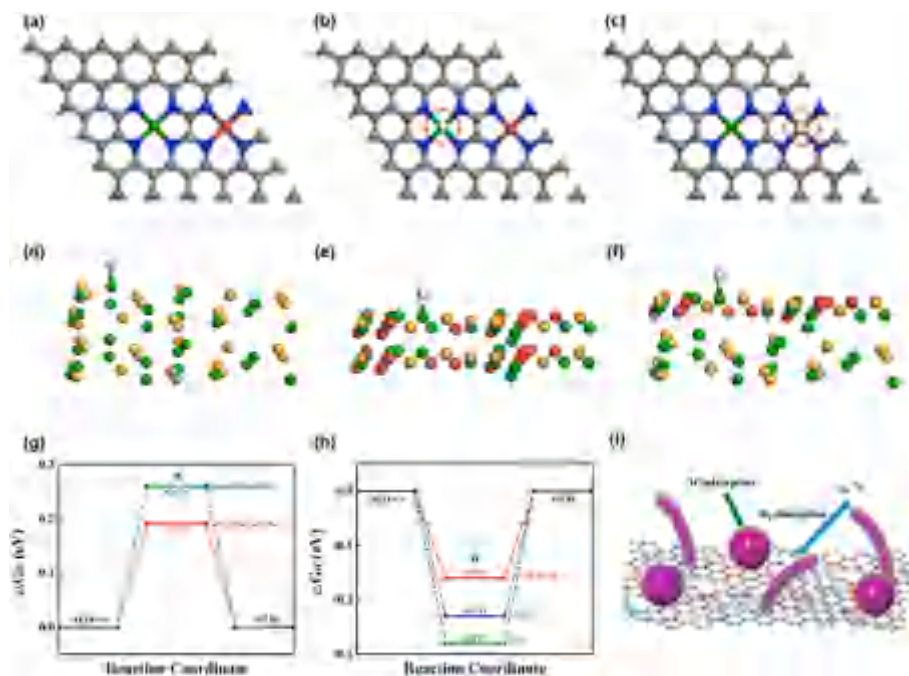


Fig. 8. The model of Co–Ni–N–C (a). Hydrogen proton adsorption on Co or Ni sites in Co–Ni–N–C model (b–c). Hydrogen proton adsorption on CoP, NiCoP and CoP/NiCoP models (d–f). Gibbs free energy diagram of HER for different active sites of Co–Ni–N–C model (g). Gibbs free energy diagram of HER for different active sites of CoP, NiCoP and CoP/NiCoP models (h). Schematic of HER mechanism on CoP/NiCoP/Co–Ni–N–C (i).

Noteworthy, the CoP/NiCoP/Co–Ni–N–C had better performance than RuO_2 ($314 \text{ mV}@10 \text{ mA cm}^{-2}$), which proved the superior activity than noble metal-based materials in OER. The Tafel slope toward OER of CoP/NiCoP/Co–Ni–N–C and control samples were evaluated based on the result of LSV (Fig. 6(b)). The CoP/NiCoP/Co–Ni–N–C exhibited fast reaction kinetics with the Tafel slope of $81 \text{ mV}\cdot\text{dec}^{-1}$, lower than that of $\text{Co}_2\text{P}/\text{Co–N–C}$ ($94 \text{ mV}\cdot\text{dec}^{-1}$), $\text{Ni}_2\text{P}/\text{Ni–N–C}$ ($122 \text{ mV}\cdot\text{dec}^{-1}$), NiCoP/Co–Ni–N–C ($101 \text{ mV}\cdot\text{dec}^{-1}$) and commercial RuO_2 ($92 \text{ mV}\cdot\text{dec}^{-1}$). Meanwhile, compared to the samples that contained only one phosphide ($\text{Co}_2\text{P}/\text{Co–N–C}$, $\text{Ni}_2\text{P}/\text{Ni–N–C}$ and NiCoP/Co–Ni–N–C), the CoP/NiCoP heterostructure had higher charge transfer efficiency, which could be proved by the lower charge transfer resistance presented in the EIS results (Fig. 6(c)) [11]. Besides, the current density retained 93% of the initial value after 20 h I–t test (Fig. 6(d)), which proved the favorable durability of CoP/NiCoP/Co–Ni–N–C toward OER.

Based on the good activities of HER and OER, an overall water splitting cell was assembled with CoP/NiCoP/Co–Ni–N–C as both cathodic catalyst and anodic catalyst in 1 M KOH solution (Fig. 7(a)). The CoP/NiCoP/Co–Ni–N–C system only required 1.54 V to achieve the current density of 10 mA cm^{-2} , which was better than that of noble metal-based two-electrode system (Pt/C & RuO_2 , 1.56 V at 10 mA cm^{-2}). Meanwhile, after 40 h of chronoamperometry test, the current density of CoP/NiCoP/Co–Ni–N–C maintained 97% of the initial value, higher than that of Pt/C & RuO_2 (93%), which proved the good stability and potential in the application of OWS (Fig. 7(b)). Moreover, the nearly 100% faradaic efficiency (FE) was proved by the ratio of H_2/O_2 that close to 2:1 (Fig. S10), demonstrating the high matching of the cathode and anode of the material in the OWS process [49]. Besides, the morphology of the cathodic (Fig. S11(a)) and anodic (Fig. S11(b)) CoP/NiCoP/Co–Ni–N–C after the chronoamperometry test were not changed compared to the pre-reaction period, indicating that the anchoring and coating effect of the carbon layer protected the active substances in the reaction. Furthermore, the characteristic peaks of CoP and NiCoP could still be observed in the XRD pattern after the HER reaction, indicating that the active substances were not changed after the reaction (Fig. S12). However, the intensity of both CoP and NiCoP characteristic peaks in the XRD of the samples after OER were

significantly reduced, illustrating that the crystallinity of the samples decreased. According to the mechanism of OER, this phenomenon could be attributed to the attachment of amorphous reaction intermediates on the surface of the CoP/NiCoP nanoparticles, such as the hydroxides ($\text{Ni}(\text{OH})_2$ or $\text{Co}(\text{OH})_2$) and hydroxyl oxides (NiOOH or CoOOH). Based on the results from laboratory-used electrolyzer, we built a simulated water electrolysis device with anion exchange membrane (AEM). The basic structure of the device was shown in Fig. 7(c), where the serpentine flow field was distributed on the center of the stainless steel pole plates (Fig. 7(d)) and the electrocatalyst (CoP/NiCoP/Co–Ni–N–C) powder was coated on carbon cloth ($1.6 \times 1.6 \text{ cm}$, Fig. 7(e)). Based on the device, we tested the stability of the CoP/NiCoP/Co–Ni–N–C at the initial current density of 10 and 100 mA cm^{-2} (Fig. 7(f)). After 20 h I–t test, the sample could maintain the catalytic activity of 98% and 92%, respectively, indicating that the CoP/NiCoP/Co–Ni–N–C had the potential for application. In conclusion, the CoP/NiCoP/Co–Ni–N–C served as a favorable electrocatalyst for efficient water splitting.

3.3. DFT calculations

To better explain the HER mechanism on the surface of CoP/NiCoP/Co–Ni–N–C, we performed a series of DFT calculations. Since the sample composition was complex and overall modeling was difficult, we performed calculations for the Co, Ni SAs fraction (Fig. 8(a–c)) and the CoP/NiCoP heterostructure fraction separately (Fig. 8(d–f)). Both Co and Ni SAs sites exhibited the Gibbs free energy of hydrogen adsorption (ΔG_{H^*}) that greater than 0 eV (0.19 eV for the Ni site and 0.26 eV for the Co site, Fig. 8(g)), indicating that they were unfavorable for adsorption of H^* but favorable for H_2 desorption. On the contrary, either pure CoP, pure NiCoP or CoP/NiCoP heterostructure exhibited the ΔG_{H^*} that lower than 0 eV (-0.28 eV for the CoP, -0.23 eV for the NiCoP and -0.16 eV for the CoP/NiCoP heterostructure, Fig. 8(h)), suggesting that they are more prone to adsorb H^* in the HER process [5]. Based on the above results, it could be hypothesized that the intrinsic synergy effect between the SAs and the heterostructure in the CoP/NiCoP/Co–Ni–N–C was consistent with the hydrogen spillover mechanism (Fig. 8(i)) [54,55]. The hydrogen protons from the dissociation of water molecules are first

adsorbed on the surface of the CoP/NiCoP and activated, and then the H^* transferred to the Co or Ni single atom sites on the carbon layer to form H_2 molecules and detach from the electrocatalyst. Benefit from the efficient adsorption-desorption process, the CoP/NiCoP/Co–Ni–N–C sample exhibited high activity and fast reaction kinetics toward HER.

4. Conclusion

In summary, we designed and synthesized a composite electrocatalyst CoP/NiCoP/Co–Ni–N–C for efficient HER and OER. The electrocatalyst consisting of Co and Ni SAs doped carbon and the encapsulated multi-morphology CoP/NiCoP nanostructures was synthesized by a facile one-pot pyrolysis strategy. Based on the characterization results, an apparent charge transfer was revealed between the heterostructure and the SAs sites to optimize the charge distribution, which enabled the moderate H^* adsorption and led to the low overpotential of 40 mV at 10 mA cm^{−2}. Meanwhile, the CoP/NiCoP heterostructure provided favorable active sites toward OER, which supported the low cell voltage of 1.54 V at 10 mA cm^{−2} in the two-electrode system for OWS. Besides, the enwrapping carbon shells provided by the FCC slurry benefited the excellent durability during long-term electrocatalysis. This work presents a facile yet efficient synthetic method for the low-cost TMPs-based heterostructure/SAs OWS electrocatalysts to promote the efficiency of hydrogen production.

Declaration of competing interest

The authors declare that they have no known competing financial interests or personal relationships that could have appeared to influence the work reported in this paper.

Acknowledgements

We gratefully thank for the National Natural Science Foundation of China (Nos.22278431, 21776302, and 22108301) and the China Postdoctoral Science Foundation (No.2021M703577) for financial support of this work.

Appendix A. Supplementary data

Supplementary data to this article can be found online at <https://doi.org/10.1016/j.ijhydene.2023.12.250>.

References

- [1] Roger I, Shipman MA, Symes MD. Earth-abundant catalysts for electrochemical and photoelectrochemical water splitting. *Nat Rev Chem* 2017;1:3. <https://doi.org/10.1038/s41570-016-0003>.
- [2] Anantharaj S, Ede SR, Sakthikumar K, Karthik K, Mishra S, Kundu S. Recent trends and perspectives in electrochemical water splitting with an emphasis on sulfide, selenide, and phosphide catalysts of Fe, Co, and Ni: a review. *ACS Catal* 2016;6: 8069–97. <https://doi.org/10.1021/acscatal.6b02479>.
- [3] Staffell I, Scamman D, Velazquez Abad A, Balcombe P, Dodds PE, Ekins P, Shah N, Ward KR. The role of hydrogen and fuel cells in the global energy system. *Energy Environ Sci* 2019;12:463–91. <https://doi.org/10.1039/c8ee01157e>.
- [4] Peng X, Yan Y, Jin X, Huang C, Jin W, Gao B, Chu PK. Recent advance and perspectives of electrocatalysts based on transition metal selenides for efficient water splitting. *Nano Energy* 2020;78:105234. <https://doi.org/10.1016/j.nanoen.2020.105234>.
- [5] Zhu J, Hu L, Zhao P, Lee LYS, Wong KY. Recent advances in electrocatalytic hydrogen evolution using nanoparticles. *Chem Rev* 2020;120:851–918. <https://doi.org/10.1021/acs.chemrev.9b00248>.
- [6] Shi Y, Zhang B. Recent advances in transition metal phosphide nanomaterials: synthesis and applications in hydrogen evolution reaction. *Chem Soc Rev* 2016;45: 1529–41. <https://doi.org/10.1039/c5cs00434a>.
- [7] Liu C, Gong T, Zhang J, Zheng X, Mao J, Liu H, Li Y, Hao Q. Engineering Ni₂P–NiSe₂ heterostructure interface for highly efficient alkaline hydrogen evolution. *Appl Catal B Environ* 2020;262:1–8. <https://doi.org/10.1016/j.apcatb.2019.118245>.
- [8] Yan H, Xie Y, Wu A, Cai Z, Wang L, Tian C, Zhang X, Fu H. Anion-modulated HER and OER activities of 3D Ni–V-based interstitial compound heterojunctions for high-efficiency and stable overall water splitting. *Adv Mater* 2019;31:1–9. <https://doi.org/10.1002/adma.201901174>.
- [9] Lin J, Yan Y, Li C, Si X, Wang H, Qi J, Cao J, Zhong Z, Fei W, Feng J. Bifunctional electrocatalysts based on Mo-doped NiCoP nanosheet arrays for overall water splitting. *Nano-Micro Lett* 2019;11:1–11. <https://doi.org/10.1007/s40820-019-0289-6>.
- [10] Yan F, Yan L, Wei X, Han Y, Huang H, Xu S, Liang X, Zhou W, Guo J. Structure-design and synthesis of nickel-cobalt oxide/sulfide/phosphide composite nanowire arrays for efficient overall water splitting. *Int J Hydrogen Energy* 2022;47: 10616–27. <https://doi.org/10.1016/j.ijhydene.2022.01.108>.
- [11] Lin Y, Sun K, Liu S, Chen X, Cheng Y, Cheong WC, Chen Z, Zheng L, Zhang J, Li X, Pan Y, Chen C. Construction of CoP/NiCoP nanotadpoles heterojunction interface for wide pH hydrogen evolution electrocatalysis and supercapacitor. *Adv Energy Mater* 2019;9:1–12. <https://doi.org/10.1002/aenm.201901213>.
- [12] Chen B, Jiang ZJ, Wang Y, Yan H, Jiang Z. In-situ single-phase derived NiCoP/CoP hetero-nanoparticles on amine-carbon nanotubes as highly efficient pH-universal electrocatalysts for hydrogen evolution. *Electrochim Acta* 2022;416: 140280. <https://doi.org/10.1016/j.electacta.2022.140280>.
- [13] Bhutani D, Maity S, Chaturvedi S, Chalapathi D, Waghmare UV, Narayana C, Prabhakaran VC, Muthusamy E. Heterostructure from heteromixture: unusual OER activity of FeP and CoP nanostructures on physical mixing. *J Mater Chem A* 2022; 147:22354–62. <https://doi.org/10.1039/d2ta04296g>.
- [14] Liu H, Yang F, Chen F, Che S, Chen N, Xu C, Wu N, Wei W, Li Y. Bimetallic Ni-Co selenide heterostructure aerogel for highly efficient overall water splitting. *Mater Chem Front* 2023;1365–73. <https://doi.org/10.1039/d2qm01082h>.
- [15] Liu H, Yang F, Chen F, Che S, Chen N, Sun S, Ta N, Sun Y, Wu N, Sun Y, Li Y. Interface and electronic structure regulation of Mo-doped NiSe₂-CoSe₂ heterostructure aerogel for efficient overall water splitting. *J Colloid Interface Sci* 2023;640:1040–51. <https://doi.org/10.1016/j.jcis.2023.02.154>.
- [16] Wu D, Kong A, Li W, Fu Y, Zhang J. Facile synthesis of bimetallic Ni–Fe phosphide as robust electrocatalyst for oxygen evolution reaction in alkaline media. *Int J Hydrogen Energy* 2021;46:39844–54. <https://doi.org/10.1016/j.ijhydene.2021.09.217>.
- [17] Wei Y, Li W, Li D, Yi L, Hu W. Amorphous-crystalline cobalt-molybdenum bimetallic phosphide heterostructured nanosheets as Janus electrocatalyst for efficient water splitting. *Int J Hydrogen Energy* 2022;47:7783–92. <https://doi.org/10.1016/j.ijhydene.2021.12.106>.
- [18] Wang P, Pu Z, Li W, Zhu J, Zhang C, Zhao Y, Mu S. Coupling NiSe₂-Ni₂P heterostructure nanowrinkles for highly efficient overall water splitting. *J Catal* 2019;377:600–8. <https://doi.org/10.1016/j.jcat.2019.08.005>.
- [19] Boppella R, Tan J, Yang W, Moon J. Homologous CoP/NiCoP heterostructure on N-doped carbon for highly efficient and pH-universal hydrogen evolution electrocatalysis. *Adv Funct Mater* 2019;29:1–9. <https://doi.org/10.1002/adfm.201807976>.
- [20] Putri LK, Ng BJ, Yeo RYZ, Ong WJ, Mohamed AR, Chai SP. Engineering nickel phosphides for electrocatalytic hydrogen evolution: a doping perspective. *Chem Eng J* 2023;461:141845. <https://doi.org/10.1016/j.cej.2023.141845>.
- [21] Jiang X, Yue X, Li Y, Wei X, Zheng Q, Xie F, Lin D, Qu G. Anion-cation-dual doped tremella-like nickel phosphides for electrocatalytic water oxidation. *Chem Eng J* 2021;426:130718. <https://doi.org/10.1016/j.cej.2021.130718>.
- [22] Zhao D, Zhuang Z, Cao X, Zhang C, Peng Q, Chen C, Li Y. Atomic site electrocatalysts for water splitting, oxygen reduction and selective oxidation. *Chem Soc Rev* 2020;49:2215–64. <https://doi.org/10.1039/c9cs00869a>.
- [23] Yang Q, Liu H, Yuan P, Jia Y, Zhuang L, Zhang H, Yan X, Liu G, Zhao Y, Liu J, Wei S, Song L, Wu Q, Ge B, Zhang L, Wang K, Wang X, Chang CR, Yao X. Single carbon vacancy traps atomic platinum for hydrogen evolution catalysis. *J Am Chem Soc* 2022;144:2171–8. <https://doi.org/10.1021/jacs.1c10814>.
- [24] Luo W, Wang Y, Luo L, Gong S, Wei M, Li Y, Gan X, Zhao Y, Zhu Z, Li Z. Single-atom and bimetallic nanoalloy supported on nanotubes as a bifunctional electrocatalyst for ultrahigh-current-density overall water splitting. *ACS Catal* 2022;12:1167–79. <https://doi.org/10.1021/acscatal.1c04454>.
- [25] Che S, Ta N, Yang F, Yan X, Liu H, Chen N, Sun S, Wang C, Jiang B, Sun Y, Wang Y, Li Y. One-pot construction of CoSe nanoparticles anchored on single-atomic-Co doped carbon for pH-universal hydrogen evolution. *Mater Chem Front* 2022;6: 3577–88. <https://doi.org/10.1039/d2qm00893a>.
- [26] Che S, Ta N, Yang F, Yang Y, Li Y. Interfacial electronic engineering of NiSe₂-anchored Ni–N–C composite electrocatalyst for efficient hydrogen evolution. *Catalysts* 2022;12. <https://doi.org/10.3390/catal12121525>.
- [27] Lei Y, Zhang L, Zhou D, Xiong C, Zhao Y, Chen W, Xiang X, Shang H, Zhang B. Construction of interconnected NiO/CoFe alloy nanosheets for overall water splitting. *Renew Energy* 2022;194:459–68. <https://doi.org/10.1016/j.renene.2022.05.124>.
- [28] Lei HS, Lili Zhang Yuanting, Xu Wenjing, Xiong Chengli, Chen Wenxing, Xu Xiang, Zhang Bing. Carbon-supported high-entropy Co–Zn–Cd–Cu–Mn sulfide nanoarrays promise high-performance overall water splitting. *Nano Res* 2022;15:6054–61.
- [29] Wu Y, Wang H, Ji S, Pollet BG, Wang X, Wang R. Engineered porous Ni₂P-nanoparticle/Ni₂P-nanosheet arrays via the Kirkendall effect and Ostwald ripening towards efficient overall water splitting. *Nano Res* 2020;13:2098–105. <https://doi.org/10.1007/s12274-020-2816-7>.
- [30] Sun H, Xu X, Yan Z, Chen X, Cheng F, Weiss PS, Chen J. Porous multishelled Ni₂P hollow microspheres as an active electrocatalyst for hydrogen and oxygen evolution. *Chem Mater* 2017;29:8539–47. <https://doi.org/10.1021/acs.chemmater.7b03627>.
- [31] Chai R, Zhou T, Sun D, Luo Y, Li J, Wu F. Bimetallic-MOF derived nickel-iron phosphide nanosheets on carbon cloth for efficacious oxygen evolution reaction.

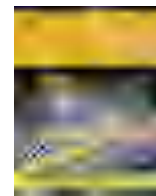
- Int J Hydrogen Energy 2022;47:36129–38. <https://doi.org/10.1016/j.ijhydene.2022.08.186>.
- [32] Choi S, Kwon J, Jo S, Kim S, Park K, Kim S, Han H, Paik U, Song T. Highly efficient and stable bifunctional electrocatalysts with decoupled active sites for hydrogen evolution and oxygen reduction reactions. *Appl Catal B Environ* 2021;298:120530. <https://doi.org/10.1016/j.apcatb.2021.120530>.
- [33] Lv XW, Xu WS, Tian WW, Wang HY, Yuan ZY. Activity promotion of core and shell in multifunctional core-shell Co₂P@NC electrocatalyst by secondary metal doping for water electrolysis and Zn-air batteries. *Small* 2021;17:1–13. <https://doi.org/10.1002/smll.202101856>.
- [34] Yan X, Che S, Yang F, Xu Z, Liu H, Li C, Yan L, Ta N, Sun S, Wei Q, Fang L, Li Y. Highly efficient water splitting catalyst composed of N, P-doped porous carbon decorated with surface P-enriched Ni₂P nanoparticles. 14. 2022. p. 20358–67. <https://doi.org/10.1021/acsami.1c14363>.
- [35] Shin C, Yu TH, Lee H, Lee B, Kwon S, Ili AG, Yu J. Applied Catalysis B : environmental Ru-loaded pyrrolic-N-doped extensively graphitized porous carbon for high performance electrochemical hydrogen evolution. *Appl Catal B Environ* 2023;334:122829. <https://doi.org/10.1016/j.apcatb.2023.122829>.
- [36] Zhao Q, Tan X, Ma T, Cao F, Xia Z, Liu H, Ning H, Li Z, Hu H, Wu M. Journal of Colloid and Interface Science Reinforced atomically dispersed Fe A N A C catalysts derived from petroleum asphalt for oxygen reduction reaction. *J Colloid Interface Sci* 2021;587:810–9. <https://doi.org/10.1016/j.jcis.2020.11.040>.
- [37] Li W, Liu J, Guo P, Li H, Fei B, Guo Y, Pan H. Co/CoP heterojunction on hierarchically ordered porous carbon as a highly efficient electrocatalyst for hydrogen and oxygen evolution. 2021, 2102134. <https://doi.org/10.1002/aenm.202102134>. 1–10.
- [38] Yan B, Liu Y, Zhang Y, Guo Y, Guo W, Chen L, Yu F, Wang G. Uniformly dispersed Fe 3 C (~5 nm) in Fe-N-doped carbon nanosheets derived from coal tar pitch as efficient electrocatalysts for oxygen reduction reaction. *Mater Lett* 2020;273:127861. <https://doi.org/10.1016/j.matlet.2020.127861>.
- [39] Qi JL, Xu QQ, Zhou D, Yin JZ, Jiang QK. Preparation of Cu single atoms on N-doped carbon materials with supercritical CO₂ deposition. *J Supercrit Fluids* 2021;171:105202. <https://doi.org/10.1016/j.supflu.2021.105202>.
- [40] Cai Z, Du P, Liang W, Zhang H, Wu P, Cai C, Yan Z. Single-atom-sized Ni-N₄ sites anchored in three-dimensional hierarchical carbon nanostructures for the oxygen reduction reaction. *J Mater Chem A* 2020;8:15012–22. <https://doi.org/10.1039/d0ta05326k>.
- [41] Liu H, Ma X, Hu H, Pan Y, Zhao W, Liu J, Zhao X, Wang J, Yang Z, Zhao Q, Ning H, Wu M. Robust NiCoP/CoP heterostructures for highly efficient hydrogen evolution electrocatalysis in alkaline solution. 2019. <https://doi.org/10.1021/acsami.9b00592>.
- [42] Chen L, Yang S, Qian K, Wei W, Sun C, Xie J. In situ growth of N-doped carbon coated CoNi alloy with graphene decoration for enhanced HER performance. *J Energy Chem* 2019;29:129–35. <https://doi.org/10.1016/j.jechem.2018.03.005>.
- [43] Meng W, Wang J, Zhang D, Xu J, Guo F, Zhang Y. Defective amorphous carbon-coated carbon nanotube-loaded ruthenium nanoparticles as efficient electrocatalysts for hydrogen production. 2023. p. 1–9. <https://doi.org/10.1002/sstr.202300098>.
- [44] Jiang M, Wang F, Yang F, He H, Yang J, Zhang W, Luo J, Zhang J, Fu C. Rationalization on high-loading iron and cobalt dual metal single atoms and mechanistic insight into the oxygen reduction reaction. *Nano Energy* 2022;93:106793. <https://doi.org/10.1016/j.nanoen.2021.106793>.
- [45] Liu Z, Sun S, Yang F, Liu H, Sun Y, Ta N, Zhang G, Che S, Li Y. Synergistic effect of Fe/Cu-N-C dual single-atom catalyst for C-H bond oxidation. *J Colloid Interface Sci* 2023;632:237–48. <https://doi.org/10.1016/j.jcis.2022.11.005>.
- [46] Jiang L, Shang J, Peng X, Li Z, Zhu M, Cheng Y, Xie P, Ren L. Single atom catalysts enable quasi-homogeneous synthesis of quinazoline. *Chem Eng J* 2023;474:145651. <https://doi.org/10.1016/j.cej.2023.145651>.
- [47] Hu C, Song E, Wang M, Chen W, Huang F, Feng Z, Liu J, Wang J. Partial-single-atom, partial-nanoparticle composites enhance water dissociation for hydrogen evolution. 2021, 2001881. <https://doi.org/10.1002/advs.202001881>. 1–10.
- [48] Cui M, Wang F, Zhao W, Zhang D, Liang R, Ou Q, Zhang S. Plasma-synthesized platinum single atom and nanoparticle catalysts for high-current – density hydrogen evolution. *Chem Eng J* 2023;460:141676. <https://doi.org/10.1016/j.cej.2023.141676>.
- [49] Chen D, Xu Z, Chen W, Chen G, Huang J, Huang J, Song C, Li C, Ken KC, Ostrikov. Just add water to split water: ultrahigh-performance bifunctional electrocatalysts fabricated using eco-friendly heterointerfacing of NiCo diselenides. *J Mater Chem A* 2020;8:12035–44. <https://doi.org/10.1039/d0ta02121k>.
- [50] Dang J, Yun S, Zhang Y, Yang J, Liu Z, Dang C, Wang Y, Deng Y. Constructing double-shell structured N-C-in-Co/N-C electrocatalysts with nanorod- and rhombic dodecahedron-shaped hollow morphologies to boost electrocatalytic activity for hydrogen evolution and triiodide reduction reaction. *Chem Eng J* 2022;449:137854. <https://doi.org/10.1016/j.cej.2022.137854>.
- [51] Hoa VH, Tran DT, Nguyen DC, Kim DH, Kim NH, Lee JH. Molybdenum and phosphorous dual doping in cobalt monolayer interfacial assembled cobalt nanowires for efficient overall water splitting. *Adv Funct Mater* 2020;30:1–12. <https://doi.org/10.1002/adfm.202002533>.
- [52] Jia S, Cheng Y, Huang Q, Li Q, Zhang Q. ScienceDirect One-step synthesis of Co₂P/N-P co-doped porous carbon composites derived from soybean derivatives as acidic and alkaline HER electrocatalysts. *Int J Hydrogen Energy* 2022;47:24796–806. <https://doi.org/10.1016/j.ijhydene.2022.05.242>.
- [53] Xu J, Zhong M, Song N, Wang C, Lu X. General synthesis of Pt and Ni co-doped porous carbon nanofibers to boost HER performance in both acidic and alkaline solutions. *Chin Chem Lett* 2023;34:107359. <https://doi.org/10.1016/j.ccllet.2022.03.082>.
- [54] Karim W, Spreafico C, Kleibert A, Gobrecht J, Vandevondele J, Ekinici Y, Van Bokhoven JA. Catalyst support effects on hydrogen spillover. *Nature* 2017;541:68–71. <https://doi.org/10.1038/nature20782>.
- [55] Li J, Hu J, Zhang M, Gou W, Zhang S, Chen Z, Qu Y, Ma Y. A fundamental viewpoint on the hydrogen spillover phenomenon of electrocatalytic hydrogen evolution. *Nat Commun* 2021;12:1–12. <https://doi.org/10.1038/s41467-021-23750-4>.



Contents lists available at ScienceDirect

Journal of Colloid and Interface Science

journal homepage: www.elsevier.com/locate/jcis



Interface and electronic structure regulation of Mo-doped NiSe₂-CoSe₂ heterostructure aerogel for efficient overall water splitting



Hongchen Liu, Fan Yang^{*}, Fengjiang Chen, Sai Che, Neng Chen, Siyuan Sun, Na Ta, Yang Sun, Ni Wu, Yankun Sun, Yongfeng Li^{*}

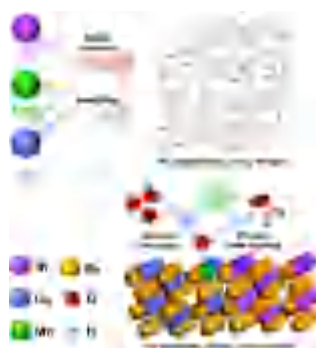
State Key Laboratory of Heavy Oil Processing, China University of Petroleum, Beijing 102249, China

h i g h l i g h t s

- Mo doped NiSe₂-CoSe₂ aerogel was firstly prepared via facile gelation and selenizing.
- Mo doped NiSe₂-CoSe₂ aerogels exhibited good performances in HER, OER and overall water splitting.
- Mo doping promoted the nucleophilic adsorption of water molecules on the heterointerface.
- DFT calculations proved the optimal adsorption of reaction intermediates in HER and OER.

g r a p h i c a l a b s t r a c t

In this work, a series of Mo doped NiSe₂-CoSe₂ heterostructure aerogels were designed and synthesized via facile spontaneous gelation and selenium vapor deposition process. Fine regulated Mo doping improved the electropositivity and adjusted the charge density of the NiSe₂-CoSe₂ heterointerface, which optimized the adsorption of water molecule and other reaction intermediates in cathode and anode reactions. Benefit from the improvements, the optimal Mo doped NiSe₂-CoSe₂ aerogel exhibited extremely low overpotentials in both HER and OER, and the cell voltage in overall water splitting was lower than that of noble-metal catalysts.



a r t i c l e i n f o

Article history:
Received 14 December 2022
Revised 14 February 2023
Accepted 27 February 2023
Available online 2 March 2023

Keywords:
Electronic regulation
Heterostructure
Mo doping
Aerogel
Overall water splitting

a b s t r a c t

Transition metal selenides (TMSes) with cubic pyrite-type crystal structure have been widely explored as electrocatalysts for oxygen evolution reaction (OER), but the insufficient hydrogen evolution reaction (HER) performance hinders the application of overall water splitting. Herein, we designed and prepared a Mo doped NiSe₂-CoSe₂ heterostructure aerogel as bifunctional electrocatalyst via facile spontaneous gelation and selenium vapor deposition. The active sites on the heterointerface possessed desirable Gibbs free energy of hydrogen adsorption, leading to better HER performance than single NiSe₂ or CoSe₂. Moreover, systematically experimental research and density functional theory (DFT) calculations revealed that fine regulated Mo doping improved the electropositivity of heterostructure, promoting the nucleophilic adsorption of water molecule. Benefit from those improvements, the optimal Mo doped NiSe₂-CoSe₂ aerogel exhibited an extremely low overpotential of 57 mV at the current density of 10 mA·cm⁻² for HER with a small Tafel slope value of 38 mV·dec⁻¹. Meanwhile, Mo doping provided

^{*} Corresponding authors.

E-mail addresses: yangfan@cup.edu.cn (F. Yang), yfli@cup.edu.cn (Y. Li).

higher electron transfer efficiency and better adsorptive property toward reaction intermediate in anodic reaction, resulting in low overpotential of 270 mV at the current density of 100 mA·cm⁻² for OER with good electrocatalytic stability. This work provides an anticipated perspective of rational combination of metal doping and heterostructure for advanced electrocatalysts.

© 2023 Elsevier Inc. All rights reserved.

1. Introduction

With the ever-worsening global energy crisis and environmental pollution, the transformation from traditional fossil fuel to green hydrogen energy has attracted huge attention [1–3]. Electrochemical water splitting, consisting of cathodic hydrogen evolution reaction (HER) and anodic oxygen evolution reaction (OER), has been considered as a promising approach for hydrogen generation [4,5]. Until now, the Pt-based materials and Ru/Ir-based oxides are still known as the best electrocatalysts for HER and OER due to their high activity and excellent stability [6]. However, the low abundance and high prices of those noble metal-based catalysts limit their large-scale application. Meanwhile, most of the reported electrocatalysts can exhibit good performance toward only one side of HER or OER, so that the incompatibility and different reaction kinetics in cathode and anode may lead to inferior efficiency in overall water splitting [7,8]. Therefore, it is highly imperative to design and construct non-noble metal bifunctional electrocatalysts with favorable performance for efficient water splitting.

Among various obtained electrocatalysts, transition-metal selenides (TMSes) are emerging as one of the most promising bifunctional catalysts due to the high intrinsic conductivity, suitable d-electron configuration and rich chemical states [9]. In particular, TMSes with cubic pyrite-type crystal structure (e.g., NiSe₂, CoSe₂) possess the surfaces that favor oxidation to generate active sites with superior OER performance, which significantly reduces the potential of anode reaction and cell voltage of overall water splitting [10–12]. However, the cubic phases TMSes exhibit deficient activity of HER, which limits their application in bifunctional electrocatalytic water splitting [13,14]. Recent studies indicate that the construction of heterostructure allows the combination of high-performance HER and OER active components and enhances the charge transfer efficiency at the heterointerface, which can effectively improve the bifunctional electrocatalytic activity of homogeneous catalysts [15–18]. Based on the theory, many TMSes-based heterostructure electrocatalysts have been developed [19–24]. For instance, Chen et al. [21] designed the NiSe₂-CoSe₂ heterogeneous structure based on Ni-Co foam. In contrast with single NiSe₂ or CoSe₂, the NiSe₂-CoSe₂ had the density of states (DOS) that near the Fermi-level, indicating that the heterostructure possessed favorable surface for hydrogen adsorption. Although the hydrogen adsorption property can be improved by heterostructures, the kinetic of the Volmer step (the step of water adsorption and dissociation) is still limited, preventing the occurrence of HER on surface of TMSes. Hence, it is extremely important to facilitate the interfacial adsorption of water molecules. Recent mechanistic researches reveal that Mo doping can provide high electropositivity, which promotes the nucleophilic adsorption of water and improves the charge transfer efficiency on the surface of electrocatalysts [25–28]. Zhou et al. [27] synthesized a series of Mo doped CoSe electrocatalysts, where the doping Mo adjusted the electron density of CoSe and provided moderate adsorption property toward hydrogen, resulting in favorable HER performance with low Tafel slope. In addition, Mo doping can contribute to the electrocatalytic performance of TMSes on anodic reaction as well. For instance, Huang et al. [28] built the Mo doping CoSe₂ nanosheets on Ni Foam, where the Mo element with high electropositivity promoted

the generation of O* in Co site and caused better electrocatalytic activity of OER. To sum up, it is of great relevance to develop high performance TMSes-based catalysts with Mo doping for overall water splitting.

Herein, a novel Mo doped NiSe₂-CoSe₂ heterostructure aerogel was successfully synthesized via facile gelation and selenium vapor deposition. Based on our previous experience, the aerogel structure was constituted by interconnect network skeleton, which could provide abundant active sites and mass transfer pathway [29–31]. Moreover, with the introduction of Mo element, the water adsorption property and surface electron transport efficiency were significantly improved, leading to extremely low Tafel slope toward HER. Besides, the results of DFT calculation indicated that the added Mo element could optimize the corresponding Gibbs free energy along both HER and OER, thus improving the intrinsic activity of the NiSe₂-CoSe₂ heterostructure for bifunctional electrocatalysis. As expected, the Mo doped NiSe₂-CoSe₂ exhibited excellent bifunctional electrocatalytic activity and an ultralow cell voltage to drive overall water splitting.

2. Experimental section

2.1. Materials and reagents

Nickle chloride hexahydrate (NiCl₂·6H₂O, 99%), cobalt chloride hexahydrate (CoCl₂·6H₂O, 99%) and sodium molybdate dihydrate (Na₂MoO₄·2H₂O, 98%) were purchased from Sinopharm Chemical Reagent Co. Sodium borohydride (NaBH₄, 98%) was purchased from Tianjin Fuchen Chemical Reagents Factory. Selenium (Se, 99.99%, powder, 100) was purchased from Adamas-beta. Platinum-carbon (Pt/C, 20 wt%) and ruthenium oxide (RuO₂, 99.9%) were purchased from Alfa Aesar.

2.2. Synthesis of Mo doped Ni-Co aerogel

In a typical preparation of Mo doped Ni-Co aerogel (Mo_x-Ni-Co), 20 mL NaBH₄ (0.1 M) solution was quickly dropped into the mixed solution of 5 mL NiCl₂ (0.05 M) and 5 mL CoCl₂ (0.05 M). As the initial formation of the hydrogel skeleton was observed, Na₂MoO₄ (0.05 M) solution was evenly add into the mixed solution. To optimize the Mo doping, different volumes of Na₂MoO₄ solution (1.5, 2.5 and 3.5 mL) were conducted to synthesize various Mo doped Ni-Co precursors. Based on the mole ratio of Mo:Ni:Co (0.3:1:1, 0.5:1:1 and 0.7:1:1), the samples were shortly named as Mo_{0.3}-Ni-Co, Mo_{0.5}-Ni-Co and Mo_{0.7}-Ni-Co, respectively. 8 h later, the Mo doped Ni-Co hydrogel was constructed at the bottom of the flask. After 20 h freeze drying, moisture was removed and the Mo doped Ni-Co aerogel was obtained.

2.3. Synthesis of Mo doped NiSe₂-CoSe₂ aerogel

To fabricate the Mo doped NiSe₂-CoSe₂ aerogel (Mo_x-NiSe₂-CoSe₂), 20 mg of Mo doped Ni-Co aerogel precursor and excess Se powder were placed at two separate positions in porcelain boats respectively, of which Se powder was placed on the upstream side of the furnace. Then, the samples were heated up to 400 °C by 5 °·C·min⁻¹ and maintained at this temperature for 120 min with Ar

gas flowing at 50 sccm to synthesize the Mo doped NiSe₂-CoSe₂ aerogel. The samples with different amounts of Mo doping were shortly named as Mo_{0.3}-NiSe₂-CoSe₂, Mo_{0.5}-NiSe₂-CoSe₂ and Mo_{0.7}-NiSe₂-CoSe₂, respectively.

2.4. Characterizations

The structure and morphology of prepared samples were analyzed by scanning electron microscope (SEM, SU8010) at an accelerating voltage of 5 kV and transmission electron microscopy (TEM, Tecnai G2 F20). The crystal structures were characterized by powder X-ray diffraction (XRD, Bruker D8 Advance). The chemical states were manifested by X-ray photoelectron spectroscopy (XPS, Thermo Fisher K-Alpha) with an Al K X-ray source. The contact angle of the material in 1 M KOH electrolyte was measured by the trapped droplet method (Kruss DSA20 system).

2.5. Electrochemical measurements

Samples on carbon-cloth-based electrodes were prepared for all the electrochemical measurements. In this context, 5.0 mg of sample was dispersed in the mixed solution with 0.25 mL ethanol, 0.25 mL deionized water and containing 20 L of Nafion (5%) under sonication for 30 min to form a homogeneous catalyst ink. Then, the achieved ink was drop-cast onto the surface of carbon cloth (1 cm × 1 cm) followed by drying at 60 °C to achieve the loading amount of 1.0 mg·cm⁻² for sample on carbon cloth. For a comparison, Pt/C and RuO₂ on carbon cloth were also prepared for evaluating HER, OER and overall water splitting by the same method.

All the electrochemical properties of the samples were measured on a CHI 760 electrochemical workstation (CH Instruments, Inc., Shanghai) integrated with a three-electrode system at room temperature. Sample modified carbon cloth, graphite rod, and Hg/HgO acted as working, counter, and reference electrodes, respectively. The conversion potential of E (RHE) was obtained according to Eq (1):

$$E(\text{RHE}) = E(\text{Hg}=\text{HgO}) + 0.059 \times \text{pH} + 0.098 \quad (1)$$

Electrocatalytic activities of HER and OER were evaluated by linear-sweep voltammetry (LSV) in 1 M KOH solution (pH = 14) at a scan rate of 5 mV·s⁻¹ with 80% iR-correction. The potential ranges toward HER and OER were -0.8 to -1.4 V and 0 to 0.8 V vs. standard Hg/HgO electrode, respectively. Further, the performance of overall water splitting was also measured by LSV on a two-electrodes system with the optimized sample under the operating voltage from 1.0 to 2.0 V (without iR-correction). Electrochemical impedance spectroscopy (EIS) measurement was applied to evaluate the charge-transfer resistances of samples at a frequency range of 0.01 to 10⁵ Hz. The testing voltages were set to -1.1 V and 0.6 V vs. standard Hg/HgO for HER and OER, respectively. Double-layer capacitance (C_{dl}) values were employed to appraise the electrochemical surface area (ECSA) of samples, which were calculated by the cyclic voltammetry (CV) results in the non-Faradaic potential region ranging from -0.3 to -0.5 V vs. standard Hg/HgO electrode at 50, 100, 150 and 200 mV·s⁻¹. The hydrogen and oxygen generation experiments adopted a simple drainage method, where the volume of the discharged gas was recorded every 10 min. The cyclic stability of obtained samples was measured by the LSV tests that before and after 2000 CV tests. Besides, the chronoamperometric curves (I-t) were used to measure the electrocatalytic stability. For HER and OER process, the voltages were set to achieve the initial current densities of 10, 100 and 200 mA·cm⁻² for 20 h. For the overall water splitting process, the I-t curve was measured at the operating voltage to achieve the current density of 10 mA·cm⁻².

2.6. Theoretical calculation details

Density functional theory (DFT) calculation was performed by DMol³ code as implemented in Materials Studio. The generalized gradient approximation of Perdew-Burke-Ernzerhof (GGA-PBE) function was used to treat all the energy changes. The core treatment was effective core potentials (ECP) and the basis set was DNP v4.4. The k-point was set as 3 × 3 × 1 and the thickness of vacuum region was 15 Å. The NiSe₂-CoSe₂ models were formed by NiSe₂ (2 1 0) and CoSe₂ (2 1 0) crystal faces, and the MoSe₂-NiSe₂-CoSe₂ model further combined the MoSe₂ (1 0 3) crystal face. The typical NiSe₂-CoSe₂ structure was modified by U × 4 and V × 2 super cell of original NiSe₂ (2 1 0) and CoSe₂ (2 1 0), where the Co atom in CoSe₂ was partially substituted by Mo atom to build the Mo-NiSe₂-CoSe₂ structure. The water adsorption energy on the obtained surfaces (DE_{H₂O}) were calculated by Eq (2):

$$DE_{\text{H}_2\text{O}} = E_{(\text{surf}+\text{H}_2\text{O})} - E_{\text{surf}} - E_{\text{H}_2\text{O}} \quad (2)$$

Where the E_{surf} and E_{H₂O} were related to the energy of bare surface and single H₂O molecule, and the E_(surf+H₂O) represented the energy of total system with one adsorbed H atom in each unit cell. Moreover, the adsorption energies of hydrogen atom (DG_{H*}) on the structures were calculated by Eq (3):

$$DG_{\text{H}^*} = DE_{\text{H}^*} + \text{DZPE} - \text{TDS} \quad (3)$$

Where the DE_{H*}, DZPE, T and DS were the binding energy of hydrogen atom, zero-point energy change, temperature (room temperature, 298.15 K), and entropy change for the adsorption reaction, respectively. Herein, the DE_{H*} was calculated as Eq (4):

$$DE_{\text{H}^*} = E_{(\text{surf}+\text{H}^*)} - E_{\text{surf}} - 1/2E_{\text{H}_2} \quad (4)$$

Where the E_{H₂} was related to the energy single H₂ molecule, and the E_(surf+H*) represented the energy of total system with one adsorbed H atom in each unit cell. Additionally, the free energy of reaction intermediates in OER (DG_i) could be calculated by Eq (5):

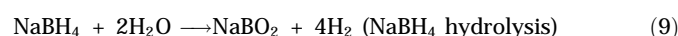
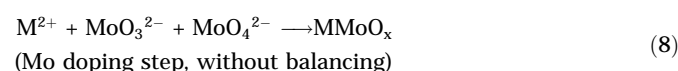
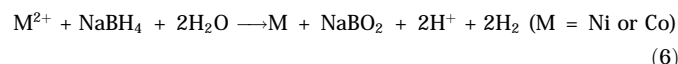
$$DG_i = DE_i + \text{DZPE} - \text{TDS} + DG_{\text{U}} \quad (5)$$

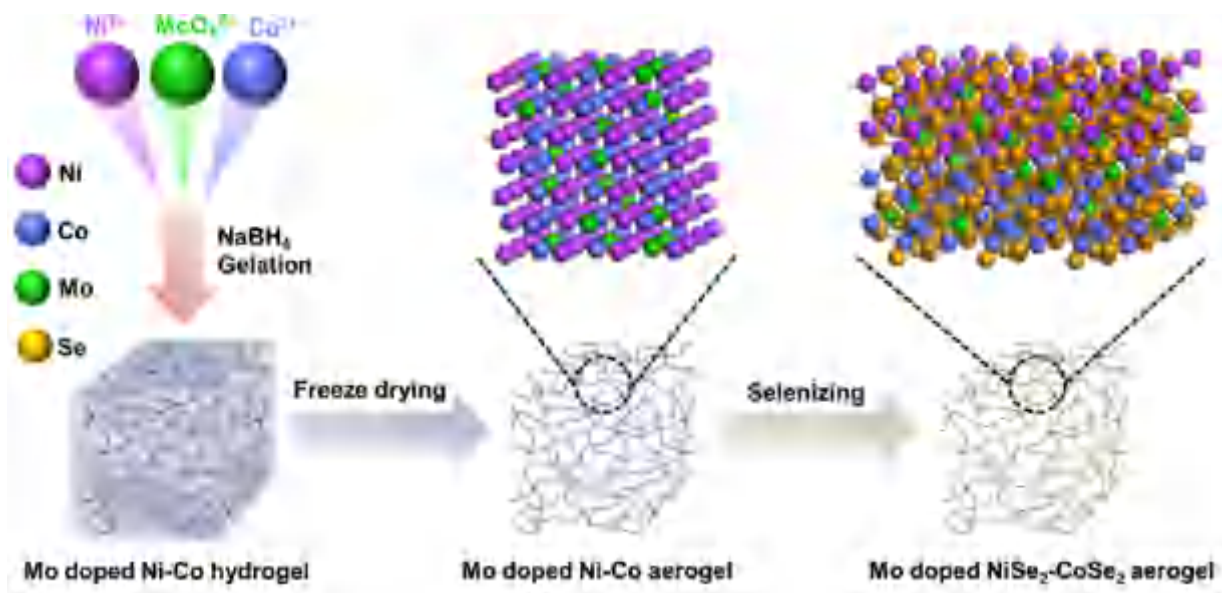
Herein, DE_i was the binding energy of reaction intermediates (OH*, O* and OOH*) on the obtained surfaces. Besides, DG_U = -eU and U was the potential vs. RHE (set as 0 V).

3. Results and discussion

3.1. Morphological and structural characterizations

The Mo doped NiSe₂-CoSe₂ aerogels (Mo_x-NiSe₂-CoSe₂) were fabricated through facile gelation and vapor selenation processes (Scheme 1). First of all, Mo_x-Ni-Co hydrogels (X = 0.3, 0.5, and 0.7, representing the mole ratio of Mo:Ni:Co = 0.3:1:1, 0.5:1:1, and 0.7:1:1, respectively) were constructed through a series of reduction reactions with precisely controlled Mo contents. The involved reactions were described as Eqs. (6)–(9) [29,32,33]:

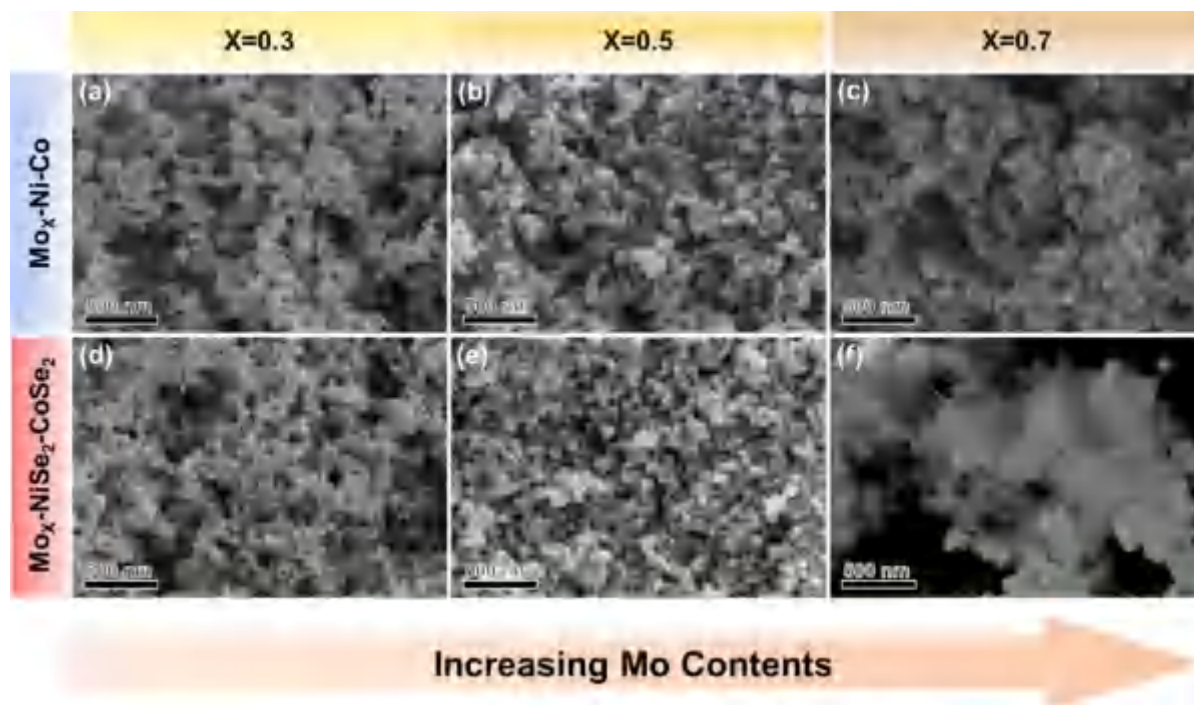


Scheme 1. Schematic illustration for the synthesis of $\text{Mo}_x\text{-Ni-Co}$ and $\text{Mo}_x\text{-NiSe}_2\text{-CoSe}_2$ aerogels.

Herein, the reduction of Ni, Co, Mo elements (Eqs. (6)–(7)) and the hydrolysis of NaBH_4 produced hydrogen bubbles, which served as the gas template and induced the formation of porous interconnected networks [33,34]. Then, the corresponding $\text{Mo}_x\text{-Ni-Co}$ aerogels were produced by freeze drying to remove the solvent from gel structure. Finally, all the $\text{Mo}_x\text{-Ni-Co}$ aerogels were annealed under selenium vapor to form the $\text{Mo}_x\text{-NiSe}_2\text{-CoSe}_2$ aerogels.

The scanning electron microscope (SEM) images in Fig. 1(a)–(c) illustrated that all the $\text{Mo}_x\text{-Ni-Co}$ aerogels possessed interconnected network skeleton formed by Mo-Ni-Co alloy nanoparticles. As the contents of Mo were gradually increased, the particle size in the skeleton of aerogels progressively improved with slight fusion.

Compared with Ni^{2+} and Co^{2+} , the MoO_4^{2-} with high valence state Mo element was difficult to be reduced by NaBH_4 , resulting in lower rate of hydrogen generation and leading to smaller pore size in the skeleton of aerogels [29]. Besides, the doped Mo with larger atomic radius caused the increasing of particle size as well [28,35]. After selenization, the $\text{Mo}_{0.3}\text{-NiSe}_2\text{-CoSe}_2$ (Fig. 1(d)) and $\text{Mo}_{0.5}\text{-NiSe}_2\text{-CoSe}_2$ (Fig. 1(e)) aerogels maintained the similar porous network structure as the corresponding precursors. In contrast, fluffy structure could be observed on the surface of $\text{Mo}_{0.7}\text{-NiSe}_2\text{-CoSe}_2$ (Fig. 1(f)), demonstrating that the excess Mo element reacted with selenium vapor and induced the generation of the unique structure, which was consisted with the previous reports [27,36]. More-

Fig. 1. (a–c) SEM images of $\text{Mo}_x\text{-Ni-Co}$ aerogels. (d–f) SEM images of $\text{Mo}_x\text{-NiSe}_2\text{-CoSe}_2$ aerogels.

over, the low-resolution transmission electron microscopy (TEM) image of typical $\text{Mo}_{0.5}\text{-NiSe}_2\text{-CoSe}_2$ exhibited the fluffy structure of aerogel (Fig. 2(a)) with massive exposed active sites [37]. The high-resolution TEM image exhibited clear lattice fringes with interplanar distances of 0.212 and 0.209 nm, corresponding to the (220) crystal planes of NiSe_2 and CoSe_2 , respectively (Fig. 2(b)) [38]. The structure composition was further confirmed by the homogeneous distribution of Ni, Co, and Mo signals in the STEM-mapping images of both $\text{Mo}_{0.5}\text{-Ni-Co}$ and $\text{Mo}_{0.5}\text{-NiSe}_2\text{-CoSe}_2$ aerogels (Figure S1). Furthermore, the distributions of Se element matched that of Ni and Co very well (Fig. 2(c)), revealing the successful formation of selenides.

The crystalline structures of $\text{Mo}_{0.5}\text{-NiSe}_2\text{-CoSe}_2$ aerogel and its precursor were investigated by powder X-ray diffraction (XRD, Fig. 3(a)). Only an unobvious characteristic peak of CoNi alloy (PDF#97–010–0838) could be observed in the pattern of $\text{Mo}_{0.5}\text{-Ni-Co}$, indicating that the amorphous NiMoO_x and CoMoO_x were the main components of the precursor, which coincided well with the reaction mechanism [29,33]. Moreover, due to the recrystallization and generation of selenides, the apparent diffraction peaks corresponding to $(\text{CoNi})\text{(Se}_2)_2$ (PDF#97–062–4483) appeared in the pattern of $\text{Mo}_{0.5}\text{-NiSe}_2\text{-CoSe}_2$, indicating the formation of Ni-Co bimetallic selenides heterostructure [21,39]. Upon the addition of Mo, the diffraction peaks of CoNi alloy and $(\text{CoNi})\text{(Se}_2)_2$ gradually decreased but without shifting in position, and almost disappeared in the pattern of $\text{Mo}_{0.7}\text{-NiSe}_2\text{-CoSe}_2$ (Fig. S2(a)), illustrating the overgrowth of the Mo-based amorphous phase in the structure [27,36]. Notably, with the increasing of Mo contents, the diffraction peaks of $(\text{CoNi})\text{(Se}_2)_2$ broadened to varying degrees, demonstrating that the doped Mo element replaced the Ni and Co in the heterostructure and resulted in grain refinement (Fig. S2(b)) [28].

The X-ray photoelectron spectroscopy (XPS) analysis was applied to comparably analyze the surface chemical composition and oxidation states of the obtained samples. The survey spectra of $\text{Mo}_{0.5}\text{-Ni-Co}$ and $\text{Mo}_{0.5}\text{-NiSe}_2\text{-CoSe}_2$ aerogels revealed the coex-

istence of Mo, Ni, Co and Mo, Ni, Co, Se fundamental elements, while the specific signal of O 1 s resulted from superficial oxidation or physical adsorption (Fig. 3(b)) [20]. Upon the high-resolution spectrum of Ni 2p, except for the two satellite peaks at 861.2 and 879.9 eV, $\text{Mo}_{0.5}\text{-Ni-Co}$ aerogel exhibited two major peaks at 855.7 and 873.6 eV, which were vested in Ni^{2+} and assigned to Ni 2p_{3/2} and Ni 2p_{1/2}, respectively (the upper part of Fig. 3(c)). The other two peaks at 852.2 and 869.7 eV were assigned to Ni^{3+} [19]. Similarly, the Co 2p spectrum of $\text{Mo}_{0.5}\text{-Ni-Co}$ aerogel possessed two major peaks of Co^{2+} (780.9 and 796.9 eV), two peaks of Co^{2+} (777.7 and 792.7 eV), and two satellite peaks (785.3 and 802.9 eV), respectively (the upper part of Fig. 3(d)) [21]. Besides, the high-resolution Mo 3d spectrum of $\text{Mo}_{0.5}\text{-Ni-Co}$ included three peaks at 229.5, 232.2, and 235.2 eV, corresponding to Mo 3d_{5/2}, Mo 3d_{3/2} (Mo^{4+}), and Mo^{6+} (the upper part of Fig. 3(e)) [40]. After selenization, the peaks of Ni 2p_{3/2}, Co 2p_{3/2}, and Mo 3d_{3/2} exhibited distinct positive shift of 0.5 eV, 0.6 eV and 0.1 eV in the spectra of $\text{Mo}_{0.5}\text{-NiSe}_2\text{-CoSe}_2$ (Fig. R2(a)-(b)), demonstrating the Se element with electron-withdrawing properties adsorbed electrons from Ni and Co in the selenide aerogel. (the lower part of Fig. 3-(c)-(e)), demonstrating the Se element with electron-withdrawing properties affected the electronic structures of metals in the selenide aerogel. Besides, the Se 3d spectrum of $\text{Mo}_{0.5}\text{-NiSe}_2\text{-CoSe}_2$ was revealed in Fig. 3(f), where peaks at 54.3 and 55.2 eV were assigned to Se^{2-} of Se 3d_{5/2} and Se 3d_{3/2}, and the peak at 59.4 eV originated from SeO_x generated by surface oxidation [41]. Furthermore, the Ni 2p and Co 2p spectra of $\text{Mo}_{0.5}\text{-NiSe}_2\text{-CoSe}_2$ and our pervious $\text{NiSe}_2\text{-CoSe}_2$ results were in sharp contrast to illustrate the influence of the doped Mo element (Figure S3). After Mo doping, the Ni 2p_{3/2} and Co 2p_{3/2} peaks presented obvious negative shift of 1.10 eV and 0.1 eV, respectively, and the ratio of $\text{Ni}^{3+}/\text{Ni}^{2+}$ and $\text{Co}^{3+}/\text{Co}^{2+}$ significantly decreased. These results suggested that the high-electropositive Mo was successfully doped into the $\text{NiSe}_2\text{-CoSe}_2$ heterostructures and donated electrons to nearby elements [42].

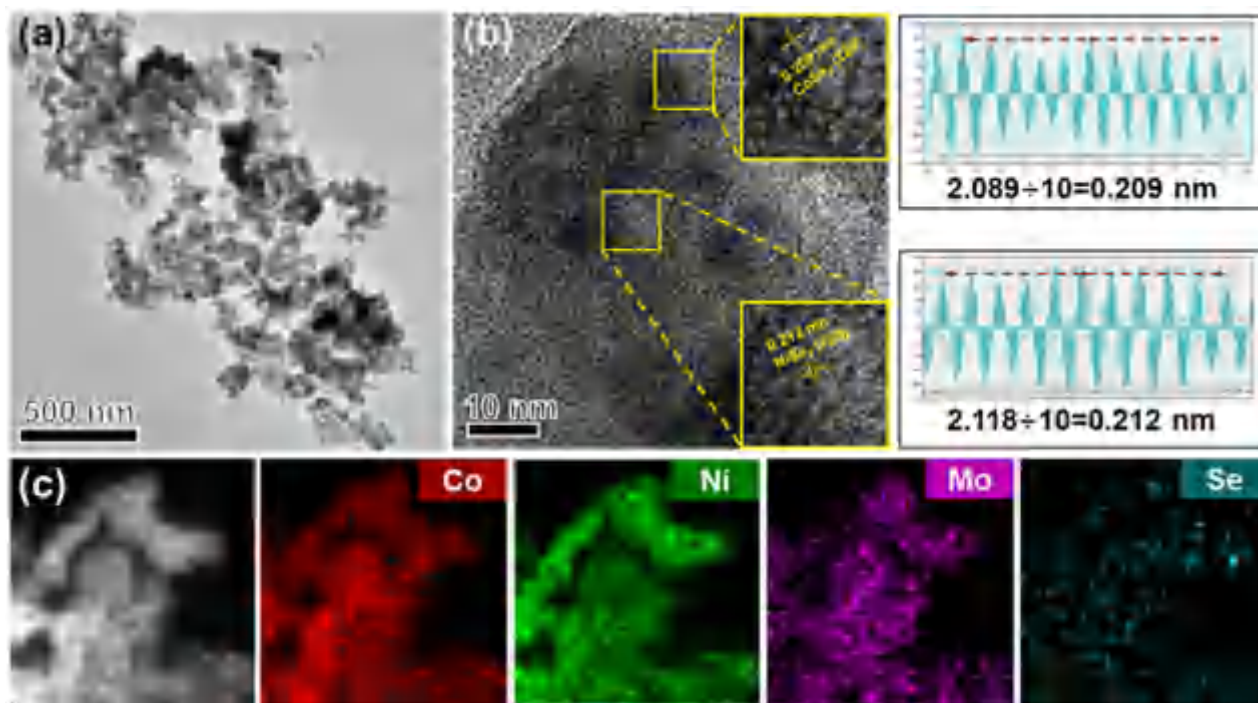


Fig. 2. (a) TEM image of $\text{Mo}_{0.5}\text{-NiSe}_2\text{-CoSe}_2$ aerogel. (b) HRTEM image of $\text{Mo}_{0.5}\text{-NiSe}_2\text{-CoSe}_2$ aerogel with lattice fringe of NiSe_2 and CoSe_2 (c) STEM image of $\text{Mo}_{0.5}\text{-NiSe}_2\text{-CoSe}_2$ aerogel and its corresponding EDX mapping of Co, Ni, Mo, and Se.

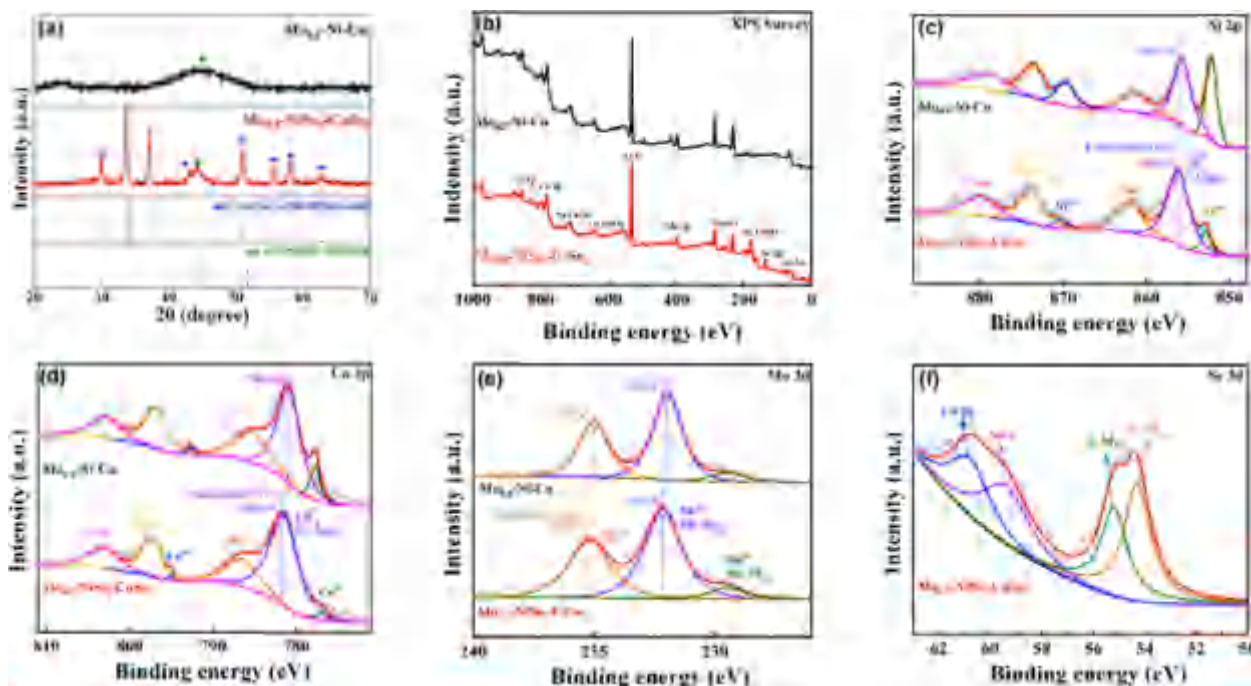
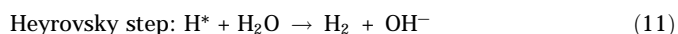
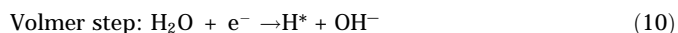


Fig. 3. (a) XRD patterns of $\text{Mo}_{0.5}\text{-Ni-Co}$ and $\text{Mo}_{0.5}\text{-NiSe}_2\text{-CoSe}_2$ aerogels comparison samples. (b) XPS survey spectrum of $\text{Mo}_{0.5}\text{-Ni-Co}$ and $\text{Mo}_{0.5}\text{-NiSe}_2\text{-CoSe}_2$ aerogels. (c-d) High resolution Ni 2p and Co 2p XPS spectra of $\text{Mo}_{0.5}\text{-Ni-Co}$ and $\text{Mo}_{0.5}\text{-NiSe}_2\text{-CoSe}_2$ aerogels. (e) High resolution Mo 3d XPS spectra of $\text{Mo}_{0.5}\text{-Ni-Co}$ and $\text{Mo}_{0.5}\text{-NiSe}_2\text{-CoSe}_2$ aerogels. (f) High resolution Se 3d XPS spectra of $\text{Mo}_{0.5}\text{-NiSe}_2\text{-CoSe}_2$ aerogel.

3.2. Electrocatalytic activity toward hydrogen evolution reaction

The electrocatalytic hydrogen evolution reaction (HER) activities of prepared $\text{Mo}_x\text{-NiSe}_2\text{-CoSe}_2$ aerogels were investigated through linear-sweep voltammetry (LSV) test in 1.0 M KOH under a scan rate of $5 \text{ mV}\cdot\text{s}^{-1}$ (Fig. 4(a)), and the overpotentials at different current densities were shown in Fig. 4(b)). The $\text{Mo}_{0.5}\text{-NiSe}_2\text{-CoSe}_2$ exhibited a lower overpotential of $57 \text{ mV}@10 \text{ mA}\cdot\text{cm}^{-2}$ than that of the $\text{Mo}_{0.3}\text{-NiSe}_2\text{-CoSe}_2$ ($63 \text{ mV}@10 \text{ mA}\cdot\text{cm}^{-2}$) and $\text{Mo}_{0.7}\text{-NiSe}_2\text{-CoSe}_2$ aerogels ($105 \text{ mV}@10 \text{ mA}\cdot\text{cm}^{-2}$), demonstrating its optimal content of Mo toward HER. Compared with the $\text{NiSe}_2\text{-CoSe}_2$ ($65 \text{ mV}@10 \text{ mA}\cdot\text{cm}^{-2}$, Fig. S4(a)), the optimized $\text{Mo}_{0.5}\text{-NiSe}_2\text{-CoSe}_2$ revealed better HER performance, which further proved the significant advantage of Mo doping in selenides heterostructure. Benefited from the improvement, the overpotential at $10 \text{ mA}\cdot\text{cm}^{-2}$ of $\text{Mo}_{0.5}\text{-NiSe}_2\text{-CoSe}_2$ was close to that of Pt/C (34 mV), and the overpotentials at high current densities ($165 \text{ mV}@100 \text{ mA}\cdot\text{cm}^{-2}$ and $211 \text{ mV}@200 \text{ mA}\cdot\text{cm}^{-2}$) were significantly superior to those of noble-metal catalyst ($212 \text{ mV}@100 \text{ mA}\cdot\text{cm}^{-2}$ and $350 \text{ mV}@200 \text{ mA}\cdot\text{cm}^{-2}$). Meanwhile, compared with recently reported TMSe-based or heterostructure-based materials, the $\text{Mo}_{0.5}\text{-NiSe}_2\text{-CoSe}_2$ possessed a lower overpotential (Fig. 4(c)) [7,19–22,26–28,43]. The origin of excellent HER performance was analyzed by the Tafel slopes (Figs. 4(d) and S4(b)). The Tafel slope value of $\text{Mo}_{0.5}\text{-NiSe}_2\text{-CoSe}_2$ was $38 \text{ mV}\cdot\text{dec}^{-1}$, which was close to that of Pt/C ($34 \text{ mV}\cdot\text{dec}^{-1}$) and lower than that of $\text{NiSe}_2\text{-CoSe}_2$ ($58 \text{ mV}\cdot\text{dec}^{-1}$), $\text{Mo}_{0.3}\text{-NiSe}_2\text{-CoSe}_2$ ($46 \text{ mV}\cdot\text{dec}^{-1}$), and $\text{Mo}_{0.7}\text{-NiSe}_2\text{-CoSe}_2$ ($64 \text{ mV}\cdot\text{dec}^{-1}$). For the reaction mechanism of HER in an alkaline solution, there were three major steps: Volmer, Heyrovsky, and Tafel steps, which could be described as Eqs. (10)–(12) [44]:



According to these equations, the theoretical values of the Tafel slopes for the three steps are 120, 40, and $30 \text{ mV}\cdot\text{dec}^{-1}$, respectively [21]. Apparently, the $\text{Mo}_{0.5}\text{-NiSe}_2\text{-CoSe}_2$ conquered the barrier of water adsorption and dissociation process and followed the Heyrovsky mechanism, revealing the favorable HER kinetics. According to the previous researches, the Ni and Co sites in the selenides heterostructure possessed good water dissociation properties, and the doped Mo element with high-electropositivity enhanced the nucleophilic adsorption of water molecule, which resulted in the lower additional energy barrier of Volmer step [25]. Besides, the Nyquist plot (Fig. 4(e)) unraveled that the $\text{Mo}_{0.5}\text{-NiSe}_2\text{-CoSe}_2$ possessed a lower calculated charge transfer resistance (R_{ct}) of 10.90 X than that of $\text{Mo}_{0.3}\text{-NiSe}_2\text{-CoSe}_2$ (14.57 X) and $\text{Mo}_{0.7}\text{-NiSe}_2\text{-CoSe}_2$ (35.16 X), suggesting that the moderate Mo doping well modified the electronic structure of NiSe_2 and CoSe_2 , which was further confirmed by the fastest reaction kinetics and smallest Tafel slope in HER among the obtained samples [8]. The cyclic stability was measured by the LSV tests that before and after 2000 cyclic voltammetry (CV) cycles (Fig. 4(f)). The current density revealed negligible attenuation after CV cycles, demonstrating the excellent cyclic stability of $\text{Mo}_{0.5}\text{-NiSe}_2\text{-CoSe}_2$ toward HER. In addition, the long-term stability of $\text{Mo}_{0.5}\text{-NiSe}_2\text{-CoSe}_2$ aerogel was tested by chronoamperometry under the voltages to achieve different initial current densities of $10 \text{ mA}\cdot\text{cm}^{-2}$, $100 \text{ mA}\cdot\text{cm}^{-2}$ and $200 \text{ mA}\cdot\text{cm}^{-2}$ (Fig. 4(g)–(i)). After 20 h, the current density retained more than 95% of the initial value for all the three tests, which demonstrated the favorable durability of $\text{Mo}_{0.5}\text{-NiSe}_2\text{-CoSe}_2$ aerogel.

3.3. Electrocatalytic activity towards oxygen evolution reaction and overall water splitting

For all three $\text{Mo}_x\text{-NiSe}_2\text{-CoSe}_2$ aerogels, the oxygen evolution reaction (OER) activities were evaluated through LSV in 1.0 M KOH under a scan rate of $5 \text{ mV}\cdot\text{s}^{-1}$ (Fig. 5(a)), and the overpotentials at different current densities were shown in Fig. 5(b)). The onsets of oxidation peak generation were observed at around 1.10 V in

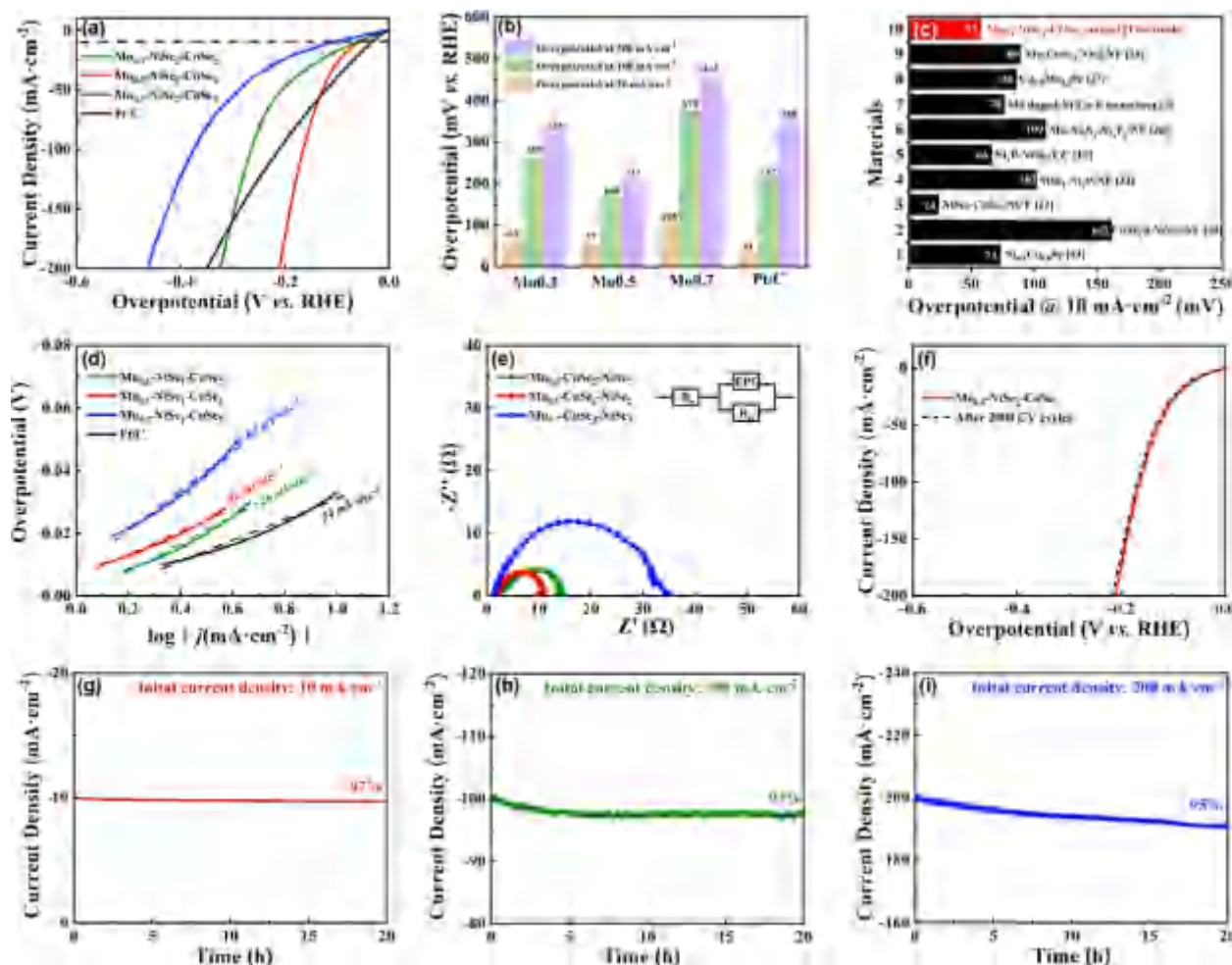


Fig. 4. (a) Polarization LSV curves of $\text{Mo}_x\text{-NiSe}_2\text{-CoSe}_2$ aerogels and Pt/C toward HER in 1.0 M KOH. (b) The overpotentials of obtained samples at different current densities. (c) Performance comparison of the optimized $\text{Mo}_{0.5}\text{-NiSe}_2\text{-CoSe}_2$ aerogel and published references. (d) Tafel slopes of $\text{Mo}_x\text{-NiSe}_2\text{-CoSe}_2$ aerogels and Pt/C toward HER in 1.0 M KOH. (e) Nyquist plot of $\text{Mo}_x\text{-NiSe}_2\text{-CoSe}_2$ toward HER. (f) LSV curves of $\text{Mo}_{0.5}\text{-NiSe}_2\text{-CoSe}_2$ toward HER before and after 2000 CV cycles. (g–i) Chronoamperometric measurement of $\text{Mo}_{0.5}\text{-NiSe}_2\text{-CoSe}_2$ toward HER with different initial current densities (10, 100 and 200 $\text{mA}\cdot\text{cm}^{-2}$). All the LSV tests were repeated 6 times, and all the EIS measurements were repeated 3 times for the error estimates.

the three curves, which represented the reconstitution process and the construction of OOH^* . Furthermore, the OER reaction started at around 1.42 V for all the $\text{Mo}_x\text{-NiSe}_2\text{-CoSe}_2$ aerogels, affording the corresponding overpotentials of 227, 206, 193 mV at 10 $\text{mA}\cdot\text{cm}^{-2}$, 342, 308, 270 mV at 100 $\text{mA}\cdot\text{cm}^{-2}$, and 401, 364, 329 mV at 200 $\text{mA}\cdot\text{cm}^{-2}$ for the $\text{Mo}_{0.3}\text{-NiSe}_2\text{-CoSe}_2$, $\text{Mo}_{0.5}\text{-NiSe}_2\text{-CoSe}_2$, and $\text{Mo}_{0.7}\text{-NiSe}_2\text{-CoSe}_2$, respectively, where the $\text{Mo}_{0.7}\text{-NiSe}_2\text{-CoSe}_2$ demonstrated the best OER performance with the optimal Mo content. Noteworthy, all the $\text{Mo}_x\text{-NiSe}_2\text{-CoSe}_2$ aerogels exhibited better performance than that of RuO_2 (260 mV@10 $\text{mA}\cdot\text{cm}^{-2}$, 386 mV@100 $\text{mA}\cdot\text{cm}^{-2}$ and 469 mV@200 $\text{mA}\cdot\text{cm}^{-2}$), proving that the Mo-doped TMSes-based electrocatalysts showed superior activity than noble metal-based materials in OER [9]. In contrast with the optimal $\text{Mo}_{0.7}\text{-NiSe}_2\text{-CoSe}_2$, the $\text{NiSe}_2\text{-CoSe}_2$ aerogel without Mo doping presented higher reconstruction voltage of 1.20 V and larger overpotentials of 215, 352, and 409 mV at 10, 100 and 200 $\text{mA}\cdot\text{cm}^{-2}$ (Fig. S5(a)), demonstrating that Mo doping enhanced the adsorption of OH^- and promoted the onset of OER under a lower voltage [28]. Benefited from the advantages, the $\text{Mo}_{0.7}\text{-NiSe}_2\text{-CoSe}_2$ put up more splendid performance than recently reported materials (Fig. 5(c)) [7,20–23,26,43,45,46]. Moreover, the $\text{Mo}_{0.7}\text{-NiSe}_2\text{-CoSe}_2$ showed a small Tafel slope value of 199 $\text{mV}\cdot\text{dec}^{-1}$ at high current density, lower than that of $\text{NiSe}_2\text{-CoSe}_2$ (235 $\text{mV}\cdot\text{dec}^{-1}$, Fig. S5(b)), $\text{Mo}_{0.3}\text{-NiSe}_2\text{-CoSe}_2$

(235 $\text{mV}\cdot\text{dec}^{-1}$), $\text{Mo}_{0.5}\text{-NiSe}_2\text{-CoSe}_2$ (225 $\text{mV}\cdot\text{dec}^{-1}$), and RuO_2 (272 $\text{mV}\cdot\text{dec}^{-1}$, Fig. 5(d)), further indicating the faster kinetics toward OER. Significantly, different from the corresponding results in HER, the $\text{Mo}_{0.7}\text{-NiSe}_2\text{-CoSe}_2$ presented a calculated R_{ct} of 23.66 X under the voltage of OER, which was slightly higher than that of $\text{Mo}_{0.5}\text{-NiSe}_2\text{-CoSe}_2$ (10.28 X) and greatly lower than that of $\text{Mo}_{0.3}\text{-NiSe}_2\text{-CoSe}_2$ (60.31 X, Fig. 5(e)). Except for the promoted electron transfer caused by Mo doping, the amorphous phase on the surface of $\text{Mo}_{0.7}\text{-NiSe}_2\text{-CoSe}_2$ showed the tendency to lose electrons in anodic reaction, leading to the reduction of electrochemical impedance. Same as the HER process, the cyclic stability toward OER was measured by the LSV tests that before and after 2000 CV cycles as well (Fig. 5(f)). The oxidation peak at 1.10–1.40 V was disappeared after CV cycles, indicating that the reconstitution was completed on the surface of $\text{Mo}_{0.7}\text{-NiSe}_2\text{-CoSe}_2$ electrode. Besides, the current density at 1.40–1.65 V exhibited tiny attenuation after 2000 CV cycles, illustrating the favorable cyclic stability of $\text{Mo}_{0.7}\text{-NiSe}_2\text{-CoSe}_2$ toward OER. Additionally, the electrocatalytic stability of $\text{Mo}_{0.7}\text{-NiSe}_2\text{-CoSe}_2$ aerogel with the best OER performance was tested by chronoamperometry under the voltages to achieve different initial current densities of 10 $\text{mA}\cdot\text{cm}^{-2}$, 100 $\text{mA}\cdot\text{cm}^{-2}$, and 200 $\text{mA}\cdot\text{cm}^{-2}$ (Fig. 5(g)–(i)). As the operation voltage was high, the accumulation and release of oxygen bubbles on electrodes resulted in the undulation of current density, so that the curves

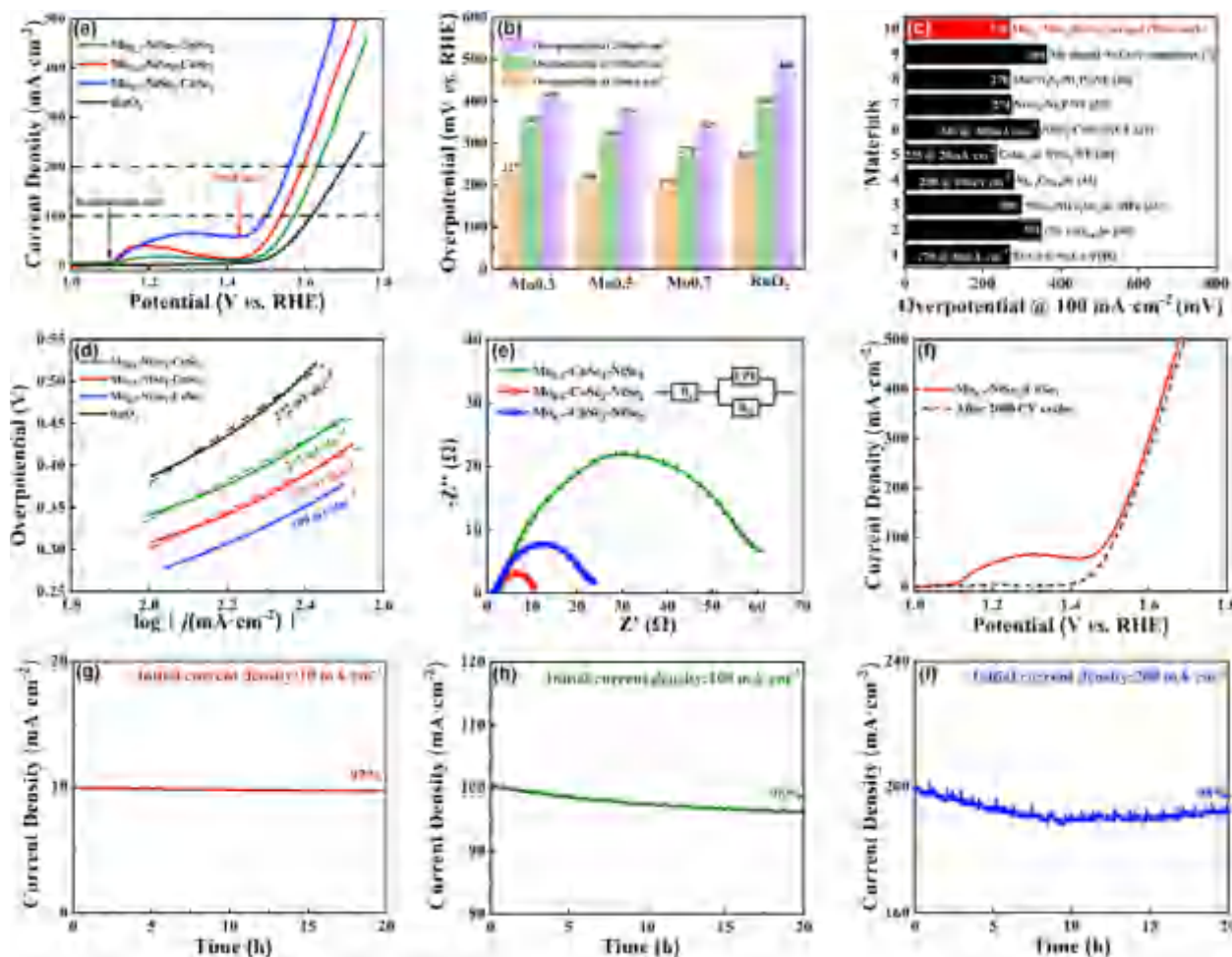


Fig. 5. (a) Polarization LSV curves of $\text{Mo}_x\text{-NiSe}_2\text{-CoSe}_2$ aerogels and RuO_2 toward OER in 1.0 M KOH. (b) The overpotentials of obtained samples at different current densities. (c) Performance comparison of the optimized $\text{Mo}_{0.7}\text{-NiSe}_2\text{-CoSe}_2$ aerogel and published references. (d) Tafel slopes of $\text{Mo}_x\text{-NiSe}_2\text{-CoSe}_2$ aerogels and RuO_2 toward OER in 1.0 M KOH. (e) Nyquist plot of $\text{Mo}_x\text{-NiSe}_2\text{-CoSe}_2$ toward OER. (f) LSV curves of $\text{Mo}_{0.7}\text{-NiSe}_2\text{-CoSe}_2$ toward OER before and after 2000 CV cycles. (g–i) Chronoamperometric measurement of $\text{Mo}_{0.7}\text{-NiSe}_2\text{-CoSe}_2$ toward HER with different initial current densities (10, 100 and 200 mA cm^{-2}). All the LSV tests were repeated 6 times, and all the EIS measurements were repeated 3 times for the error estimates.

at high current densities (100 mA cm^{-2} and 200 mA cm^{-2}) exhibited fluctuations [47,48]. After 20 h, the current densities retained more than 95% of the initial value for all the three tests, illustrating the favorable stability of $\text{Mo}_{0.7}\text{-NiSe}_2\text{-CoSe}_2$ toward OER.

Furthermore, the CV curves of obtained samples in the non-Faradaic potential region were presented in Figure S6, where the capacitive currents density at 0.525 V (vs. RHE) linearly increase with the scan rate for all the catalysts. Based on the slope, the double layer capacitance (C_{dl}) of $\text{NiSe}_2\text{-CoSe}_2$, $\text{Mo}_{0.3}\text{-NiSe}_2\text{-CoSe}_2$, $\text{Mo}_{0.5}\text{-NiSe}_2\text{-CoSe}_2$, and $\text{Mo}_{0.7}\text{-NiSe}_2\text{-CoSe}_2$ were fitted as 18.50, 11.63, 9.42, and 12.10 mF cm^{-2} , respectively (Fig. 6(a)). Based on the results, the electrochemical surface area (ECSA) of the four sample were calculated by Eq. (13) [29,49,50]:

$$\text{ECSA} = C_{dl} / C_s \quad (C_s = 0.04 \text{ mF cm}^{-2}) \quad (13)$$

As it shown in Fig. 6(b), the ECSA of $\text{NiSe}_2\text{-CoSe}_2$, $\text{Mo}_{0.3}\text{-NiSe}_2\text{-CoSe}_2$, $\text{Mo}_{0.5}\text{-NiSe}_2\text{-CoSe}_2$, and $\text{Mo}_{0.7}\text{-NiSe}_2\text{-CoSe}_2$ were 462.50, 290.75, 235.50, and 302.50 cm^2 , respectively. As mentioned earlier, the introduction of Mo led to the size reduction of hydrogen bubble templates, so that all the $\text{Mo}_x\text{-NiSe}_2\text{-CoSe}_2$ exhibited smaller ECSA than the control samples without Mo doping. However, the $\text{Mo}_{0.7}\text{-NiSe}_2\text{-CoSe}_2$ showed a higher ECSA than the other two Mo doped aerogels, indicating that the fluffy

structure on the surface provided extra electron transmission region. Furthermore, the LSV curves were normalized by the calculated ECSA, where the $\text{Mo}_{0.5}\text{-NiSe}_2\text{-CoSe}_2$ and $\text{Mo}_{0.7}\text{-NiSe}_2\text{-CoSe}_2$ exhibited the highest intrinsic activities in HER (Figure S7) and OER (Figure S8), respectively. Therefore, the enhancement of water molecules nucleophilic adsorption and charge transfer efficiency caused by Mo doping significantly increased the intrinsic performance of the optimized samples, which was sufficient to compensate for the negative influence on the ECSA of aerogel morphology [35]. On the basis of good activities of HER and OER, an overall water splitting cell was assembled with $\text{Mo}_{0.5}\text{-NiSe}_2\text{-CoSe}_2$ as cathodic catalyst and $\text{Mo}_{0.7}\text{-NiSe}_2\text{-CoSe}_2$ as anodic catalyst electrodes in 1 M KOH solution (Fig. 6(c)). The $\text{Mo}_x\text{-NiSe}_2\text{-CoSe}_2$ aerogels system exhibited a low potential of 1.54 V at 10 mA cm^{-2} , which was lower than that of Pt/C// RuO_2 (1.56 V at 10 mA cm^{-2}). Moreover, a ratio of $\text{H}_2\text{:O}_2$ close to 2:1 (Figure S9) indicated the nearly 100% faradaic efficiency (FE) for each gas evolution reaction[21]. Besides, after 2000 CV cycles, the current density of the $\text{Mo}_x\text{-NiSe}_2\text{-CoSe}_2$ two-electrode system presented slight attenuation under high cell voltage of 1.70–1.90 V (Figure S10). However, as to the overall view, the $\text{Mo}_x\text{-NiSe}_2\text{-CoSe}_2$ could maintain good cyclic stability in the overall water splitting process. In addition to catalytic activity, the stability of the overall water splitting cell was also

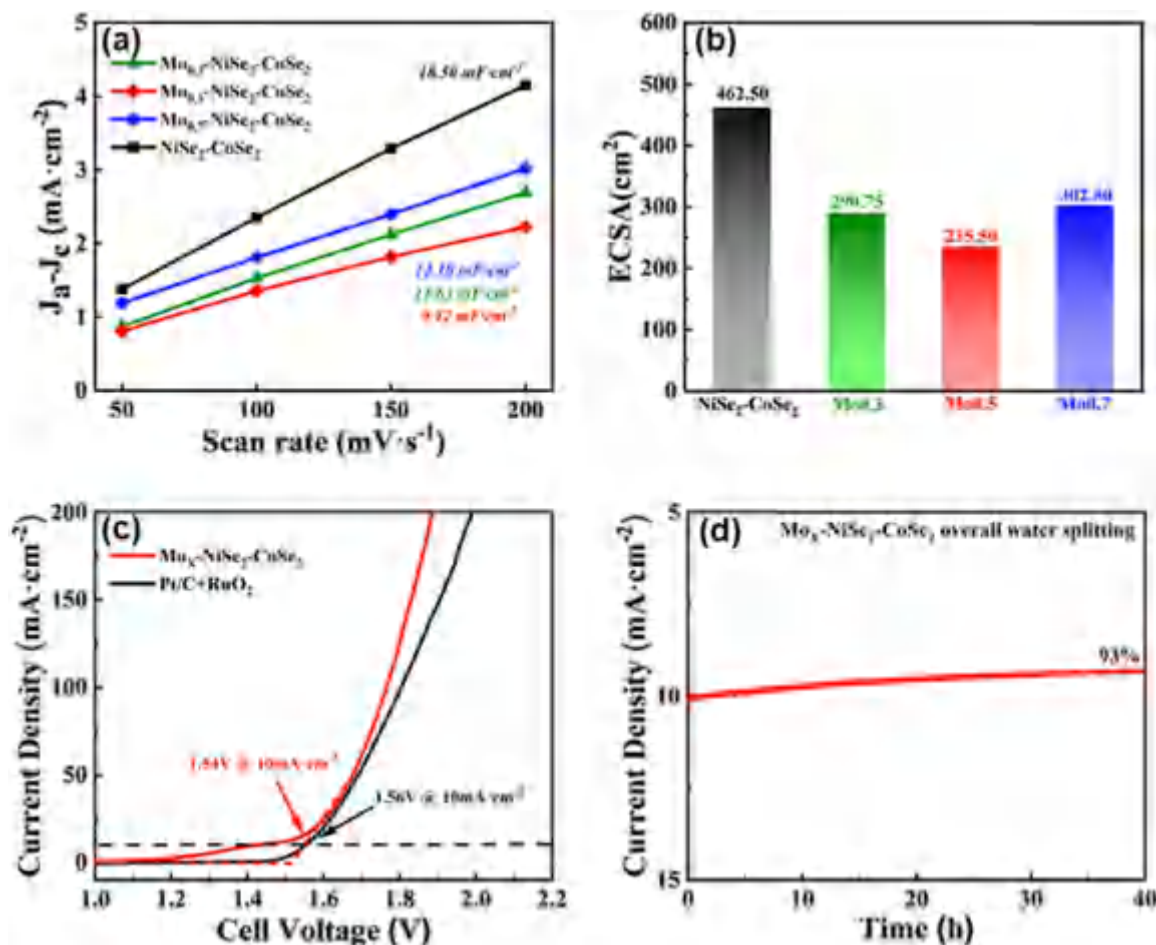


Fig. 6. (a) The C_{dl} values of the NiSe₂-CoSe₂ and Mo_X-NiSe₂-CoSe₂ samples. (b) ECSA of the NiSe₂-CoSe₂ and Mo_X-NiSe₂-CoSe₂ samples. (c) Polarization LSV curves of the dual electrodes system formed by Mo_X-NiSe₂-CoSe₂ aerogels (Mo_{0.5}-NiSe₂-CoSe₂ for cathode and Mo_{0.7}-NiSe₂-CoSe₂ for anode) and contrast noble-metal system (Pt/C for cathode and RuO₂ for anode) toward overall water splitting in 1.0 M KOH. (d) Chronoamperometric measurement of Mo_X-NiSe₂-CoSe₂ toward overall water splitting with the initial current densities of 10 mA cm⁻². All the LSV tests were repeated 6 times, and all the tests to get the C_{dl} were repeated 3 times for the error estimates.

investigated. Fig. 6(d) showed that the Mo_X-NiSe₂-CoSe₂ device showed decent durability, with a current retention of 93% after 40 h operation. Therefore, the Mo_X-NiSe₂-CoSe₂ aerogel served as a favorable electrocatalyst for both HER and OER in water-splitting process with the requirements of high activities and decent stabilities.

3.4. Theoretical calculation analysis

To further understand the origin of the observed excellent performance of both HER and OER on Mo_X-NiSe₂-CoSe₂ aerogels, theoretical calculations were conducted using density functional theory (DFT) with the Materials Studio-DMol³. Based on the SEM, TEM images, and XRD results, we constructed the models of NiSe₂-CoSe₂ and Mo-NiSe₂-CoSe₂ structures to match the samples of NiSe₂-CoSe₂ and Mo_X-NiSe₂-CoSe₂ (Fig. 7(a)). To be specific, we calculated adsorption energy of H₂O molecule (DE_{H_2O}) on the surface of the established systems (Fig. 7(b)). The Mo-NiSe₂-CoSe₂ structure exhibited a higher DE_{H_2O} of 1.45 eV than that of NiSe₂-CoSe₂ (0.84 eV), indicating a stronger binding strength and better adsorption property toward H₂O molecule provided by Mo doping. In addition, the contact angles of 1 M KOH solution on the surface of obtained samples decreased with the improving of Mo content, which further proved the positive effect of Mo doping toward water adsorption (Fig. 7(c))[35]. Moreover, the free energy of hydrogen adsorption (DG_{H^*}) for NiSe₂-CoSe₂ and Mo-NiSe₂-CoSe₂

were calculated to evaluate the potential HER performance (Fig. 7(d)). For the NiSe₂-CoSe₂ structure, the Ni site exhibited stronger DG_{H^*} (-0.26 eV) than that of Co site (-0.18 eV), indicating that the Co site possessed better adsorption property and high activity toward HER[21,51]. After introducing the high-electropositive Mo element, the DG_{H^*} of Ni and Co sites were translated to -0.20 and -0.12 eV, respectively, demonstrating that the doping Mo adsorbed electrons from Ni and Co and enhanced the desorption of H⁺ on those sites. It was illustrated that Mo doping could reduce the excessive adsorption properties toward H⁺ on the Ni and Co sites in the NiSe₂-CoSe₂ structure, leading to the generation of active sites with DG_{H^*} that closer to ideal state (0 eV). Furthermore, we proposed a detailed OER mechanism of the two structures by calculating the free energy of reaction intermediates (Fig. 7(e)). The high-electropositive Mo site afforded stronger OH⁻ adsorption in Mo-NiSe₂-CoSe₂ (-1.63 eV) than that of Co site in NiSe₂-CoSe₂ (-1.25 eV) and in Mo-NiSe₂-CoSe₂ (-1.17 eV), indicating a stronger trend of reconstitution and activation on the Mo site during the anodic reaction process[52]. Besides, the electron transfer step to form *OOH exhibited a larger ladder span for the two samples, which was the rate-limiting step for OER process[21]. Apparently, the energy barrier of the Mo site in Mo-NiSe₂-CoSe₂ was 1.51 eV, which was lower than that of the Co site in NiSe₂-CoSe₂ (1.86 eV) and in Mo-NiSe₂-CoSe₂ (1.80 eV), proving that the Mo site had the optimal property toward electrocatalytic OER with smaller overpotential. Based on above results of theoretical

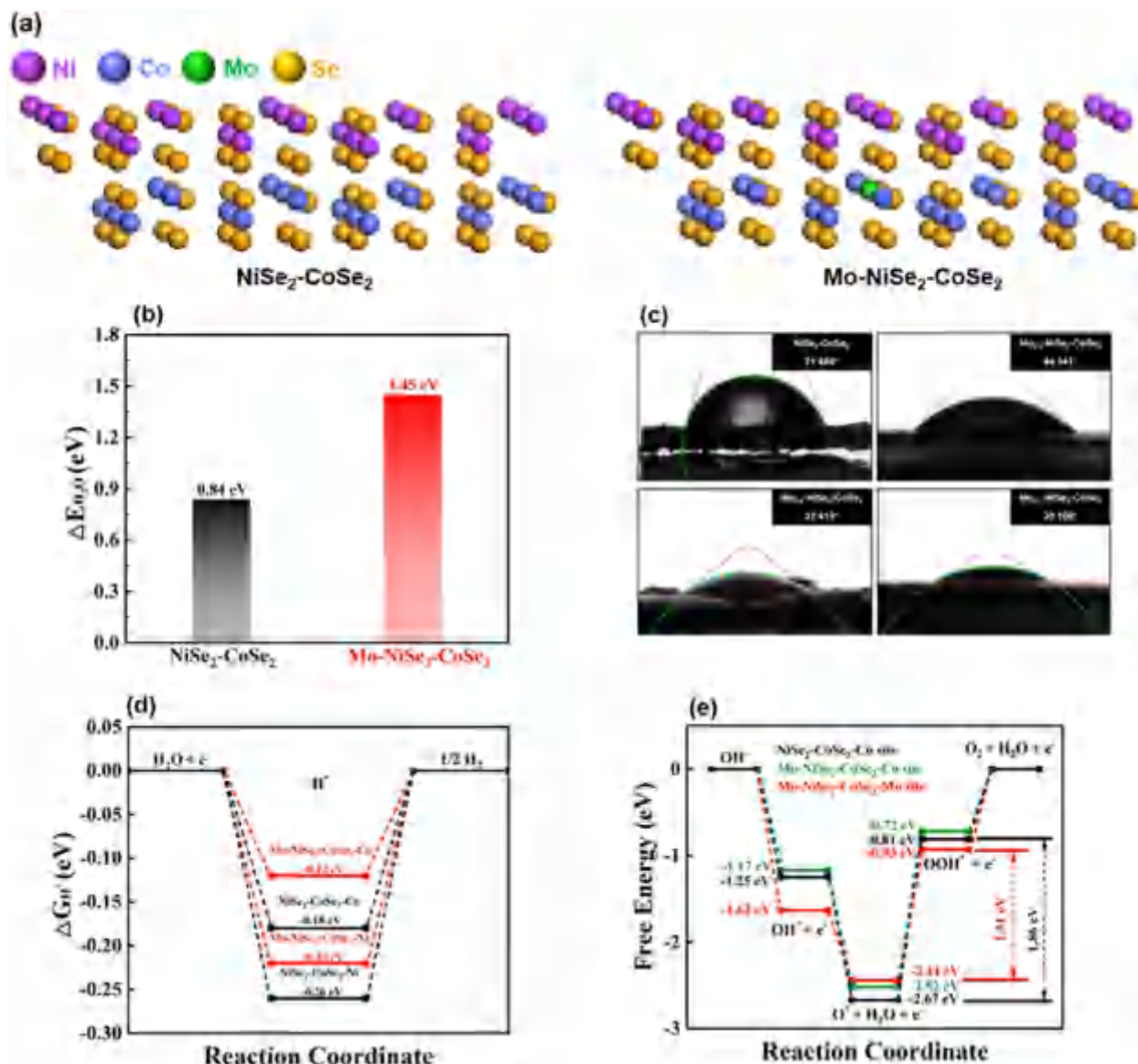


Fig. 7. (a) Crystal models of NiSe₂-CoSe₂ and Mo-NiSe₂-CoSe₂. (b) H₂O adsorption energy on the surface of NiSe₂-CoSe₂ and Mo-NiSe₂-CoSe₂. (c) Contact angles of NiSe₂-CoSe₂ and MoX-NiSe₂-CoSe₂ with increasing Mo content. (d) Free energy diagram of HER. (e) Free energy diagram of OER. All the tests to get the contact angles were repeated 6 times for the error estimates.

calculation, the high-electropositive Mo element not only adjusted the adsorption properties of NiSe₂-CoSe₂ heterostructure toward OH⁻, but also acted as suitable active sites for electro catalyzing OER in anode. Therefore, the Mo_{0.7}-NiSe₂-CoSe₂ with higher Mo content demonstrated better OER activity than that of Mo_{0.5}-NiSe₂-CoSe₂.

4. Conclusion

In summary, we designed and synthesized a series of novel Mo doped NiSe₂-CoSe₂ aerogels via facile spontaneous gelation and selenium vapor deposition process. The Mo_{0.5}-NiSe₂-CoSe₂ aerogel showed splendid hydrogen evolution reaction (HER) activity with low potential (57 mV at 10 mA·cm⁻²) and favorable stabilities, which benefited from the enhanced nucleophilic adsorption of water molecule and higher charge transfer efficiency provided by adjusted Mo doping. Meanwhile, the doping Mo with high electropositivity acted as the active site in (oxygen evolution reaction) OER process, which provided the Mo_{0.7}-NiSe₂-CoSe₂ aerogel won-

derful performance (270 mV at 100 mA·cm⁻²). Compared with published literatures of Mo doping electrocatalysts [7,26–28], we deeply illustrated the different effects of doped Mo toward the active sites of HER and OER process. In addition, our work combined Mo-doped heterostructures with aerogel morphology for the first time, which enabled the samples to possess abundant of active sites and mass transfer pathways with higher intrinsic activity than that of reported alloy-based aerogels [33,53]. Our work afforded a new and facile approach to construct and optimize TMSes-based electrocatalysts, and we were committed to extend the application of this method to a wide range of active substances for efficient overall water splitting in the future.

CRediT authorship contribution statement

Hongchen Liu: Writing – review & editing, Writing – original draft, Formal analysis, Investigation, Conceptualization. Fan Yang: Writing – review & editing, Writing – original draft, Formal analysis. Fengjiang Chen: Investigation, Writing – review & editing. Sai

Che: Investigation, Formal analysis, Writing – review & editing.
 Neng Chen: Investigation. Siyuan Sun: Investigation, Writing – review & editing.
 Na Ta: Investigation. Yang Sun: Investigation.
 Ni Wu: . Yankun Sun: Writing – review & editing. Yongfeng Li: Writing – review & editing, Writing – original draft, Supervision.

Data availability

The data that has been used is confidential.

Declaration of Competing Interest

The authors declare that they have no known competing financial interests or personal relationships that could have appeared to influence the work reported in this paper.

Acknowledgements

We gratefully thank for the National Natural Science Foundation of China (Nos.22278431, Nos.21776302).

Appendix A. Supplementary material

Supplementary data to this article can be found online at <https://doi.org/10.1016/j.jcis.2023.02.154>.

References

- [1] B. You, Y. Sun, Innovative strategies for electrocatalytic water splitting, *Acc. Chem. Res.* 51 (2018) 1571–1580, <https://doi.org/10.1021/acs.accounts.8b00002>.
- [2] I. Roger, M.A. Shipman, M.D. Symes, Earth-abundant catalysts for electrochemical and photoelectrochemical water splitting, *Nat. Rev. Chem.* 1 (2017), <https://doi.org/10.1038/s41570-016-0003>.
- [3] A. Wang, L. Cheng, W. Zhao, X. Shen, W. Zhu, Electrochemical hydrogen and oxygen evolution reactions from a cobalt-porphyrin-based covalent organic polymer, *J. Colloid Interface Sci.* 579 (2020) 598–606, <https://doi.org/10.1016/j.jcis.2020.06.109>.
- [4] J. Zhang, Q. Zhang, X. Feng, Support and Interface Effects in Water-Splitting Electrocatalysts, *Adv. Mater.* 31 (2019) 1–19, <https://doi.org/10.1002/adma.201808167>.
- [5] L. Li, P. Wang, Q. Shao, X. Huang, Metallic nanostructures with low dimensionality for electrochemical water splitting, *Chem. Soc. Rev.* 49 (2020) 3072–3106, <https://doi.org/10.1039/d0cs00013b>.
- [6] H. Sun, Z. Yan, F. Liu, W. Xu, F. Cheng, J. Chen, Self-Supported Transition-Metal-Based Electrocatalysts for Hydrogen and Oxygen Evolution, *Adv. Mater.* 32 (2020) 1–18, <https://doi.org/10.1002/adma.201806326>.
- [7] J. Lin, Y. Yan, C. Li, X. Si, H. Wang, J. Qi, Bifunctional Electrocatalysts Based on Mo - Doped NiCoP Nanosheet Arrays for Overall Water Splitting, *Nano-Micro Lett.* 11 (2019) 1–11, <https://doi.org/10.1007/s40820-019-0289-6>.
- [8] V.H. Hoa, D.T. Tran, D.C. Nguyen, D.H. Kim, N.H. Kim, J.H. Lee, Molybdenum and Phosphorous Dual Doping in Cobalt Monolayer Interfacial Assembled Cobalt Nanowires for Efficient Overall Water Splitting, *Adv. Funct. Mater.* 30 (2020) 1–12, <https://doi.org/10.1002/adfm.202002533>.
- [9] X. Peng, Y. Yan, X. Jin, C. Huang, W. Jin, B. Gao, P.K. Chu, Recent advance and perspectives of electrocatalysts based on transition metal selenides for efficient water splitting, *Nano Energy*. 78 (2020), <https://doi.org/10.1016/j.nanoen.2020.105234>.
- [10] K. Xu, H. Ding, H. Lv, S. Tao, P. Chen, X. Wu, W. Chu, C. Wu, Y. Xie, Understanding Structure-Dependent Catalytic Performance of Nickel Selenides for Electrochemical Water Oxidation, *ACS Catal.* 7 (2017) 310–315, <https://doi.org/10.1021/acscatal.6b02884>.
- [11] X. Zheng, X. Han, H. Liu, J. Chen, D. Fu, J. Wang, C. Zhong, Y. Deng, W. Hu, Controllable Synthesis of Ni_xSe (0.5 ≤ x ≤ 1) Nanocrystals for Efficient Rechargeable Zinc-Air Batteries and Water Splitting, *ACS Appl. Mater. Interfaces*. 10 (2018) 13675–13684, <https://doi.org/10.1021/acsami.8b01651>.
- [12] K. Lan, J. Li, Y. Zhu, L. Gong, F. Li, P. Jiang, F. Niu, R. Li, Morphology engineering of CoSe₂ as efficient electrocatalyst for water splitting, *J. Colloid Interface Sci.* 539 (2019) 646–653, <https://doi.org/10.1016/j.jcis.2018.12.044>.
- [13] Y. Shi, B. Zhang, Recent advances in transition metal phosphide nanomaterials: Synthesis and applications in hydrogen evolution reaction, *Chem. Soc. Rev.* 45 (2016) 1529–1541, <https://doi.org/10.1039/c5cs00434a>.
- [14] S. Sanati, A. Morsali, H. Garcia, First-row transition metal-based materials derived from bimetallic metal-organic frameworks as highly efficient electrocatalysts for electrochemical water splitting, *Energy Environ. Sci.* 15 (2022) 3119–3151, <https://doi.org/10.1039/d1ee03614a>.
- [15] B. Wang, C. Tang, H.F. Wang, X. Chen, R. Cao, Q. Zhang, A Nanosized CoNi Hydroxide@Hydroxysulfide Core-Shell Heterostructure for Enhanced Oxygen Evolution, *Adv. Mater.* 31 (2019) 1–7, <https://doi.org/10.1002/adma.201805658>.
- [16] Y. Li, W. Wang, B. Huang, Z. Mao, R. Wang, B. He, Y. Gong, H. Wang, Abundant heterointerfaces in MOF-derived hollow CoS₂–MoS₂ nanosheet array electrocatalysts for overall water splitting, *J. Energy Chem.* 57 (2021) 99–108, <https://doi.org/10.1016/j.jechem.2020.08.064>.
- [17] H. Li, S. Yang, W. Wei, M. Zhang, Z. Jiang, Z. Yan, J. Xie, Chrysanthemum-like FeS/Ni₃S₂ heterostructure nanoarray as a robust bifunctional electrocatalyst for overall water splitting, *J. Colloid Interface Sci.* 608 (2022) 536–548, <https://doi.org/10.1016/j.jcis.2021.09.121>.
- [18] Z. Huang, L. He, W. Zhang, W. Huang, Q. Mo, L. Yang, Q. Fu, Q. Gao, Nickel sulfide-oxide heterostructured electrocatalysts: Bi-functionality for overall water splitting and in-situ reconstruction, *J. Colloid Interface Sci.* 622 (2022) 728–737, <https://doi.org/10.1016/j.jcis.2022.04.150>.
- [19] C. Liu, T. Gong, J. Zhang, X. Zheng, J. Mao, H. Liu, Y. Li, Q. Hao, Engineering Ni₂P–NiSe₂ heterostructure interface for highly efficient alkaline hydrogen evolution, *Appl. Catal. B Environ.* 262 (2020) 1–8, <https://doi.org/10.1016/j.apcatb.2019.118245>.
- [20] X. Zhang, Y. Ding, G. Wu, X. Du, CoSe₂@NiSe₂ nanoarray as better and efficient electrocatalyst for overall water splitting, *Int. J. Hydrogen Energy*. 45 (2020) 30611–30621, <https://doi.org/10.1016/j.ijhydene.2020.08.096>.
- [21] D. Chen, Z. Xu, W. Chen, G. Chen, J. Huang, J. Huang, C. Song, C. Li, K. (Ken) Ostrikov, Just add water to split water: ultrahigh-performance bifunctional electrocatalysts fabricated using eco-friendly heterointerfacing of NiCo diselenides, *J. Mater. Chem. A*. 8 (2020) 12035–12044, <https://doi.org/10.1039/d0ta02121k>.
- [22] P. Wang, Z. Pu, W. Li, J. Zhu, C. Zhang, Y. Zhao, S. Mu, Coupling NiSe₂–Ni₂P heterostructure nanowrinkles for highly efficient overall water splitting, *377* (2019) 600–608, <https://doi.org/10.1016/j.jcat.2019.08.005>.
- [23] J. Yuan, X. Cheng, H. Wang, C. Lei, S. Pardiwala, B. Yang, Z. Li, Q. Zhang, L. Lei, S. Wang, Y. Hou, A Superaerophobic Bimetallic Selenides Heterostructure for Efficient Industrial-Level Oxygen Evolution at Ultra-High Current Densities, *Nano-Micro Lett.* 12 (2020) 1–12, <https://doi.org/10.1007/s40820-020-00442-0>.
- [24] M. Velpandian, G. Ummethala, S.K. Malladi, P. Meduri, Heterostructures of tin and tungsten selenides for robust overall water splitting, *J. Colloid Interface Sci.* 623 (2022) 561–573, <https://doi.org/10.1016/j.jcis.2022.05.052>.
- [25] X. Liu, W. Zhang, M. Peng, G. Zhai, L. Hu, L. Mao, The role of S and Mo doping on the dissociation of water molecule on FeOCl surface: Experimental and theoretical analysis, *Chem. Eng. J.* 426 (2021), <https://doi.org/10.1016/j.cej.2021.131353>.
- [26] X. Luo, P. Ji, P. Wang, R. Cheng, D. Chen, C. Lin, J. Zhang, J. He, Z. Shi, N. Li, S. Xiao, S. Mu, Interface Engineering of Hierarchical Branched Mo-Doped Ni₃Se₂/Ni₂Py Hollow Heterostructure Nanorods for Efficient Overall Water Splitting, *Adv. Energy Mater.* 10 (2020) 1–11, <https://doi.org/10.1002/aenm.201903891>.
- [27] Y. Zhou, J. Zhang, H. Ren, Y. Pan, Y. Fan, F. Sun, X. Wang, S. Wang, J. Zhang, Mo doping induced metallic CoSe for enhanced electrocatalytic hydrogen evolution, *Appl. Catal. B Environ.* 268 (2020), <https://doi.org/10.1016/j.apcatb.2019.118467>.
- [28] J. Huang, S. Wang, J. Nie, C. Huang, X. Zhang, B. Wang, J. Tang, C. Du, Z. Liu, J. Chen, Active site and intermediate modulation of 3D CoSe₂ nanosheet array on Ni foam by Mo doping for high-efficiency overall water splitting in alkaline media, *Chem. Eng. J.* 417 (2021), <https://doi.org/10.1016/j.cej.2020.128055>.
- [29] B. Zhang, F. Yang, X. Liu, N. Wu, S. Che, Y. Li, Phosphorus doped nickel-molybdenum aerogel for efficient overall water splitting, *Appl. Catal. B Environ.* 298 (2021), <https://doi.org/10.1016/j.apcatb.2021.120494>.
- [30] F. Chen, F. Yang, H. Liu, S. Che, G. Zhang, C. Xu, Y. Li, One-pot preparation of surface vulcanization Co-Fe bimetallic aerogel for efficient sulfadiazine degradation, *Chem. Eng. J.* 430 (2022), <https://doi.org/10.1016/j.cej.2021.132904>.
- [31] H. Liu, F. Yang, Z. Xu, X. Yan, F. Chen, C. Xu, S. Che, Y. Li, P-doped CoCu aerogel as a bifunctional electrocatalyst for efficient overall water splitting, *Electrochim. Acta*. 430 (2022), <https://doi.org/10.1016/j.electacta.2022.141075>.
- [32] L. Liu, L.X. Chen, A.J. Wang, J. Yuan, L. Shen, J.J. Feng, Hydrogen bubbles template-directed synthesis of self-supported AuPt nanowire networks for improved ethanol oxidation and oxygen reduction reactions, *Int. J. Hydrogen Energy*. 41 (2016) 8871–8880, <https://doi.org/10.1016/j.ijhydene.2016.03.208>.
- [33] A.A. Dubale, Y. Zheng, H. Wang, R. Hübner, Y. Li, J. Yang, J. Zhang, N.K. Sethi, L. He, Z. Zheng, W. Liu, High-Performance Bismuth-Doped Nickel Aerogel Electrocatalyst for the Methanol Oxidation Reaction, *Angew. Chemie - Int. Ed.* 59 (2020) 13891–13899, <https://doi.org/10.1002/anie.202004314>.
- [34] C. Zhu, Q. Shi, S. Fu, J. Song, H. Xia, D. Yu, Y. Lin, Efficient Synthesis of MCu (M = Pd, Pt, and Au), in: Aerogels with Accelerated Gelation Kinetics and Their High Electrocatalytic Activity, 2016, pp. 1–5, <https://doi.org/10.1002/adma.201602546>.
- [35] J. Lin, Y. Yan, C. Li, X. Si, H. Wang, J. Qi, J. Cao, Z. Zhong, W. Fei, J. Feng, Bifunctional Electrocatalysts Based on Mo-Doped NiCoP Nanosheet Arrays for Overall Water Splitting, *Nano-Micro Lett.* 11 (2019) 1–11, <https://doi.org/10.1007/s40820-019-0289-6>.
- [36] X. Yu, Q. Lv, L. She, L. Hou, Y. Fautrelle, Z. Ren, G. Cao, X. Lu, X. Li, Controlled moderate sulfidation-fabricated hierarchical heterogeneous nickel sulfides-based electrocatalyst with tripartite Mo doping for efficient oxygen evolution, *J. Energy Chem.* 68 (2022) 780–788, <https://doi.org/10.1016/j.jechem.2021.12.010>.

- [37] B. Cai, A. Eychmüller, Promoting Electrocatalysis upon Aerogels, *Adv. Mater.* 31 (2019) 1–16, <https://doi.org/10.1002/adma.201804881>.
- [38] N. Chen, W. Zhang, J. Zeng, L. He, D. Li, Q. Gao, Plasma-Engineered MoP with nitrogen doping: Electron localization toward efficient alkaline hydrogen evolution, *Appl. Catal. B Environ.* 268 (2020), <https://doi.org/10.1016/j.apcatb.2019.118441> 118441.
- [39] X. Yun, T. Lu, R. Zhou, Z. Lu, J. Li, Y. Zhu, Heterostructured NiSe 2 / CoSe 2 hollow microspheres as battery-type cathode for hybrid supercapacitors : Electrochemical kinetics and energy storage mechanism, *Chem. Eng. J.* 426 (2021), <https://doi.org/10.1016/j.cej.2021.131328> 131328.
- [40] X.D. Wang, H.Y. Chen, Y.F. Xu, J.F. Liao, B.X. Chen, H.S. Rao, D. Bin Kuang, C.Y. Su, Self-supported NiMoP2 nanowires on carbon cloth as an efficient and durable electrocatalyst for overall water splitting, *J. Mater. Chem. A* 5 (2017) 7191–7199, <https://doi.org/10.1039/c6ta11188b>.
- [41] S.M.N. Jeghan, D. Kim, Y. Lee, M. Kim, G. Lee, Designing a smart heterojunction coupling of cobalt-iron layered double hydroxide on nickel selenide nanosheets for highly efficient overall water splitting kinetics, *Appl. Catal. B Environ.* 308 (2022), <https://doi.org/10.1016/j.apcatb.2022.121221> 121221.
- [42] Y. Zhang, Q. Shao, S. Long, X. Huang, Cobalt-molybdenum nanosheet arrays as highly efficient and stable earth-abundant electrocatalysts for overall water splitting, *Nano Energy* 45 (2018) 448–455, <https://doi.org/10.1016/j.nanoen.2018.01.022>.
- [43] Z. Qian, Y. Chen, Z. Tang, Z. Liu, X. Wang, Hollow Nanocages of Ni x Co 1–x Se for Efficient Zinc – Air Batteries and Overall Water Splitting, *Nano-Micro Lett.* 11 (28) (2019) 1–17, <https://doi.org/10.1007/s40820-019-0258-0>.
- [44] J. Zhu, L. Hu, P. Zhao, L.Y.S. Lee, K.Y. Wong, Recent Advances in Electrocatalytic Hydrogen Evolution Using Nanoparticles, *Chem. Rev.* 120 (2020) 851–918, <https://doi.org/10.1021/acs.chemrev.9b00248>.
- [45] K. Xiao, L. Zhou, M. Shao, M. Wei, Fabrication of (Ni, Co)0.85Se nanosheet arrays derived from layered double hydroxides toward largely enhanced overall water splitting, *J. Mater. Chem. A* 6 (2018) 7585–7591, <https://doi.org/10.1039/c8ta01067f>.
- [46] Y. Gong, Z. Xu, H. Pan, Y. Lin, J. Wang, A 3D well-matched electrode pair of Ni – Co – S // Ni – Co – P nanoarrays grown on nickel foam as a high- performance electrocatalyst for water splitting †, (2018) 12506–12514, 10.1039/c8ta03163k.
- [47] A.K. Taylor, T. Mou, A. Sonea, J. Chen, B.B. Yee, B.D. Gates, Arrays of Microscale Linear Ridges with Self-Cleaning Functionality for the Oxygen Evolution Reaction, *ACS Appl. Mater. Interfaces* 13 (2021) 2399–2413, <https://doi.org/10.1021/acsami.0c15240>.
- [48] H. Vogt, R.J. Balzer, The bubble coverage of gas-evolving electrodes in stagnant electrolytes, *Electrochim. Acta* 50 (2005) 2073–2079, <https://doi.org/10.1016/j.electacta.2004.09.025>.
- [49] Y. Yang, W. Zhang, Y. Xiao, Z. Shi, X. Cao, Y. Tang, Q. Gao, CoNiSe2 heteronanorods decorated with layered-double-hydroxides for efficient hydrogen evolution, *Appl. Catal. B Environ.* 242 (2019) 132–139, <https://doi.org/10.1016/j.apcatb.2018.09.082>.
- [50] D. Guo, J. Qi, W. Zhang, R. Cao, Surface Electrochemical Modification of a Nickel Substrate to Prepare a NiFe-based Electrode for Water Oxidation, *ChemSusChem* 10 (2017) 394–400, <https://doi.org/10.1002/cssc.201601151>.
- [51] B. Jansi Rani, G. Ravi, R. Yuvakkumar, B. Saravanakumar, M. Thambidurai, C. Dang, D. Velauthapillai, CoNiSe2 Nanostructures for Clean Energy Production, *ACS, Omega* 5 (2020) 14702–14710, <https://doi.org/10.1021/acsomega.0c01476>.
- [52] I.C. Man, H.Y. Su, F. Calle-Vallejo, H.A. Hansen, J.I. Martínez, N.G. Inoglu, J. Kitchin, T.F. Jaramillo, J.K. Nørskov, J. Rossmeisl, Universality in Oxygen Evolution Electrocatalysis on Oxide Surfaces, *ChemCatChem* 3 (2011) 1159–1165, <https://doi.org/10.1002/cctc.201000397>.
- [53] K. Deng, T. Ren, Y. Xu, S. Liu, Z. Dai, Z. Wang, X. Li, L. Wang, H. Wang, Transition metal M (M = Co, Ni, and Fe) and boron co-modulation in Rh-based aerogels for highly efficient and pH-universal hydrogen evolution electrocatalysis, *J. Mater. Chem. A* 8 (2020) 5595–5600, <https://doi.org/10.1039/d0ta00398k>.



RESEARCH ARTICLE

View Article Online
View Journal | View Issue



Cite this: *Mater. Chem. Front.*,
2023, 7, 1365

Bimetallic Ni–Co selenide heterostructure aerogel for highly efficient overall water splitting†

Hongchen Liu, Fan Yang,* Fengjiang Chen, Sai Che, Neng Chen, Chong Xu, Ni Wu, Wenkai Wei and Yongfeng Li*

Exploring transition metal-based electrocatalysts with excellent performance toward alkaline overall water splitting is of significant importance for the hydrogen economy but remains challenging. Herein, we designed and prepared a bimetallic Ni–Co selenide heterostructure aerogel (NiSe₂–CoSe₂) for highly efficient overall water splitting via facile spontaneous gelation and selenium vapor deposition. The optimized sample exhibited extremely low overpotentials of 65/220 mV for the HER/OER at a geometric current density of 10 mA cm^{−2} in 1 M KOH electrolyte. Assembled as an electrolyzer for overall water splitting, NiSe₂–CoSe₂ only required a low cell voltage of 1.56 V to achieve 10 mA cm^{−2} with decent stability, which was comparable to those of commercial noble-metal catalysts (Pt/C + RuO₂). The exceptional performance was attributed to the unique porous morphology of the aerogel with abundant active sites and the bimetallic selenide heterostructure with excellent intrinsic activity. Density functional theory (DFT) calculations further revealed the ideal adsorption performance for reactant intermediates at the heterogeneous phase boundaries. This work provides an anticipated perspective of transition metal selenide bifunctional electrocatalysts for overall water splitting.

Received 20th October 2022,
Accepted 23rd January 2023

DOI: 10.1039/d2qm01082h

rsc.li/frontiers-materials

Introduction

Nowadays, the ever-worsening global energy crisis and environmental pollution push the development of renewable energy, especially toward ‘green hydrogen’ produced by water splitting.^{1,2} Currently, noble metal-based catalysts show the best performance for electrocatalytic water splitting with a low operating voltage. However, high cost and low reserves dramatically prevent their large-scale application.^{3,4} In this case, the development of highly active non-noble metal electrocatalysts has been a hot research topic in recent years, such as transition metal (Ni, Co, or Fe, *etc.*) alloys^{5–7} or compounds (phosphides, sulfides, selenides, nitrides or oxides, *etc.*).^{8–12} Although some of the materials demonstrate electrocatalytic hydrogen or oxygen evolution reaction (HER or OER) activities comparable to those of precious metal catalysts, the research and applications of those materials in overall water splitting are insufficient. To this end, it is particularly crucial to design and develop bifunctional non-noble metal electrocatalysts with low overpotential and good stability for highly efficient overall water splitting.

Basically, high performance electrocatalysts for the HER require moderate adsorption/desorption properties with H*,

while high performance electrocatalysts for the OER need balanced binding energy of O* between OH* and OOH*.^{3,13} In this regard, transition metal-based selenides (TMSeS) have been widely studied as a newly discovered family for water electrolysis owing to their unique features.¹⁰ As sulfide analogs, TMSeS have balanced hydrogen bonding energy, leading to favorable catalytic performance toward the HER.¹⁴ Meanwhile, some TMSeS with a cubic pyrite-type crystal structure (*e.g.* NiSe₂, CoSe₂, *etc.*) can efficiently coordinate with water/hydroxide and undergo oxidation and reduction on an anode to construct an oxide/hydroxide shell with advanced OER catalytic activity and stability.^{15,16} Besides, the unique metal-like properties of selenium allow excellent electrical conductivity of TMSeS, which leads to desirable charge transfer, reaction kinetics, and energy conversion efficiency.^{17,18} In order to further improve the intrinsic electrocatalytic capability of TMSeS, there are some recent reports on construction of heterostructures to adjust the interface electronic structures, such as NiSe₂–NiFe₂Se₄, Ni₂P–NiSe₂, NiSe₂–CoSe₂, *etc.*^{19–21} By constructing heterostructures, the charge transfer efficiency within the catalyst can be significantly enhanced due to the electricity differences of the two phases, while new active sites with a moderately regulated electronic structure that adapts for the adsorption of reaction intermediates generate at the heterogeneous phase boundaries.^{22–24} To maximally expose those highly active sites in TMSe-based heterostructures, different morphological regulation strategies have been proposed, such as designing ultra-thin nanosheets or nickel foam-based

State Key Laboratory of Heavy Oil Processing, China University of Petroleum, Changping, Beijing 102249, China. E-mail: yangfan@cup.edu.cn, yfli@cup.edu.cn

† Electronic supplementary information (ESI) available. See DOI: <https://doi.org/10.1039/d2qm01082h>

nanoarrays.^{25,26} However, the electrochemical active surface area and the amount of mass transfer paths of these structures still remain to be improved. Recently, metal aerogels have been widely researched due to their unique properties between powders and self-supporting materials. Compared with other powder materials, metal aerogels have three-dimensional interconnected network structures without carriers, which not only present a high specific area with plenty of active sites, but also provide abundant pathways for mass transfer.^{27,28} Benefiting from the advantages of the aerogel structure, some transition-metal-based structures have been reported as high-performance water electrolysis catalysts.^{29,30} For example, we have designed and prepared a P, Mo-codoped Ni aerogel (Ni-Mo-P aerogel) for electrocatalytic overall water splitting in our previous work. In contrast to the nanowires with the same composition, the Ni-Mo-P aerogel exhibits a larger electrochemical surface area and a better HER performance.³¹ Nevertheless, there are few reports dedicated to combining the TMSeS or TMSe-based heterostructures and the unique aerogel morphology for efficient overall water splitting.

In this work, a NiSe₂-CoSe₂ aerogel was prepared by spontaneous gelation and selenium vapor deposition. The bifunctional NiSe₂-CoSe₂ catalyst exhibited an impressive performance for the HER (65 mV@10 mA cm⁻²) and the OER (220 mV@10 mA cm⁻²), and the assembled symmetrical overall water splitting system required a low cell voltage of 1.56 V to achieve a current density of 10 mA cm⁻². The eminent performance of the optimized sample was attributed to the following two aspects: (1) the heterogeneous structure constructed by NiSe₂ and CoSe₂ led to the generation of active sites with ideal adsorption capability for reactant intermediates at the interface. Meanwhile, the charge transfer efficiency of the material was significantly improved due to the electrical property contrast of the two phases. (2) The NiSe₂-CoSe₂ heterostructure with higher intrinsic activity was successfully prepared with an aerogel morphology, providing a high specific surface area with lots of exposed active sites. This work provides a new perspective for the design of TMSe-based electrocatalysts for overall water splitting.

Materials and methods

Materials and reagents

Nickle chloride hexahydrate (NiCl₂·6H₂O, AR) and cobalt chloride hexahydrate (CoCl₂·6H₂O, AR) were purchased from Sino-pharm Chemical Reagent Co. Sodium borohydride (NaBH₄, 98%) was purchased from TianJin Fuchen Chemical Reagents Factory. Selenium (Se, 99.99%, powder, 100) was purchased from Adamas-beta. Pt/C (20 wt%) and RuO₂ were purchased from Alfa Aesar.

Ni-Co aerogel synthesis

In a typical preparation of the Ni-Co aerogel, 15 mL of NaBH₄ (0.1 M) solution was quickly dropped into the mixed solution of 10 mL Ni²⁺ (0.05 M) and Co²⁺ (0.05 M). After 8 hours of gelation, the Ni-Co hydrogel was formed at the bottom of the flask. After 20 h of freeze drying, moisture was removed and the Ni-Co

aerogel (Ni-Co-1:1) was obtained. As comparison samples, the molar ratio of Ni²⁺ and Co²⁺ was changed to 2:1, 1:2, 1:0 and 0:1 to prepare the Ni-Co-2:1, Ni-Co-1:2, pure Ni and Co aerogels, respectively.

NiSe₂-CoSe₂ aerogel synthesis

To fabricate the NiSe₂-CoSe₂ aerogel, 20 mg of the Ni-Co-1:1 aerogel and excess Se powder were placed at two separate positions in porcelain boats, respectively, of which Se powder was placed on the upstream side of the furnace. Then, the samples were heated up to 400 °C at 5 °C min⁻¹ and maintained at this temperature for 120 min with Ar gas flowing at 50 sccm to obtain the NiSe₂-CoSe₂ aerogel. The comparison samples prepared in the previous step were selenized in the same way to get NiSe₂-CoSe₂-2:1, NiSe₂-CoSe₂-1:2, NiSe₂ and CoSe₂ aerogels, respectively. To investigate the influence of selenide temperature and determine the best reaction conditions, NiSe₂-CoSe₂-300 and NiSe₂-CoSe₂-500 aerogels were prepared by changing the reaction temperature to 300 °C and 500 °C, respectively.

Materials characterization

Scanning electron microscopy (SEM) measurements were performed on a SU8010 microscope at an accelerating voltage of 5 kV. Transmission electron microscopy (TEM) and energy dispersive spectroscopy (EDS) images were recorded using a Tecnai G2 F20 field emission transmission electron microscope. Inductively coupled plasma-optical emission spectroscopy (ICP-OES) results were obtained from an Agilent ICPOES 730. Powder X-ray diffraction (XRD) was studied using a Bruker D8 Advance diffractometer. X-ray photoelectron spectroscopy (XPS) data of the samples were recorded on a Thermo Fisher K-Alpha American with an Al K X-ray source.

Electrochemical measurements

Samples on carbon-cloth-based electrodes were prepared for all the electrochemical measurements. In this context, 5.0 mg of the sample was dispersed in the mixed solution with 0.25 mL ethanol and 0.25 mL deionized water, containing 20 mL of Nafion (5%) under sonication for 30 min to form a homogeneous catalyst ink. Then, the obtained ink was drop-cast onto the surface of carbon cloth (1 cm × 1 cm) followed by drying at 60 °C for 5 h to achieve the loading amount of 1.0 mg cm⁻² for the sample on carbon cloth. For a comparison, Pt/C and RuO₂ on carbon cloth were also prepared for evaluating HER, OER and overall water splitting by the same method.

All the electrochemical properties of the samples were measured on a CHI 760 electrochemical workstation (CH Instruments, Inc., Shanghai) integrated with a three-electrode system at room temperature. Sample modified carbon cloth, graphite rod, and Hg/HgO acted as working, counter, and reference electrodes, respectively. The conversion potential of E (RHE) was obtained according to the following equation:

$$E(\text{RHE}) = E(\text{Hg}/\text{HgO}) + 0.059 \times \text{pH} + 0.098$$

Electrocatalytic performance of the HER and OER were tested by linear-sweep voltammetry in 1 M KOH solution at a

scan rate of 5 mV s^{-1} . The potential range of the HER and OER was -0.8 to -1.4 V and 0 to 0.8 V vs. the standard Hg/HgO electrode, respectively. All the polarization curves of the HER and OER were adjusted with 90% IR-correction according to the ohmic resistance of the solution (R_s), and the values of R_s was obtained from the electrochemical impedance spectroscopy (EIS) results under the open circuit potential. Besides, electrocatalytic performance of overall water splitting were tested by LSV on an electrolytic cell consisting of two carbon cloth electrodes with the optimized sample under the operating voltage from 1.0 to 2.0 V (without IR-correction). EIS measurements were applied to evaluate the charge transfer ability of the catalysts at a frequency range of 0.01 to 10^5 Hz under the voltage of -1.1 V . Double-layer capacitance (C_{dl}) values were assessed by cyclic voltammetry (CV) in the non-faradaic potential region ranging from -0.3 to -0.5 V vs. standard Hg/HgO electrode at 10 mV s^{-1} , 50 mV s^{-1} , 100 mV s^{-1} , 150 mV s^{-1} , and 200 mV s^{-1} . Stability of samples was tested by chronoamperometric measurement under the voltages to achieve a current density of 10 mA cm^{-2} .

Theoretical calculations

Density functional theory (DFT) calculation was performed using the DMol³ code as implemented in Materials Studio. The generalized gradient approximation of the Perdew–Burke–Ernzerhof (GGA-PBE) function was used to treat all the energy changes. The core treatment was effective core potentials (ECP) and the basis set was DNP v4.4. The k -point was set as $3 \times 3 \times 1$ and the size of vacuum region was 15 \AA . The Ni–Co model was formed by Ni(111) and Co(111) layers, and NiSe₂, CoSe₂, NiSe₂–CoSe₂ models were formed by NiSe₂(210) and CoSe₂(210) layers. The typical Ni–Co surface was modified by the $U \times 2$ and $V \times 2$ super cell of the Ni(111)–Co(111) layer, while all the selenide surfaces were modified by the $U \times 2$ and $V \times 1$ super cell of corresponding NiSe₂(210), CoSe₂(210) or NiSe₂(210)–CoSe₂(210) layers. The adsorption energies of hydrogen atoms and reaction intermediates of the OER on the structures were calculated by the following equation:

$$DG = DE + DZPE - TDS$$

In the equation, the DZPE and DS in the formula are the zero-point energy change and the entropy change between the surface and the adsorbed reaction intermediate molecule, which were obtained from the frequency calculation function of the DMol³ code. T was the temperature of the system, which was set to 298.15 K in all the calculations. Besides the DE was the binding energy of reaction intermediates and could be calculated by the following equation:

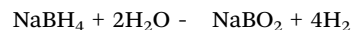
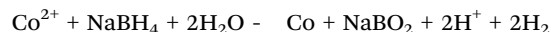
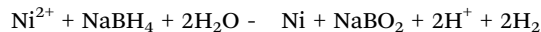
$$DE = E_{(\text{surf}+i)} - E_{(\text{surf})} - E_i$$

Herein, the $E_{(\text{surf})}$ and E_i represented the energies of the bare surface and reaction intermediates (H^* in the HER and OH^* , O^* , and OOH^* in the OER), respectively. The $E_{(\text{surf}+i)}$ was the total energy of the obtained surface structure with an adsorbed reaction intermediate molecule.

Results and discussion

Catalyst synthesis and characterizations

The synthetic procedure of the NiSe₂–CoSe₂ aerogel involved three facile steps (Fig. 1). First of all, the Ni–Co hydrogel was synthesized *via* the spontaneous NaBH₄ reduction and gelation process. The corresponding reactions of this step was described by the following equations:



During this step, the *in situ* generated H₂ gas from the reduction of Ni, Co elements and the hydrolysis of NaBH₄ served as the gas template, directing the formation of porous interconnected networks (Fig. S1, ESI†).^{31,32} Then, the corresponding aerogel was obtained by freeze-drying without damaging the morphology of the gel. Finally, the Ni–Co aerogel was annealed under a selenium vapor atmosphere to obtain the NiSe₂–CoSe₂ aerogel.

The morphologies and structures of the NiSe₂–CoSe₂ aerogel were characterized by SEM. To be specific, the Ni–Co precursor and NiSe₂–CoSe₂ aerogel exhibited the fluffy overall morphology in the large-scale images (Fig. S2(a) and (b), ESI†). Moreover, the Ni–Co aerogel presented a three-dimensional interconnected network formed by bimetallic alloy nanoparticles (Fig. 2(a)). After selenization, the NiSe₂–CoSe₂ aerogel still maintained the unique porous morphology (Fig. 2(b)), which could be further confirmed by the high-resolution SEM images (Fig. S2(c) and (d), ESI†) and low-resolution TEM images (Fig. S3, ESI†). Such a shaggy and porous structure provided abundant active sites and mass transfer pathways.^{32,33} According to reported literatures and our previous works,^{28,31,34} the type and mole ratio of metals are the key factors affecting the morphology of the aerogel. Notably, the NiSe₂–CoSe₂-2:1 and NiSe₂ aerogels with a higher Ni content tended to form the network structure composed of comparatively small nanoparticles (Fig. S4(a) and (c), ESI†), while the NiSe₂–CoSe₂-1:2 and CoSe₂ were entirely comprised of larger nanoparticles without an appreciable network skeleton (Fig. S4(b) and (d), ESI†).³⁵ In addition, the selenization temperature also played an important role in modulating the

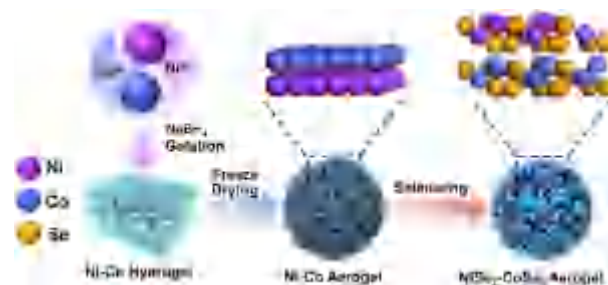


Fig. 1 Schematic illustration of the synthesis of Ni–Co and NiSe₂–CoSe₂ aerogels.

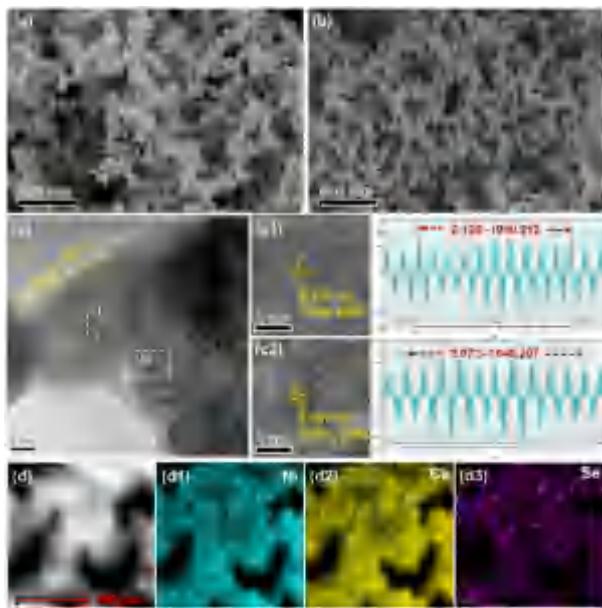


Fig. 2 (a and b) SEM images of the Ni-Co and NiSe₂-CoSe₂ aerogel. (c) HRTEM image of the NiSe₂-CoSe₂ aerogel with lattice fringes of NiSe₂ and CoSe₂ (c1 and c2). (d) STEM image of the NiSe₂-CoSe₂ aerogel and its corresponding EDX mapping of Ni, Co, Se (d1–d3).

morphology. NiSe₂-CoSe₂-300 was identified to retain the porous network structure, while NiSe₂-CoSe₂-500 agglomerated obviously and gradually lost the aerogel morphology (Fig. S5, ESI†). The HRTEM of the NiSe₂-CoSe₂ aerogel is shown in Fig. 2(c). Because of contact with air, a thick oxide layer was formed on the surface of aerogel.^{34,36} Based on the results of Fast Fourier Transform (FFT), the (220) crystal planes of NiSe₂ (0.212 nm, Fig. 2(c1)) and CoSe₂ (0.207 nm, Fig. 2(c2)) were observed, which preliminarily proved the formation of the NiSe₂-CoSe₂ heterostructure.^{21,26} Besides, the STEM-mapping of the NiSe₂-CoSe₂ aerogel showed that Ni, Co, and Se were evenly distributed in the skeleton (Fig. 2(d1)–(d3)), which revealed the construction of the selenide aerogel. Meanwhile, the Ni, Co, and Se contents of NiSe₂-CoSe₂, NiSe₂-CoSe₂-2:1 and NiSe₂-CoSe₂-1:2 were analyzed by SEM-EDS (Fig. S6, ESI†) and further confirmed by the results of ICP-OES (Table S1, ESI†). The proportion of Ni and Co in each sample conformed well to our design, while the Se contents were 30–40 wt%.

The crystalline structure of NiSe₂-CoSe₂ and comparison samples were investigated by XRD (Fig. 3(a)). The patterns of NiSe₂-CoSe₂-1:1, NiSe₂-CoSe₂-2:1 and NiSe₂-CoSe₂-1:2 aerogels exhibited the characteristic diffraction peaks of NiSe₂ (PDF#41-1495) and CoSe₂ (PDF#09-0234). Meanwhile, the selenides on the surface of the aerogel prevented selenium vapor from contacting the Ni and Co inside the skeleton, so that the corresponding peaks of Ni (PDF#04-0850) and Co (PDF#45-1027) could be observed in the patterns.¹⁹ Compared with the standard cards, the shift and superposition of NiSe₂ and CoSe₂ characteristic peaks at 301–401 could be observed, which was attributed to the lattice distortion caused by the interaction between the two selenide crystals, thus proving the formation of a bimetallic selenide heterostructure.^{37,38}

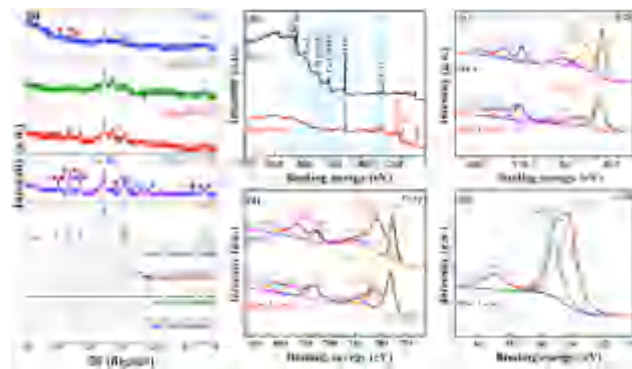


Fig. 3 (a) XRD patterns of the NiSe₂-CoSe₂ aerogel and comparison samples. (b) XPS survey spectrum of Ni-Co and NiSe₂-CoSe₂ aerogels. (c and d) High resolution Ni 2p and Co 2p XPS spectra of Ni-Co and NiSe₂-CoSe₂ aerogels. (e) High resolution Se 3d XPS spectra of the NiSe₂-CoSe₂ aerogel.

In addition, the NiSe₂ aerogel showed good crystallinity with distinct characteristic peaks of Ni and NiSe₂, but the crystallinity of the CoSe₂ aerogel was comparatively poor due to the easy formation of an amorphous oxide layer on the surface.^{39,40} Therefore, the crystallization degree of the aerogels could be regulated by constructing a bimetallic selenide heterostructure to expose highly-active crystal planes.⁴¹

XPS analysis was used to analyze the chemical states of Ni-Co and NiSe₂-CoSe₂ aerogels. As demonstrated in Fig. 3(b), the survey spectrum of Ni-Co and NiSe₂-CoSe₂ aerogels demonstrated the co-presence of Ni, Co, C, and O fundamental elements. The characteristic peak of Se 3d was observed for the NiSe₂-CoSe₂ aerogel, which indicated the generation of selenides. The high-resolution Ni 2p and Co 2p spectra were respectively manifested in Fig. 3(c) and (d), and four major peaks of Ni and Co with two satellite peaks were identified. For the Ni-Co aerogel, the peaks located at 852.1 and 869.5 eV were assigned to Ni³⁺, and the peaks at 855.5 and 873.4 eV were attributed to Ni²⁺ of Ni 2p_{3/2} and Ni²⁺ of Ni 2p_{1/2}, respectively. Similarly, the peaks located at 777.5 and 792.8 eV were fitted to Co³⁺, and the peaks at 780.5 and 796.6 eV were assigned to the Co²⁺ 2p_{3/2} and Co²⁺ of Co 2p_{1/2}, respectively.²¹ For NiSe₂-CoSe₂, the peaks of Ni²⁺ and Co²⁺ showed obvious positive shifts of 1.80 eV and 1.10 eV, respectively, indicating the electronic structure regulation due to selenization. Such alteration of electron densities around the bimetallic atoms could benefit the adsorption of OH[−] ions and the desorption of H* during alkaline electrocatalytic water splitting.⁴² Fig. 3(e) showed the Se 3d spectra of the NiSe₂-CoSe₂ aerogel. The peaks at 54.2 and 55.1 eV were assigned to Se^{2−} of Se 3d_{5/2} and Se^{2−} of Se 3d_{3/2}, while the peak at 59.0 eV was attributed to SeO_x due to air oxidation.⁴³

Electrocatalytic activity toward the HER

The electrocatalytic activity of NiSe₂-CoSe₂ toward the HER was investigated through LSV in 1.0 M KOH under a scan rate of 5 mV s^{−1}. For comparison, NiSe₂, CoSe₂, Ni-Co aerogels, and commercial Pt/C on carbon cloth with similar mass loading

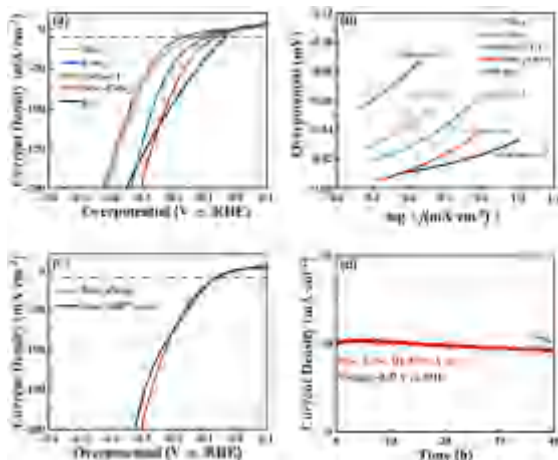


Fig. 4 (a and b) Polarization LSV curves and Tafel slopes of NiSe₂, CoSe₂, Ni-Co, and NiSe₂-CoSe₂ aerogels and Pt/C toward the HER in 1.0 M KOH. (c) Cyclic stability of NiSe₂-CoSe₂ toward the HER. (d) Chronoamperometric measurement of NiSe₂-CoSe₂ toward the HER.

were also tested (Fig. 4(a), and the curves before IR-correction are shown in Fig. S7, ESI†). The Pt/C showed the lowest overpotential of 34 mV@10 mA cm⁻², which was consistent with the reported literature.⁴⁴ The NiSe₂-CoSe₂ also afforded remarkable HER activity with an overpotential of only 65 mV@10 mA cm⁻². It obviously outperformed the counterparts of the NiSe₂ aerogel (131 mV@10 mA cm⁻²), CoSe₂ aerogel (173 mV@10 mA cm⁻²), and Ni-Co aerogel (94 mV@10 mA cm⁻²), indicating the synergic enhancement of the bimetallic selenide heterostructure. In order to determine the best ratio of Ni and Co, we also tested the HER performance of NiSe₂-CoSe₂-2:1 (84 mV@10 mA cm⁻²) and NiSe₂-CoSe₂-1:2 aerogels (92 mV@10 mA cm⁻²) (Fig. S8(a), ESI†), and the curves before IR-correction are shown in Fig. S8(b), ESI†). It was found that the sample with the balanced ratio of Ni and Co (1:1) showed the best performance, indicating the optimized construction of a heterogeneous interface under this ratio. To optimize the selenization temperature, we tested the HER performance of NiSe₂-CoSe₂-300 (95 mV@10 mA cm⁻²) and NiSe₂-CoSe₂-500 (133 mV@10 mA cm⁻²) as well (Fig. S8(c), ESI† and the curves before IR-correction are shown in Fig. S8(d), ESI†). NiSe₂-CoSe₂-300 showed similar HER performance with the Ni-Co aerogel, indicating that NiSe₂-CoSe₂-300 was barely selenized at 300 °C. Meanwhile, the performance of NiSe₂-CoSe₂-500 decreased significantly due to structural agglomeration under the elevated temperature of 500 °C. Thus, we determined that 400 °C was the optimized selenization temperature. Tafel plots were further conducted to analyze the electrocatalytic performance. In Fig. 4(b), the NiSe₂-CoSe₂ aerogel delivered a Tafel slope of 57.54 mV dec⁻¹, lower than those of NiSe₂ (95.36 mV dec⁻¹), CoSe₂ (115.68 mV dec⁻¹), and Ni-Co (75.68 mV dec⁻¹) aerogels. The low Tafel slope on the NiSe₂-CoSe₂ aerogel indicated the accelerated H₂ generation with the applied overpotential, in accordance with its high activity.³ Tafel slopes of aerogels with different metal proportions and different selenization temperatures were also calculated in Fig. S9 (ESI†), which were also

consistent with their HER performances. The cyclic stability of the NiSe₂-CoSe₂ aerogel with the best performance was tested by cyclic voltammetry and chronoamperometric measurement at an initial current density of 10 mA cm⁻² (Fig. 4(c) and (d)). A tiny deflection of LSV results was observed before and after 2000 CV cycles, verifying the impressive stability of the NiSe₂-CoSe₂ aerogel. After a 40 h test, the current density retained 97% of the initial value, which further indicated the favorable stability of the NiSe₂-CoSe₂ aerogel.

Electrocatalytic activity towards OER and overall water splitting

The OER polarization curve of the NiSe₂-CoSe₂ aerogel and contrast samples were also determined through LSV in 1.0 M KOH under a scan rate of 5 mV s⁻¹ (Fig. 5(a), and the curves before IR-correction are shown in Fig. S10, ESI†). The oxidation peaks could be observed at around 1.33 V in the curves of NiSe₂ and CoSe₂ aerogels, which represented the reconstruction process and the generation of OOH*.⁴² In contrast with the single metallic selenides, the Ni-Co aerogel exhibited a lower onset voltage of oxidation at 1.25 V, indicating that the facilitated charge transfer efficiency enhanced the reconstruction process. As Ni-Co was further selenized to NiSe₂-CoSe₂, the onset voltage of oxidation decreased to 1.23 V, demonstrating that the bimetallic selenide heterostructure had the surface that favored to reconstruct and generate active sites with excellent OER performance.¹⁰ Benefiting from the rapid reconstruction, NiSe₂-CoSe₂ exhibited the lowest overpotential of 220 mV@10 mA cm⁻², significantly better than that of NiSe₂ (304 mV), CoSe₂ (289 mV) and Ni-Co (265 mV). Notably, the performance of the NiSe₂-CoSe₂ aerogel was superior to the commercial RuO₂ (251 mV@10 mA cm⁻²), demonstrating that the selenide heterostructure possessed great application potential in the electrocatalytic OER process. Besides, NiSe₂-CoSe₂ exhibited a Tafel slope of 99.57 mV dec⁻¹, lower than that of NiSe₂ (157.71 mV dec⁻¹), CoSe₂ (131.52 mV dec⁻¹) and Ni-Co (109.47 mV dec⁻¹), which indicated the favorable reaction kinetics of the Ni-Co selenide heterostructure (Fig. 5(b)).

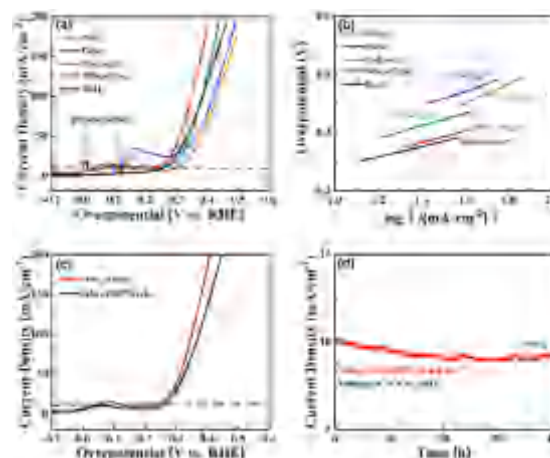


Fig. 5 (a and b) Polarization LSV curves and Tafel slopes of NiSe₂-CoSe₂, NiSe₂ and CoSe₂ aerogels and RuO₂ toward the OER in 1.0 M KOH. (c) Cyclic stability of NiSe₂-CoSe₂ toward the OER. (d) Chronoamperometric measurement of NiSe₂-CoSe₂ toward the OER.

To further illustrate the optimal metal ratio and reaction temperature, the OER properties of NiSe₂-CoSe₂-2:1, NiSe₂-CoSe₂-1:2, NiSe₂-CoSe₂-300, and NiSe₂-CoSe₂-500 aerogels were also tested (Fig. S11 and S12, ESI†). Similar to the HER, the sample with a metal ratio of 1:1 and selenization temperature of 400 °C had the best OER performance. All of the above results indicated that the optimized NiSe₂-CoSe₂ had the best OER performance due to its balanced ratio of NiSe₂/CoSe₂ and favorable morphology. Stability of NiSe₂-CoSe₂ toward the OER was also evaluated by cyclic voltammetry and chronoamperometric measurements at an initial current density of 10 mA cm⁻² (Fig. 5(c) and (d)). A deflection of LSV results was observed before and after 2000 CV cycles. Such a change in performance mainly came from the sample falling out caused by oxygen bubble overflow. After a 40 h test, 93% of the initial value of the current density was retained, indicating the favorable stability of the NiSe₂-CoSe₂ aerogel toward the OER.

In another regard, the excellent performance of NiSe₂-CoSe₂ toward both the HER and OER in an alkaline medium could also be accounted for the high charge transfer efficiency and large electrochemically active surface area (ECSA)-introduced efficient charge transfer and abundant active sites. The charge transfer resistances (R_{ct}) of NiSe₂-CoSe₂ and comparison samples were tested by EIS analysis (Fig. 6(a)). Compared with NiSe₂ (39.70 Ω), CoSe₂ (59.51 Ω), and Ni-Co (25.87 Ω) aerogels, the NiSe₂-CoSe₂ showed the lowest R_{ct} of 12.16 Ω, indicating the enhanced charge transfer ability offered by the heterostructure. Besides, we also tested the conductivities of other prepared samples (Fig. S13, ESI†). NiSe₂-CoSe₂ showed the best electron conductive performance, which further supported the optimal preparation conditions. After that, electrochemical double-layer capacitance (C_{dl}) was applied to estimate the electrochemical surface area of different samples (Fig. 6(b)) based on CV curves (Fig. S14, ESI†). The C_{dl} value of the NiSe₂-CoSe₂ aerogel was

calculated to be 18.50 mF cm⁻², which was higher than that of NiSe₂ (3.64 mF cm⁻²), CoSe₂ (3.25 mF cm⁻²), and Ni-Co (1.16 mF cm⁻²) aerogels, indicating that the heterostructure activated additional exposed active sites. The same electrochemical tests were performed on other comparison samples (Fig. S15, ESI†), and the NiSe₂-CoSe₂ aerogel exhibited a higher C_{dl} value than other aerogels, suggesting that the sufficient construction of the heterostructure based on the optimal preparation conditions could fully activate catalytic sites and provide a large electrochemical surface area. Besides, the optimized NiSe₂-CoSe₂ aerogel exhibited a C_{dl} value superior to some reported selenides or heterostructure electrocatalysts with other nanostructures (Table S2, ESI†), proving plenty of active sites and abundant mass transfer pathways provided by the aerogel skeleton.

On the basis of good activities of HER and OER, an overall water splitting cell was prepared with two NiSe₂-CoSe₂ electrodes under alkaline conditions (Fig. 6(c)). The NiSe₂-CoSe₂ aerogel device exhibited a low potential of 1.56 V@10 mA cm⁻², which was equal to the performance of Pt/C + RuO₂ (1.56 V). Note that the ratio of H₂ and O₂ was close to 2:1 (Fig. S16, ESI†), indicating that the faradaic efficiency (FE) was nearly 100% for each gas evolution reaction.²¹ Besides, the activity of NiSe₂-CoSe₂ was also comparable with other reported selenides or heterostructure electrocatalysts (Table S3, ESI†). In addition to catalytic activity, the stability of the overall water splitting cell was also investigated. Fig. 6(d) shows that the NiSe₂-CoSe₂ device had decent durability, with a current retention of 91% after 40 h operation. Furthermore, the XRD patterns of NiSe₂-CoSe₂ after the stability test of overall water splitting are shown in Fig. S17 (ESI†). The characteristic peaks of selenides (NiSe₂ and CoSe₂) and metal elements (Ni and Co) that are identical to the unreacted sample could be observed in the XRD pattern of the cathodic NiSe₂-CoSe₂ aerogel, suggesting that the overall structure and composition of the tested hybrid was unaltered. This result could indicate the superior electrochemical stability of the selenides heterostructure in the HER process.²¹ Moreover, there were no obvious peaks in the XRD pattern of the anodic NiSe₂-CoSe₂ aerogel, which was attributed to the transformation of crystal structures from selenides and metal elements to reconstructed hydroxides (Ni(OH)₂ and Co(OH)₂) and hydroxyl oxides (NiOOH and CoOOH) in the OER process.⁴²

Theoretical calculation

To further understand the origin of the observed excellent performance of both the HER and OER on the NiSe₂-CoSe₂ aerogel, theoretical calculations were conducted using density functional theory (DFT) with the Materials Studio-DMol.³ Considering the complexity of the aerogel with surface oxidation and metals without selenide, we simplified the model and focused on the interactions within the bimetallic selenide heterostructure. Based on the XRD results, we formed the models of Ni-Co, NiSe₂, CoSe₂, and NiSe₂-CoSe₂, and all structures are shown in Fig. 7(a). For the HER process, we mainly focused on the adsorption properties of metal sites (Ni or Co site) for H* (Fig. 7(b)). In the NiSe₂-CoSe₂ structure, the Ni site exhibited stronger free energy of hydrogen adsorption (ΔG_{H^*} , -0.26 eV) than that of the Co site

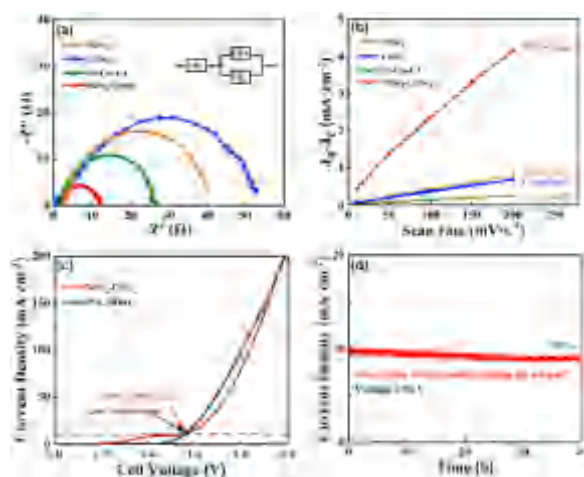


Fig. 6 (a) EIS measurements of prepared samples. (b) C_{dl} values of prepared samples. (c) LSV measurements for overall water splitting performance of the devices based on NiSe₂-CoSe₂ electrodes and Pt/C + RuO₂ electrodes. (d) Chronoamperometric measurement of NiSe₂-CoSe₂ aerogel toward overall water splitting.

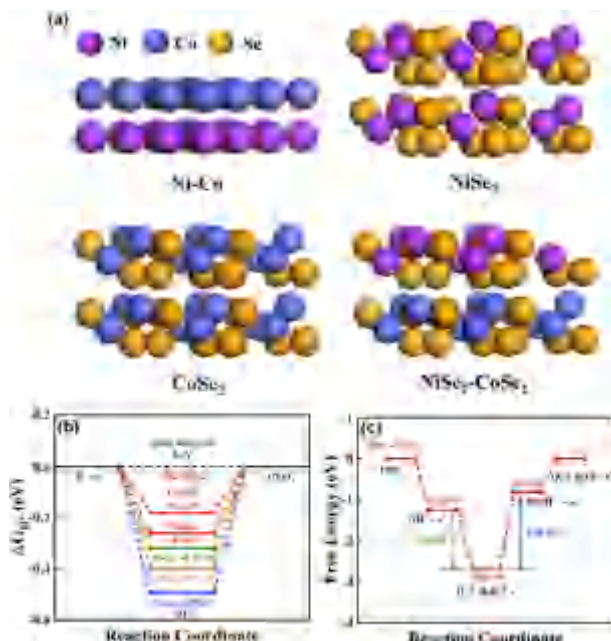
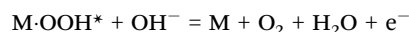
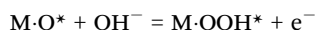
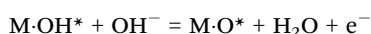
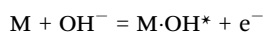


Fig. 7 (a) Crystal models of Ni-Co, NiSe₂, CoSe₂, and NiSe₂-CoSe₂ constructed based on the XRD. (b) Free energy diagram of the HER for different catalysts. (c) Free energy diagram of the OER for NiSe₂-CoSe₂.

(−0.18 eV), indicating that electrons transferred from CoSe₂ to NiSe₂ at the heterointerface. In contrast, the Co site had the DG_{H^*} closer to zero (ideal state), demonstrating the favorable adsorption properties and high activity toward the HER. Meanwhile, the Co site in NiSe₂-CoSe₂ had markedly better adsorption properties toward H* than that of Ni-Co (−0.32 eV), NiSe₂ (−0.40 eV) and CoSe₂ (−0.49 eV), indicating the superior activity toward the HER on the heterointerface between NiSe₂ and CoSe₂.²¹ Furthermore, we proposed the detailed OER mechanism of NiSe₂-CoSe₂ by DFT calculations. The OER reaction could be divided into the following 4 steps:



The calculated results (Fig. 7(c)) showed that the third electron transfer step to form *OOH exhibited the largest ladder span with an energy barrier of 1.86 eV, which was the rate-limiting step of the OER.⁴⁵ Besides, the free energy difference between the intermediates HO* and OOH* was a definite value (about 3.2 eV). When the difference of the energy barriers between HO* to O* and O* to OOH* was smaller, the OER process would be easier.⁴⁶ For the NiSe₂-CoSe₂, the difference value between the two steps was only 0.43 eV, which further validated the excellent reaction kinetics. All the theoretical calculations were in good agreement with the experimental results.

Conclusions

In summary, we designed and synthesized a NiSe₂-CoSe₂ aerogel *via* spontaneous gelation followed by a facile chemical vapor deposition selenide process. The bifunctional NiSe₂-CoSe₂ aerogel showed splendid HER, OER and overall water splitting capabilities with low potentials and favorable stabilities. Systematic characterization, electrochemical testing and DFT calculations illustrated that the superior performances were attributed to the large effective surface area of the aerogel with a three-dimensional interconnected network structure, as well as the high intrinsic activity of the heterostructure formed by NiSe₂ and CoSe₂. Our work afforded an uncomplicated approach to construct potentially scalable electrocatalysts using TMSe-based aerogels.

Conflicts of interest

There are no conflicts to declare.

Acknowledgements

The authors gratefully thank the National Natural Science Foundation of China (No. 22278431 and No. 21776302) and the Science Foundation of China University of Petroleum, Beijing (No. 2462020YXZZ033) for financial support of this work.

Notes and references

- 1 I. Staffell, D. Scamman, A. Velazquez Abad, P. Balcombe, P. E. Dodds, P. Ekins, N. Shah and K. R. Ward, The role of hydrogen and fuel cells in the global energy system, *Energy Environ. Sci.*, 2019, **12**, 463–491.
- 2 J. Schmidt, K. Gruber, M. Klingler, C. Klöckl, L. Ramirez Camargo, P. Regner, O. Turkovska, S. Wehrle and E. Wetterlund, A new perspective on global renewable energy systems: Why trade in energy carriers matters, *Energy Environ. Sci.*, 2019, **12**, 2022–2029.
- 3 J. Zhu, L. Hu, P. Zhao, L. Y. S. Lee and K. Y. Wong, Recent Advances in Electrocatalytic Hydrogen Evolution Using Nanoparticles, *Chem. Rev.*, 2020, **120**, 851–918.
- 4 E. Fabbri, A. Habereder, K. Waltar, R. Kötz and T. J. Schmidt, Developments and perspectives of oxide-based catalysts for the oxygen evolution reaction, *Catal. Sci. Technol.*, 2014, **4**, 3800–3821.
- 5 J. Greeley, T. F. Jaramillo, J. Bonde, I. Chorkendorff and J. K. Nørskov, Computational high-throughput screening of electrocatalytic materials for hydrogen evolution, *Nat. Mater.*, 2006, **5**, 909–913.
- 6 M. Chen, D. Liu, B. Zi, Y. Chen, D. Liu, X. Du, F. Li, P. Zhou, Y. Ke, J. Li, K. H. Lo, C. T. Kwok, W. F. Ip, S. Chen, S. Wang, Q. Liu and H. Pan, Remarkable synergistic effect in cobalt-iron nitride/alloy nanosheets for robust electrochemical water splitting, *J. Energy Chem.*, 2021, **65**, 405–414.
- 7 Y. Zhou, B. Tang, S. Wang and J. Long, Cu-MOF@Co-MOF derived Co-Cu alloy nanoparticles and N atoms co-doped

- carbon matrix as efficient catalyst for enhanced oxygen reduction, *Int. J. Hydrogen Energy*, 2020, **45**, 15785–15795.
- 8 A. Parra-Puerto, K. L. Ng, K. Fahy, A. E. Goode, M. P. Ryan and A. Kucernak, Supported Transition Metal Phosphides: Activity Survey for HER, ORR, OER, and Corrosion Resistance in Acid and Alkaline Electrolytes, *ACS Catal.*, 2019, **9**, 11515–11529.
 - 9 Y. Zhao, S. Wei, K. Pan, Z. Dong, B. Zhang, H. H. Wu, Q. Zhang, J. Lin and H. Pang, Self-supporting transition metal chalcogenides on metal substrates for catalytic water splitting, *Chem. Eng. J.*, 2021, **421**, 129645.
 - 10 X. Peng, Y. Yan, X. Jin, C. Huang, W. Jin, B. Gao and P. K. Chu, Recent advance and perspectives of electrocatalysts based on transition metal selenides for efficient water splitting, *Nano Energy*, 2020, **78**, 105234.
 - 11 M. S. Balogun, Y. Huang, W. Qiu, H. Yang, H. Ji and Y. Tong, Updates on the development of nanostructured transition metal nitrides for electrochemical energy storage and water splitting, *Mater. Today*, 2017, **20**, 425–451.
 - 12 I. Concina, Z. H. Ibupoto and A. Vomiero, Semiconducting metal oxide nanostructures for water splitting and photovoltaics, *Adv. Energy Mater.*, 2017, **7**, 1–29.
 - 13 J. Mohammed-ibrahim and H. Moussab, Tuning the electronic structure of the earth-abundant electrocatalysts for oxygen evolution reaction (OER) to achieve efficient alkaline water splitting – A review, *J. Energy Chem.*, 2021, **56**, 299–342.
 - 14 S. Anantharaj, S. R. Ede, K. Sakthikumar, K. Karthick, S. Mishra and S. Kundu, Recent Trends and Perspectives in Electrochemical Water Splitting with an Emphasis on Sulfide, Selenide, and Phosphide Catalysts of Fe, Co, and Ni: A Review, *ACS Catal.*, 2016, **6**, 8069–8097.
 - 15 S. Anantharaj and S. Noda, Nickel selenides as pre-catalysts for electrochemical oxygen evolution reaction: A review, *Int. J. Hydrogen Energy*, 2020, **45**, 15763–15784.
 - 16 X. Xia, L. Wang, N. Sui, V. L. Colvin and W. W. Yu, Recent progress in transition metal selenide electrocatalysts for water splitting, *Nanoscale*, 2020, **12**, 12249–12262.
 - 17 Y. Sun, K. Xu, Z. Wei, H. Li, T. Zhang, X. Li, W. Cai, J. Ma, H. J. Fan and Y. Li, Strong Electronic Interaction in Dual-Cation-Incorporated NiSe₂ Nanosheets with Lattice Distortion for Highly Efficient Overall Water Splitting, *Adv. Mater.*, 2018, **30**, 1–7.
 - 18 Y. Chen, J. Zhang, P. Guo, H. Liu, Z. Wang, M. Liu, T. Zhang, S. Wang, Y. Zhou, X. Lu and J. Zhang, Coupled Heterostructure of Mo-Fe Selenide Nanosheets Supported on Carbon Paper as an Integrated Electrocatalyst for Efficient Hydrogen Evolution, *ACS Appl. Mater. Interfaces*, 2018, **10**, 27787–27794.
 - 19 J. Yuan, X. Cheng, H. Wang, C. Lei, S. Pardiwala, B. Yang, Z. Li, Q. Zhang, L. Lei, S. Wang and Y. Hou, A Super-aerophobic Bimetallic Selenides Heterostructure for Efficient Industrial-Level Oxygen Evolution at Ultra-High Current Densities, *Nano-Micro Lett.*, 2020, **12**, 1–12.
 - 20 C. Liu, T. Gong, J. Zhang, X. Zheng, J. Mao, H. Liu, Y. Li and Q. Hao, Engineering Ni₂P-NiSe₂ heterostructure interface for highly efficient alkaline hydrogen evolution, *Appl. Catal., B*, 2020, **262**, 1–8.
 - 21 D. Chen, Z. Xu, W. Chen, G. Chen, J. Huang, J. Huang, C. Song, C. Li and K. (Ken) Ostrikov, Just add water to split water: ultrahigh-performance bifunctional electrocatalysts fabricated using eco-friendly heterointerfacing of NiCo diselenides, *J. Mater. Chem. A*, 2020, **8**, 12035–12044.
 - 22 B. Wang, C. Tang, H. F. Wang, X. Chen, R. Cao and Q. Zhang, A Nanosized CoNi Hydroxide@Hydroxysulfide Core-Shell Heterostructure for Enhanced Oxygen Evolution, *Adv. Mater.*, 2019, **31**, 1–7.
 - 23 Y. Li, W. Wang, B. Huang, Z. Mao, R. Wang, B. He, Y. Gong and H. Wang, Abundant heterointerfaces in MOF-derived hollow CoS₂-MoS₂ nanosheet array electrocatalysts for overall water splitting, *J. Energy Chem.*, 2021, **57**, 99–108.
 - 24 C. Zhang, Y. Xue, L. Hui, Y. Fang, Y. Liu and Y. Li, Graphdiyne@NiO_x(OH)_y heterostructure for efficient overall water splitting, *Mater. Chem. Front.*, 2021, **5**, 5305–5311.
 - 25 K. Xiao, L. Zhou, M. Shao and M. Wei, Fabrication of (Ni,Co)0.85Se nanosheet arrays derived from layered double hydroxides toward largely enhanced overall water splitting, *J. Mater. Chem. A*, 2018, **6**, 7585–7591.
 - 26 X. Zhang, Y. Ding, G. Wu and X. Du, CoSe₂@NiSe₂ nanoarray as better and efficient electrocatalyst for overall water splitting, *Int. J. Hydrogen Energy*, 2020, **45**, 30611–30621.
 - 27 Y. Li, S. Guo, T. Jin, Y. Wang, F. Cheng and L. Jiao, Promoted synergy in core-branch CoP@NiFe-OH nanohybrids for efficient electrochemical-/photovoltage-driven overall water splitting, *Nano Energy*, 2019, **63**, 103821.
 - 28 H. Wang, Q. Fang, W. Gu, D. Du, Y. Lin and C. Zhu, Noble Metal Aerogels, *ACS Appl. Mater. Interfaces*, 2020, **12**, 52234–52250.
 - 29 O. Lori, N. Zion, H. C. Honig and L. Elbaz, 3D metal carbide aerogel network as a stable catalyst for the hydrogen evolution reaction, *ACS Catal.*, 2021, **11**, 13707–13713.
 - 30 Z. Lin, S. Liu, Y. Liu, Z. Liu, S. Zhang, X. Zhang, Y. Tian and Z. Tang, Rational design of Ru aerogel and RuCo aerogels with abundant oxygen vacancies for hydrogen evolution reaction, oxygen evolution reaction, and overall water splitting, *J. Power Sources*, 2021, **514**, 230600.
 - 31 B. Zhang, F. Yang, X. Liu, N. Wu, S. Che and Y. Li, Phosphorus doped nickel-molybdenum aerogel for efficient overall water splitting, *Appl. Catal., B*, 2021, **298**, 120494.
 - 32 L. Liu, L. X. Chen, A. J. Wang, J. Yuan, L. Shen and J. J. Feng, Hydrogen bubbles template-directed synthesis of self-supported AuPt nanowire networks for improved ethanol oxidation and oxygen reduction reactions, *Int. J. Hydrogen Energy*, 2016, **41**, 8871–8880.
 - 33 A. A. Dubale, Y. Zheng, H. Wang, R. Hübner, Y. Li, J. Yang, J. Zhang, N. K. Sethi, L. He, Z. Zheng and W. Liu, High-Performance Bismuth-Doped Nickel Aerogel Electrocatalyst for the Methanol Oxidation Reaction, *Angew. Chem., Int. Ed.*, 2020, **59**, 13891–13899.
 - 34 B. Cai and A. Eychmüller, Promoting Electrocatalysis upon Aerogels, *Adv. Mater.*, 2019, **31**, 1–16.
 - 35 K. Deng, T. Ren, Y. Xu, S. Liu, Z. Dai, Z. Wang, X. Li, L. Wang and H. Wang, Transition metal M (M = Co, Ni, and Fe) and boron co-modulation in Rh-based aerogels for highly efficient

- and pH-universal hydrogen evolution electrocatalysis, *J. Mater. Chem. A*, 2020, **8**, 5595–5600.
- 36 F. Chen, F. Yang, H. Liu, S. Che, G. Zhang, C. Xu and Y. Li, One-pot preparation of surface vulcanization Co-Fe bimetallic aerogel for efficient sulfadiazine degradation, *Chem. Eng. J.*, 2022, **430**, 132904.
 - 37 B. Jansi Rani, G. Ravi, R. Yuvakkumar, B. Saravanakumar, M. Thambidurai, C. Dang and D. Velauthapillai, CoNiSe₂ Nanostructures for Clean Energy Production, *ACS Omega*, 2020, **5**, 14702–14710.
 - 38 C. Liu, T. Gong, J. Zhang, X. Zheng, J. Mao, H. Liu, Y. Li and Q. Hao, Engineering Ni₂P-NiSe₂ heterostructure interface for highly efficient alkaline hydrogen evolution, *Appl. Catal., B*, 2020, **262**, 1–8.
 - 39 A. Badruzzaman, A. Yuda, A. Ashok and A. Kumar, Recent advances in cobalt based heterogeneous catalysts for oxygen evolution reaction, *Inorg. Chim. Acta*, 2020, **511**, 119854.
 - 40 V. D. Nithya, Recent advances in CoSe₂ electrocatalysts for hydrogen evolution reaction, *Int. J. Hydrogen Energy*, 2021, **46**, 36080–36102.
 - 41 Y. Yang, W. Zhang, Y. Xiao, Z. Shi, X. Cao and Y. Tang, CoNiSe₂ heteronanorods decorated with layered-double-hydroxides for efficient hydrogen evolution, *Appl. Catal., B*, 2019, **242**, 132–139.
 - 42 X. Yun, T. Lu, R. Zhou, Z. Lu, J. Li and Y. Zhu, Heterostructured NiSe₂/CoSe₂ hollow microspheres as battery-type cathode for hybrid supercapacitors: Electrochemical kinetics and energy storage mechanism, *Chem. Eng. J.*, 2021, **426**, 131328.
 - 43 L. Wei, J. Luo, L. Jiang, L. Qiu, J. Zhang, D. Zhang, P. Xu and D. Yuan, CoSe₂ nanoparticles grown on carbon nanofibers derived from bacterial cellulose as an efficient electrocatalyst for hydrogen evolution reaction, *Int. J. Hydrogen Energy*, 2018, **43**, 20704–20711.
 - 44 V. H. Hoa, D. T. Tran, D. C. Nguyen, D. H. Kim, N. H. Kim and J. H. Lee, Molybdenum and Phosphorous Dual Doping in Cobalt Monolayer Interfacial Assembled Cobalt Nanowires for Efficient Overall Water Splitting, *Adv. Funct. Mater.*, 2020, **30**, 1–12.
 - 45 H. Dau, C. Limberg, T. Reier, M. Risch and S. Roggan, The Mechanism of Water Oxidation: From Electrolysis via Homogeneous to Biological Catalysis, *ChemCatChem*, 2010, **2**, 724–761.
 - 46 I. C. Man, H. Y. Su, F. Calle-Vallejo, H. A. Hansen, J. I. Martínez, N. G. Inoglu, J. Kitchin, T. F. Jaramillo, J. K. Nørskov and J. Rossmeisl, Universality in Oxygen Evolution Electrocatalysis on Oxide Surfaces, *ChemCatChem*, 2011, **3**, 1159–1165.



Contents lists available at ScienceDirect

Electrochimica Acta

journal homepage: www.journals.elsevier.com/electrochimica-acta



P-doped CoCu aerogel as a bifunctional electrocatalyst for efficient overall water splitting

Hongchen Liu, Fan Yang^{*}, Zhusong Xu, Xingru Yan, Fengjiang Chen, Chong Xu, Sai Che, Yongfeng Li^{*}

State Key Laboratory of Heavy Oil Processing, China University of Petroleum, Beijing, 102249, China

ARTICLE INFO

Keywords:

Transition metal
Aerogel
Phosphorus doping
Electrocatalyst
Overall water splitting

ABSTRACT

The exploration of bifunctional transition metal-based catalysts for water electrolysis is important for clean and large-scale production of hydrogen but yet remains challenging. Herein, a novel phosphorous doped cobalt-copper aerogel (P-CoCu) with three-dimensional interconnected structure was prepared via spontaneous gelation and in-situ P doping process. The electronic structure and charge density of Co could be modulated upon alloying with Cu, resulting in optimized charge transfer efficiency and proton adsorption energy. The hydrophilicity and the bond strength of H⁺ were further optimized through P doping, which promoted the reaction efficiency on the surface of P-CoCu. Besides, the unique porous morphology of aerogel endowed the catalyst with efficient mass transfer pathways and abundant active sites. Density functional theory (DFT) calculations further revealed the electron redistribution and the optimization of H₂ desorption performance through Cu alloying and P doping. Based on the outstanding features, the optimized P-CoCu sample achieved extremely low overpotentials of 74/224 mV for hydrogen evolution reaction (HER) / oxygen evolution reaction (OER) at a current density of 10 mA·cm⁻² in 1 M KOH electrolyte. Additionally, a two-electrode electrolytic cell assembled with P-CoCu only required an operating voltage of 1.57 V at 10 mA·cm⁻² with decent stability, which was comparable to commercial noble-metal catalysts (Pt/C//RuO₂/C) and superior to recently published electrocatalyst. This work provides an anticipated perspective of non-noble metal-based bifunctional catalysts for overall water splitting.

1. Introduction

In recent years, global energy dilemma and environmental problem promote the development and production of renewable clean energy [1]. Benefit from high gravimetric energy density and no pollutant exhaust, hydrogen is considered as one of the most potential energy sources in the future. Electrochemical overall water splitting (OWS), consisting of cathode hydrogen evolution reaction (HER) and anode oxygen evolution reaction (OER), has been widely believed as the optimal method for the mass production of hydrogen [2]. Currently, noble metal-based catalysts (Pt for HER and RuO₂, IrO₂ for OER) show the highest efficiency for electrocatalytic OWS with low overpotentials [3,4]. However, high cost and low storage of raw materials dramatically limit their large-scale application [5]. Besides, each commercial noble metal catalyst usually exhibits high activities for only one-half of OWS (HER or OER). Nevertheless, the utilization of two different catalysts at

the anode and cathode of electrolytic cell will not only reduce the stability and efficiency, but also increase the complexity and cost of OWS system due to their mismatch with each other [6]. To this end, it is significant to construct inexpensive bifunctional catalysts with high efficiencies for both OWS half reactions.

Among all non-noble-metal-based catalysts for OWS, cobalt (Co) has been widely studied in electrocatalytic HER because of its suitable adsorption/desorption properties with H⁺ and low cost [7,8]. Meanwhile, Co oxides have the moderate binding energy of O* between OH* and OOH*, leading to favorable catalytic activity for OER [9]. However, the HER/OER performance of Co-based catalysts are still inferior to that of noble-metal catalysts [10]. Up to now, numerous measures have been reported to enhance the electrocatalytic properties of Co-based materials. One effective approach is bimetallic alloying by introducing another transitional metal into the skeleton of Co lattice, such as Co-Ni nanocones, Co-Cu nanoparticles, and Co-Fe nanosheets, which can

^{*} Corresponding authors.

E-mail addresses: yangfan@cup.edu.cn (F. Yang), yfli@cup.edu.cn (Y. Li).

<https://doi.org/10.1016/j.electacta.2022.141075>

Received 2 April 2022; Received in revised form 20 August 2022; Accepted 20 August 2022

Available online 21 August 2022

0013-4686/© 2022 Elsevier Ltd. All rights reserved.

modify the coordination environment and the electronic structure of the Co atom that further leads to the appropriate interaction between catalysts and reactive intermediates [11–13]. According to the DFT calculation, Co-Cu surface alloy has more favorable hydrogen adsorption Gibbs free energy (close to zero) than other Co-based transition metallic alloys (Co-Ni, Co-Fe, etc), giving rise to better catalytic activity of HER [14]. Besides, the low resistivity of Cu endow the alloys with high intrinsic electric conductivity and charge transfer efficiency [15–17]. In addition to forming alloys, transitional metal-compounds especially transition metal phosphides (TMPs) also show promising bifunctional electrocatalytic performance in OWS [18]. P has large atomic size, high electronegativity, and strong electron-donating ability, which makes P sites effective adsorbents for proton during HER process [19]. Moreover, P atoms on the surface of TMPs can be oxidized to phosphorus (PO_4^{3-}), leading to improved intrinsic hydrophilicity and corrosion resistance [20,21]. Compared with TMPs, P doping can modulate the electronic structures without altering the original compounds type and structure of host materials, which is more conducive for surface modification [22]. Previous studies have shown that P doping can optimize the activity of Co-based catalysts for HER [23], OER [24], and OWS [25–27]. For instance, Van Hien Hoa et al. prepared Mo, P-codoped Co nanowire array (Co-Mo-P) through electrodeposition [26]. Compared to the samples without P doping, Co-Mo-P demonstrated lower impedance and better charge transfer ability than those of Co-Mo. Besides, Wang et al. fabricated a P-doped Co_3O_4 (P- Co_3O_4) nanowire array [24]. P-doping led to the decrease in the charge density and the increase in the empty d orbitals around Co in Co_3O_4 to provide more adsorption sites for OH^- .

Morphology engineering also plays a pivotal role in improving the electrocatalytic performance of materials through increasing active sites exposure and accelerating mass transfer. In recent years, metal aerogels have been widely researched due to their unique three-dimensional interconnect-network structures [28], which not only present high specific area with porous architectures, but also offer abundant pathways for mass transfer [29,30]. At present, the researches of metal aerogels mainly focus on noble-metal-based materials, such as PdPt aerogel, PtAg aerogel, PdNi aerogel, et al [31–33]. High intrinsic activities with suitable morphologies endow these aerogels with remarkable electrocatalytic performance in HER, ORR, MOR, et al [34–36]. However, up to now, the preparation and application of functionalized transition metal aerogels are rarely reported [37]. Therefore, it is significant to construct P-doped transition metal aerogels for high-performance OWS electrocatalysis.

In light of these benefits, we designed and constructed a P-doped CoCu aerogel (P-CoCu) with 3D nanowire crosslinked network by spontaneous gelation and facile P doping process. The optimal P-CoCu aerogel achieved impressive performance of 74 and 224 $\text{mV}@10 \text{ mA}\cdot\text{cm}^{-2}$ for HER and OER, and the assembled symmetrical OWS system required low operating voltage of 1.57 V to achieve a current density of $10 \text{ mA}\cdot\text{cm}^{-2}$. The excellent performance of the P-CoCu was attributed to the following three aspects: (1) Cu alloying optimized the hydrogen adsorption Gibbs free energy at the active sites, and its good electrical conductivity improved the charge transfer efficiency of the material. (2) P doping adjusted the electron density around CoCu, which promoted the adsorption of hydroxide and proton. (3) The unique structure of aerogel provided high specific surface area, leading to abundant exposed active sites and mass transfer pathways. This work provided an anticipated perspective for the construction of high performance Co-based transition metal catalysts of OWS reaction.

2. Experimental section

Materials and reagents: Cobalt chloride hexahydrate ($\text{CoCl}_2\cdot 6\text{H}_2\text{O}$, AR), copper chloride dihydrate ($\text{CuCl}_2\cdot 2\text{H}_2\text{O}$, AR), nickel chloride hexahydrate ($\text{NiCl}_2\cdot 6\text{H}_2\text{O}$, AR) and iron chloride (FeCl_3 , 97%) were purchased from Sinopharm Chemical Reagent Co., Ltd. Sodium molybdate dihydrate ($\text{Na}_2\text{MoO}_4\cdot 2\text{H}_2\text{O}$, AR) was purchased from TianJin

GuangFu Fine Chemical Research Institute. Sodium borohydride (NaBH_4 , 98%) was purchased from TianJin Fuchen Chemical Reagents Factory. Ammonium hypophosphite ($\text{NH}_4\text{H}_2\text{PO}_2$, 97%) was purchased from Aladdin. Pt/C (20 wt%) and RuO_2/C were purchased from Alfa Aesar.

CoCu aerogel synthesis: In a typical preparation of CoCu aerogel, aqueous solution of $\text{CoCl}_2\cdot 6\text{H}_2\text{O}$ (0.05 M, 5 mL) and $\text{CuCl}_2\cdot 2\text{H}_2\text{O}$ (0.05 M, 5 mL) were mixed at first. Then, NaBH_4 (0.1 M, 15 mL) solution was quickly dropped into the mixed solution of cobalt and copper ions. The color of the solution turned to black immediately. After 8 hours gelation, the CoCu hydrogel was formed at the bottom of the flask. Finally, the CoCu hydrogel was taken to freeze drying for 20 hours to obtain the corresponding aerogel. Besides, the molar ratio of Co and Cu ions was turned to 2:1, 1:2, 1:0 and 0:1 to prepare the Co_2Cu , CoCu_2 , Co and Cu aerogels, respectively. To extend this synthetic strategy to other cobalt-based transition metal aerogels, CoMo, CoNi and CoFe aerogels were prepared by the same procedures. Among them, aqueous solution of CuCl_2 was replaced by $\text{Na}_2\text{MoO}_4\cdot 2\text{H}_2\text{O}$ (0.05 M, 5 mL), $\text{NiCl}_2\cdot 6\text{H}_2\text{O}$ (0.05 M, 5 mL) and FeCl_3 (0.05 M, 5 mL), respectively.

P-CoCu aerogel synthesis: To fabricate the P-CoCu aerogel, 20 mg of CoCu aerogel and 200 mg of $\text{NH}_4\text{H}_2\text{PO}_2$ were placed at two separate positions in porcelain boats respectively, of which $\text{NH}_4\text{H}_2\text{PO}_2$ was placed on the upstream side of the furnace. Then, the samples were heated up to 250°C by $5^\circ\text{C}\cdot\text{min}^{-1}$ and maintained at this temperature for 1 h under Ar gas atmosphere (40 sccm) to construct P-CoCu aerogel. Meanwhile, the samples with different molar ratio were treated by the same method to synthesis the P- Co_2Cu , P- CoCu_2 , P-Co and P-Cu aerogels. To investigate the influence of reaction temperature, P-CoCu-350 and P-CoCu-450 aerogels were constructed by changing the reaction temperature to 350°C and 450°C , respectively. Besides, P-CoMo, P-CoNi and P-CoFe aerogels were prepared by the same procedures, in which the CoCu aerogel was replaced by CoMo, CoNi and CoFe, respectively.

Characterization: The morphologies, structures and element distributions of aerogels were characterized by scanning electron microscope (SEM, SU3500 and SU8010), transmission electron microscopy (TEM, Tecnai G2 F20) and energy disperse spectroscopy (EDS). The loose and tap bulk density of P-CoCu was tested through measuring cylinder and analytical balance. X-ray diffraction (XRD) spectra were collected by a Bruker D8 advance diffractometer. N_2 physisorption isotherms were tested by a kubo X1000 aperture and specific surface area analyzer. X-ray photoelectron spectroscopy (XPS) spectra with an Al K X-ray source were collected from a Thermo Fisher K-Alpha American.

Electrochemical Measurements: Samples on carbon-cloth-based electrodes were prepared for all the electrochemical measurements. In this context, 5.0 mg of sample was dispersed in the mixed solution with 20 μL of Nafion (5%), 0.25 mL ethanol and 0.25 mL deionized water. After 30 min sonication, the homogeneous ink was drop-cast onto a piece of carbon cloth ($1 \text{ cm} \times 1 \text{ cm}$) followed by drying at 60°C for 5 h to prepare the working electrode with the sample loading amount of $1.0 \text{ mg}\cdot\text{cm}^{-2}$. In contrast to the noble metal electrocatalysts, Pt/C and RuO_2/C on carbon cloth were also prepared for evaluating HER, OER and OWS by the same method.

An electrochemical workstation (CHI 760, CH Instruments, Inc., Shanghai) with a three electrodes electrolyzer was used to tested all the electrochemical properties. The three-electrode system with working, counter and reference electrodes was made up of carbon-cloth-based electrode, graphite rod and Hg/HgO reference electrode at room temperature. The conversion potential of E (RHE) was obtained according to Eq (1).

$$E(\text{RHE}) = E(\text{Hg} / \text{HgO}) + 0.059 \times \text{pH} + 0.098 \quad (1)$$

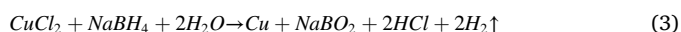
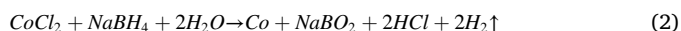
Linear-sweep voltammetry (LSV) were used to estimate the performance of HER and OER in alkaline electrolyte (1M KOH) at a scan rate of $5 \text{ mV}\cdot\text{s}^{-1}$. The testing voltage ranges toward HER and OER were -0.6 to -1.4 V and 0 to 0.8 V (vs. Hg/HgO), respectively. Besides, electrocatalytic performance of OWS were also tested by LSV on a two-

electrode system consisting of two carbon cloth electrodes with the optimized sample under the cell voltage from 1.0 to 2.0 V. Electrochemical impedance spectroscopy (EIS) measurements were applied to evaluate the intrinsic conductivities at a frequency range of 0.01 to 10^5 Hz. The double-layer capacitance (C_{dl}) values were acquired from cyclic voltammetry (CV) results under the potential range from -0.3 to -0.5 V (non-Faradaic region) at changed scan rates of $10 \text{ mV}\cdot\text{s}^{-1}$ to $50 \text{ mV}\cdot\text{s}^{-1}$. Stabilities of the optimal sample was tested through chronoamperometric measurement under the potential to achieve the current density of $10 \text{ mA}\cdot\text{cm}^{-2}$.

3. Results and discussion

3.1. Morphological and structural characterizations of P-CoCu

The preparation process of CoCu and P-CoCu aerogels was shown in Fig. 1. CoCu aerogel were first prepared via spontaneous gelation and freeze drying. In this step, Co and Cu ions were reduced to pure metal nanoparticles with the addition of reductant NaBH_4 . The involved reactions were described as Eq (2-4) [38,39]:



During this process, hydrogen worked as the gas template for the self-aggregation and assembly of Co and Cu nanoparticles, leading to the formation of interconnected nanowire networks (characteristic structure of aerogels), and the intrinsic porosity was preserved with freeze drying process. Subsequently, the P-CoCu aerogel was fabricated by the solid/gas phase reaction between CoCu aerogel and PH_3 from the decomposition of $\text{NH}_4\text{H}_2\text{PO}_2$.

The morphologies and structures of CoCu and P-CoCu aerogels was characterized by SEM. Noted that the CoCu aerogel presented three-dimensional interconnect-network structure (Fig. 2(a)). In contrast, the following P doping process resulted in moderate agglomeration of the P-CoCu (Fig. 2(b)), but the characteristic morphology of the aerogel was still maintained. The unique porous networks were confirmed by TEM images of Co, CoCu and P-CoCu aerogels (Fig. S1). Such a highly porous structure with large void space yielded the P-CoCu ultralow loose and tap bulk densities of 0.051 and 0.077 g cm^{-3} , respectively (Fig S2 and Note S1) [32]. With the increasing of doping temperature, the P-CoCu-350 and P-CoCu-450 agglomerated obviously and gradually lost the aerogel morphology (Fig. S3). Therefore, 250°C was determined as the optimal temperature for P doping. Besides, as shown in Fig. S4, significant particle fusion and structural collapse were observed in the structures with higher Cu content, such as P-CoCu₂ and P-Cu, since Cu nanoparticles tended to agglomerate during calcination. To confirm the

versatility of spontaneous gelation and in situ P doping process, the alloying composites were further extended to other Co-based dual metal aerogels (e.g. CoMo, CoNi, CoFe and their corresponding P doping aerogels), and their SEM images illustrated the similar porous network structures composed of alloy particles (Fig. S5). The high-resolution TEM (HRTEM) was carried out to analyze the hyperfine structures of P-CoCu (Fig. 2(c)). The present P-CoCu showed linear-fused particle chains composed of core-shell structure [40,41]. Lattice fringes were observed with interplanar distances of that the clear interplanar distance on the core of 0.210 nm for the core and 0.249 nm for the shell, which were assigned to Cu (111) (Fig. 2(c1)) and Co_3O_4 (111) (Fig. 2(c2)), respectively [24]. These results indicated that the P-CoCu was composed of surface oxide shell and metal core. The structure composition was further confirmed by the homogeneous distribution of Co, Cu, and O signals in the elemental mapping analysis of both CoCu and P-CoCu (Fig. S6). Moreover, the signal of P signals emerged and matched the skeleton of Co and Cu well in P-CoCu (Fig. 2(d)), revealing the successful construction of P doped CoCu alloy structure.

The porosities of the CoCu and the P-CoCu were measured by N_2 adsorption experiments at 77 K (Fig. 3(a)). Brunauer-Emmett-Teller (BET) surface areas were determined to be 52.19 and $33.49 \text{ m}^2\cdot\text{g}^{-1}$ for the CoCu and P-CoCu, respectively, indicating that the agglomeration of alloy particles caused by the calcined P doping process slightly reduced the specific surface area of aerogels. It was noteworthy that P-CoCu had a larger pore volume than the pristine CoCu aerogel, which could be attributed to the PH_3 etching effect to the skeleton of aerogel [42]. In addition, the influence of Co/Cu ratio on the porosity of the aerogel was also investigated (Fig. S7 and Table S1). The specific surface areas of the samples from the highest to the lowest were P-Co₂Cu, P-CoCu, P-CoCu₂, P-Co and P-Cu. During hydrogel formation, the rapid and violent reduction reaction of Cu ions led to the generation of large hydrogen bubbles, which acted as the gas template and resulted in more inner porosity of network [34,36]. Therefore, Co-Cu alloy aerogels had relatively higher specific surface area than the single-metal counterparts. During P doping, since Co showed a lower tendency of aggregation than Cu, the aerogels with higher Co ratios preserved better morphology with relatively larger surface areas. These investigations provide significant guidance for the design of P-doped transition metal aerogels.

The crystallinities of CoCu and P-CoCu were analyzed through XRD. As shown in Fig. 3(b), the diffraction peaks at 43.3 , 50.4 , and 74.1° of CoCu were fitted with the (111), (200), (220) crystalline planes of elemental Cu (PDF#04-0836), while the peaks at 31.3 and 36.8° were related to the (220) and (311) crystalline planes of Co_3O_4 (PDF#43-1003). These results corresponded with the previous morphology characterizations, further indicating that the aerogel was composed of pure metal particles and surface oxides. After P doping, the intensity of Cu (111) peak increased, while the diffraction peaks corresponding Co (111) and (200) at 44.2 and 51.5° appeared (PDF#15-0806), which was attributed to the recrystallization of Co and Cu with the reduction of PH_3

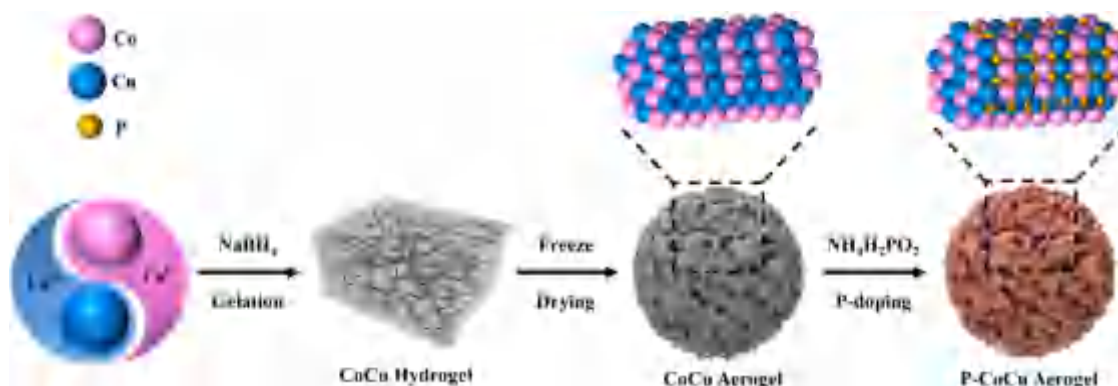


Fig. 1. Schematic illustration for the synthesis of P-CoCu aerogels

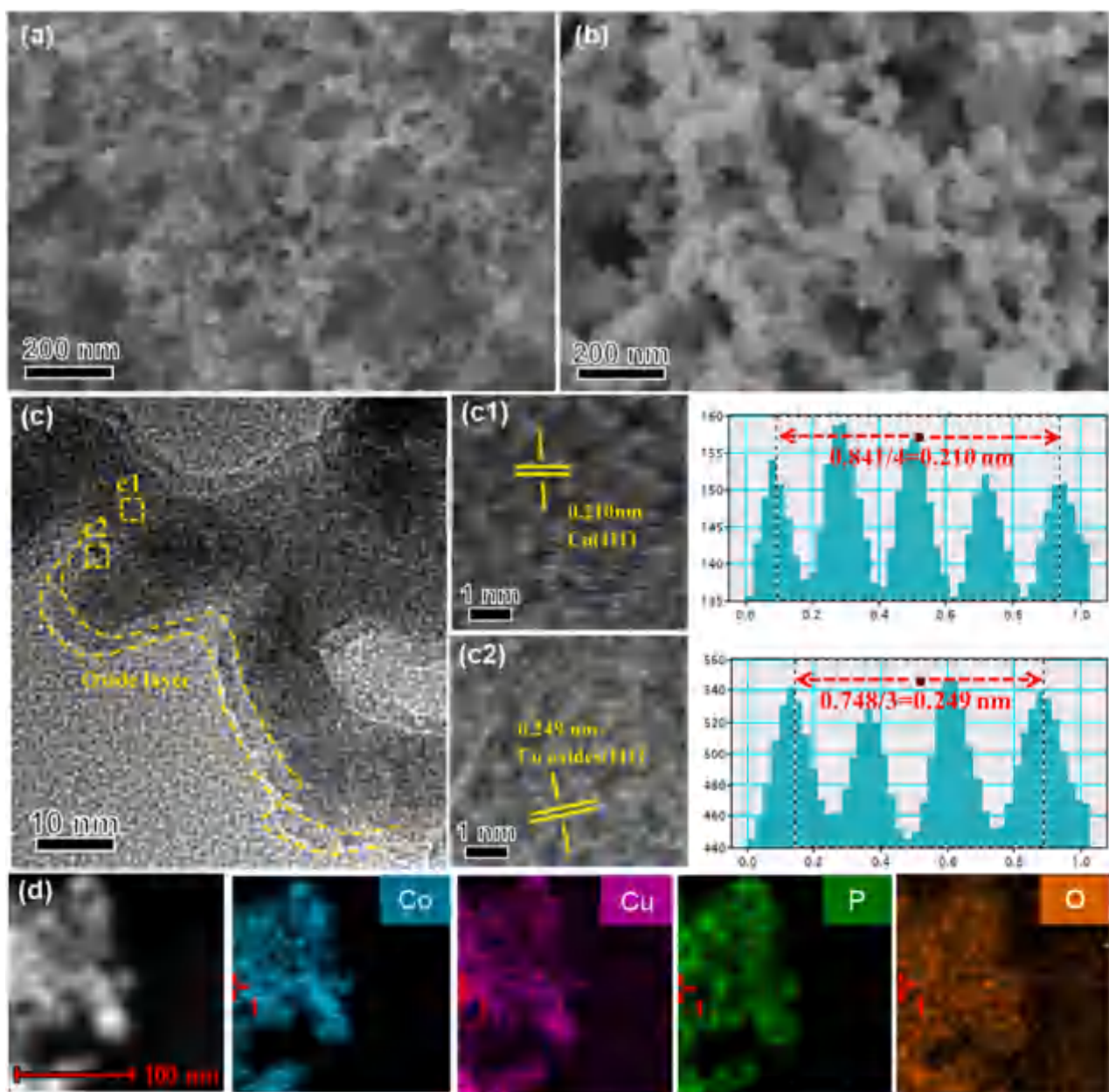


Fig. 2. SEM image of CoCu aerogel (a) and P-CoCu aerogel (b). HRTEM image of P-CoCu aerogel (c) with lattice fringe (c1-c2). STEM-mapping P-CoCu aerogel (d).

[41]. Notably, the doping P did not transform the peak pattern of Co and Cu, and no corresponding peaks of elemental P or phosphide appeared. Instead, compared with the standard cards of Co and Cu, the Co (111) and Cu (111) peaks shifted to a higher angle after P doping, which could be attributed to the crystal lattice expansion with P atoms insertion [43, 44].

Furthermore, XPS characterizations were applied to investigate the elemental states of CoCu and P-CoCu. The survey XPS spectra of both CoCu and P-CoCu included the noticeable peaks of Co 2p and Cu 2p at 776 and 930 eV, respectively (Fig. 3(c)). Moreover, the additional peak of P 2p was observed at 132 eV for P-CoCu, indicating the successful doping of P atoms. The Co 2p spectra could be deconvoluted into three sets of bi-peaks of Co 2p 1/2 and Co 2p 3/2, including 777.8 and 792.0 eV for Co⁰, 780.9 and 796.7 eV for Co²⁺, 784.8 and 802.7 eV for satellite peaks (Fig. 3(d)) [24,26]. Among them, the peaks of Co⁰ were not obvious, indicating that Co mainly existed as oxides on the shell. After P doping, the peaks of Co⁰ completely disappeared, which was caused by the surface phosphorating in this step. Because of the electron

interactions, a negative shift of the Co 2p could be observed in the spectra of P-CoCu, confirming the redistribution of electron caused by P doping. With the introduced electronic interactions, a negative shift of the Co 2p was observed in P-CoCu, confirming the redistribution of electron caused by P doping. Based on the d-band center theory, this phenomenon would cause the positive shift of d-band center of Co, leading to the improved H⁺ adsorption performance [45]. The Cu 2p XPS of CoCu was deconvoluted into two pairs of peaks of Cu 2p 1/2 and Cu 2p 3/2, with 931.2 and 952.0 eV for Cu⁰, 933.8 and 953.8 eV for Cu²⁺ (Fig. 3(e)). In contrast to Co, the peaks of Cu⁰ were dramatically more pronounced than those of Cu²⁺, indicating that Cu mainly existed in the form of elemental substance, consistent with the previous analysis of HRTEM. After P doping, due to the change of electron distribution, the characteristic peaks of Cu²⁺ also showed a negative shift and merged into the peak of Cu⁰ [15]. Fig. 3(f) showed the characteristic peaks of P 2p at 130.3 and 133.1 eV, which corresponded to M-P bond and P-O bond. This result suggested that P mainly existed in the oxidized state in P-CoCu, which powerfully bonded with Co-Cu alloy and affected the

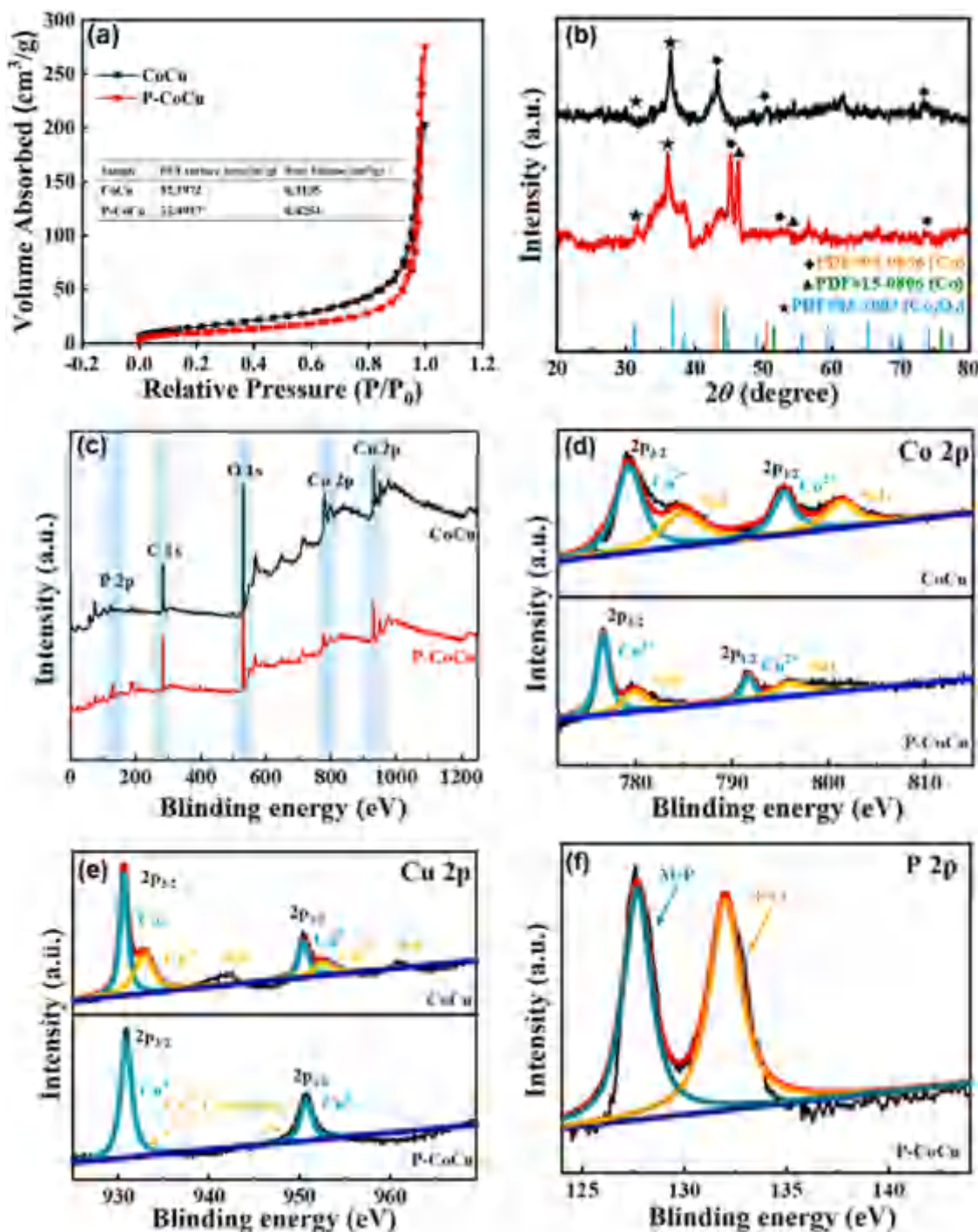


Fig. 3. Chemical composition and structure characterization of CoCu and P-CoCu aerogels: N₂ physisorption isotherms (a). XRD patterns (b). XPS survey spectrum of CoCu and P-CoCu aerogels (c). High resolution XPS spectra of Co 2p (d), Cu 2p (e) and P 2p (f).

surface charge distribution [46].

3.2. HER performances of P-CoCu

The electrocatalytic HER performances were first tested with LSV in 1.0 M KOH alkaline electrolyte (Fig. 4(a) - Fig. 4(c)). It could be seen that the commercially available Pt/C had a low overpotential of 34 mV@10 mA·cm⁻² [26]. With inferior intrinsic activity, Co aerogel showed a relatively low electrocatalytic performance with the highest overpotential of 142 mV@10 mA·cm⁻², and the large Tafel slope value of 161.93 mV·dec⁻¹ further indicated the slow HER kinetics. When Cu was

introduced into Co aerogel, the overpotential of CoCu dropped to 128 mV@10 mA·cm⁻², while the Tafel slope dropped to 138.39 mV·dec⁻¹. The enhanced activity was ascribed to the synergy of the two metals and the improved charge transfer efficiency caused by Cu core introduction. After P doping, HER catalytic performance of the P-CoCu revealed significant increase with a low overpotential and Tafel slope value of 74 mV@10 mA·cm⁻² and 101.75 mV·dec⁻¹. Further analysis showed that P doping effectively modulated the electronic configuration, promoted the adsorption of reactants (H₂O and H in alkaline medium), and increased catalytic active sites. Although the activity was still lower than that of the benchmark Pt/C, P-CoCu aerogel showed superior HER performance

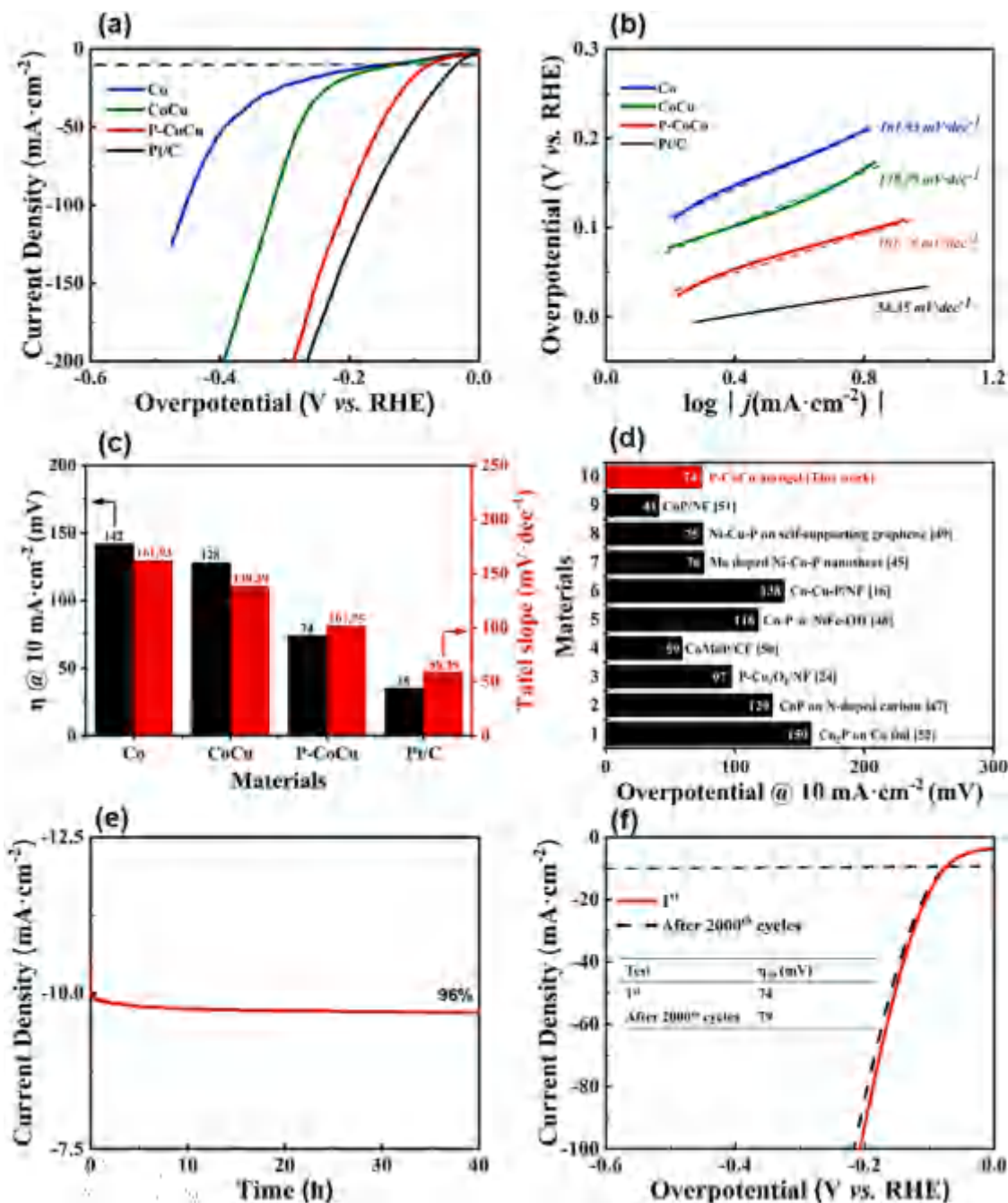


Fig. 4. Electrocatalytic activity tests of P-CoCu toward HER: Polarization LSV curves in 1.0 M KOH (a). Tafel slopes (b). η_{10} values and Tafel slopes of different samples (c). Comparison of HER performance between P-CoCu and previous reports (d). Chronoamperometric measurement (e). Cyclic stability (f).

among transition-metal-based electrocatalysts (Fig. 4(d)) [16,24,45, 47–52]. The cyclic stability of P-CoCu with the optimized performance was tested through chronoamperometric measurement under a constant potential of 74 mV (Fig. 4(e)). After 40 h test, 96% of the initial current density retained, demonstrating the favorable durability of P-CoCu. Meanwhile, negligible shift in LSV curve was observed after 2000 CV cycles (Fig. 4(f)), which further verified the long-term stability of P-CoCu.

In order to further investigate the influence of preparation condition and composition on the electrocatalytic HER performance, the same electrochemical tests were performed on other prepared samples (Fig. S8). Fig. S8(a)–(b) showed the electrocatalytic HER performance of P doped aerogels with different in-situ P doping temperatures. Among them, the sample prepared at 250°C exhibited the best electrocatalytic

properties due to the intact morphology without apparent agglomeration. Thus, under the premise that the $\text{NH}_4\text{H}_2\text{PO}_4$ could be decomposed to produce PH_3 (around 250°C), low doping temperatures yielded the best properties. The molar ratio of Co and Cu also played an important role in the HER performance (Fig. S8(c)–(d)). The activities of the samples were in the order of P-CoCu, P-CoCu₂, P-Co₂Cu, P-Co, and P-Cu. We attributed this to the larger the specific surface area of P-CoCu and P-CoCu₂ that led to more exposed activity sites. Compared with P-CoCu₂, P-CoCu with the balanced molar ratio of Co and Cu (1:1) demonstrated better synergy between two metals. Fig. S8(e)–(f) exhibited the electrocatalytic HER properties of various P doped Co-based aerogels. Benefiting from the best synergistic effect and excellent charge transfer efficiency with Cu alloying, P-CoCu showed better electrocatalytic activities of HER than P-CoMo, P-CoNi and P-CoFe [16].

3.3. OER and OWS performances of P-CoCu

The OER performance of the synthesized samples were also investigated through LSV in 1.0 M KOH alkaline electrolyte (Fig. 5(a) - Fig. 5(c)). The overpotential of Co, CoCu, and P-CoCu were 318, 286, and 224 mV@10 mA·cm⁻² with Tafel slope values of 130.99, 128.58, and 122.54 mV·dec⁻¹, respectively. Notably, the overpotential of CoCu at 10 mA·cm⁻² was comparable with that of noble-metal catalyst (RuO₂, 277 mV), while that of P-CoCu was significantly lower than RuO₂. Compared with recently reported transition-metal-based electrocatalysts, the P-CoCu represented a lower overpotential, confirming its high-activity toward OER. (Fig. 5(d)) [24,25,45,53-58]. Chronoamperometric measurement was also applied to evaluate the OER stability of P-CoCu under

a constant potential of 224 mV (Fig. 5(e)). The P-CoCu maintained a current density of 93% of the initial value, which was slightly lower than that of HER. This result was attributed to the catalyst shedding caused by the releasing of large oxygen bubbles on the surface of anode. This observation was also confirmed by the slightly larger deviation of LSV curve after 2000 CV cycles. Same electrochemical tests of OER were performed on other prepared samples, and the OER performance followed the same order as HER discussed previously (Fig. S9). Therefore, with the help of Cu and P, the optimized P-CoCu received best OER electrocatalytic activity.

To further understand the origin of observed excellent performance of both HER and OER on P-CoCu, density functional theory (DFT) calculations were applied using Materials Studio-DMol³. To reduce the

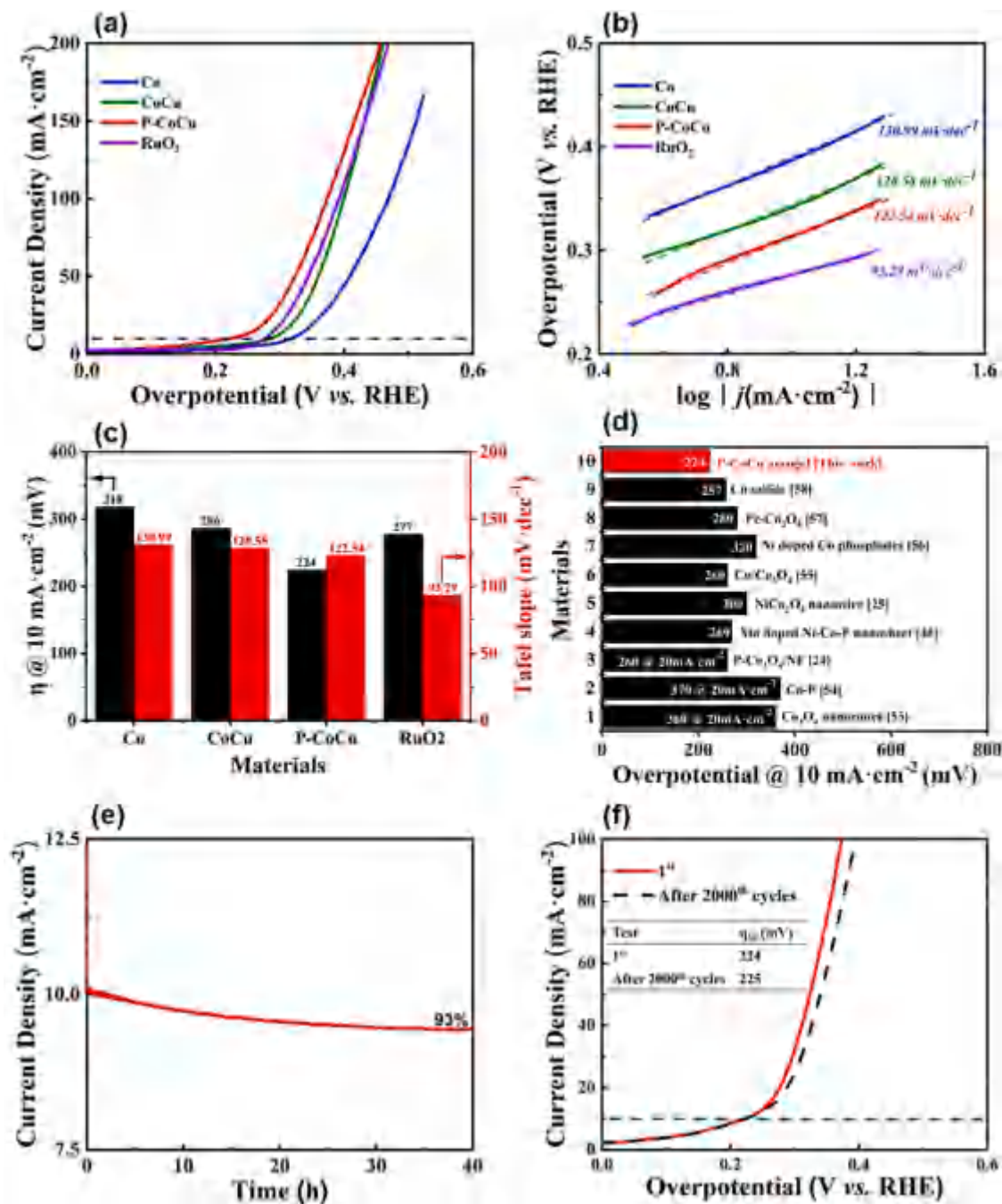


Fig. 5. Electrocatalytic activity tests of P-CoCu toward OER: Polarization LSV curves in 1.0 M KOH (a). Tafel slopes (b). η₁₀ values and Tafel slopes of different samples (c). Comparison of OER performance between P-CoCu and previous reports (d). Chronoamperometric measurement (e). Cyclic stability (f).

complexity of aerogel model, we mainly focused on the interactions between the alloys and doped P atoms [26]. Detailed modeling parameters were shown in supporting information (Fig. S10, Note S2). Firstly, we evaluated the binding abilities of Co, CoCu and P-CoCu toward reactive intermediate through the densities of states (DOS) results (Fig. 6a). The d-band center locations of Co, Cu and P-CoCu were 0.580, 0.632 and 0.108 eV, respectively. Obviously, the d-band center of P-CoCu was the closest to the Fermi level (0 eV), implying the ideal adsorption capacity toward reactive intermediate and best electrocatalytic activity [59]. Fig. 6b showed the free energy diagram of HER steps in alkaline medium. The HER pathway in alkaline electrolyte could be divided into three phases: water adsorption and dissociation (translated into H^* and OH^*), OH^* transformation to OH^- , H_2 formation and desorption [42]. Among the three models, the surface of Co was most prone to water dissociation with the most negative free energy of -0.33 eV, which led to insuperable energy barrier (0.25 eV) of the H_2 desorption step. After alloy construct and P doping, the energy barrier of H_2 desorption decreased to 0.13 eV on CoCu and 0.07 eV on P-CoCu, which indicated the highest H_2 desorption efficiency and fastest HER kinetics on the surface of P-CoCu [60]. All above theoretical calculation results rationalized the excellent electrocatalytic performance of P-CoCu.

Moreover, good electrical conductivity and abundant active sites are vital for the favorable electrochemical activities of P-CoCu. The conductivity of P-CoCu was evaluated by EIS analysis (Fig. 7(a)). Compared with Co and CoCu, the P-CoCu showed the lowest charge transfer resistance (R_{ct} , 21 Ω), demonstrating the excellent charge transfer ability offered by Cu core and strong electron-donating effect from doped P. Besides, the conductivities of other prepared samples were also investigated (Fig. S11(a)-(c)). P-CoCu showed the best charge transfer performance among all $P-Co_xCu_y$ contrast samples, which further indicated the optimal ratio of the two metals. Meanwhile, P-CoCu had lower intrinsic resistance than other P-CoM aerogels, which was attributed to the better conductivity of Cu than that of other transition metals [15, 17]. After that, we used electrochemical double-layer capacitance (C_{dl}) to estimate the electrochemically effective surface area (ECSA) of different samples (Fig. 7(b)). The C_{dl} value of P-CoCu was calculated to be 10.95 $mF\ cm^{-2}$, higher than that of Co (7.15 $mF\ cm^{-2}$) and CoCu (10.28 $mF\ cm^{-2}$). The ECSA values were calculated by the following formula:

$$ECSA = C_{dl}/C_s \quad (5)$$

where C_s was a constant with a value of 0.04. The corresponding ECSA value of Co, CoCu, and P-CoCu were 179, 257, and 274 cm^2 , respectively. This result demonstrated that the largest amount of electrocatalytic active sites were exposed in P-CoCu due to improvement in

charge transfer efficiency of aerogel skeleton caused by Cu alloying and P doping. It is worth mentioning that although the BET specific surface area was reduced, the active sites in P-CoCu were fully activated by P doping, leading to a larger ECSA value than CoCu [61,62]. The same electrochemical tests were performed on other control samples (Fig. S11 (d)-(f)). P-CoCu exhibited the highest C_{dl} values than other samples, indicating the existence of abundant active sites from the most balanced metal ratio and intact structure [63,64].

On the basis of good activities of HER and OER, an alkaline electrolyzer with two working electrodes was set up with the optimized P-CoCu electrocatalyst to test the performance of OWS (Fig. 7(c)). The P-CoCu//P-CoCu device exhibited a low potential of 1.57 V @ 10 $mA\ cm^{-2}$, which was similar to the cell voltage of noble-metal-based electrolyzer (Pt/C//RuO₂/C, 1.56 V) at the same current density. Compared with other reported bifunctional electrocatalysts, the performance of P-CoCu for OWS was also commendable (Fig. 7(d)) [24,45, 50,65-70]. Besides, the OWS stability of P-CoCu was also investigated by chronoamperometric measurement and long-term electrocatalytic cycles. P-CoCu showed the decent durability with 90% current density residual after 40 h operation and a minor increase of cell voltage after 2000 CV cycles (Fig. 7(e)-(f)). The loss of performance mainly came from the catalyst shedding caused by the bubbles releasing on the surface of anode, same as the stability test of OER. Therefore, the P-CoCu aerogel could serve as a favorable bifunctional electrocatalyst with excellent catalytic properties and decent stabilities.

4. Conclusion

In this work, we designed and synthesized a P-doped CoCu aerogel via spontaneous gelation and facile P doping process. The bifunctional P-CoCu showed splendid electrocatalytic performances toward HER, OER and OWS with low overpotential and operating voltage. Such a remarkable performance was put down to the three-dimensional interconnect-network structure of aerogel as well as the electronic structure regulation of Co by Cu alloying and P doping. Among them, the metallic aerogel skeleton offered abundant active sites and massive pathway for mass transfer. Cu alloying introduced synergistic effect between two metallic sites, thus further enhancing the charge transfer efficiency. P doping redistributed the electronic structures around CoCu alloy, resulting in the optimized adsorption property toward reactive intermediates as well as the lower energy barrier of H_2 desorption. Our work afforded an uncomplicated and widely applicable method to construct non-noble metal-based bifunctional electrocatalysts for overall water splitting with favorable properties.

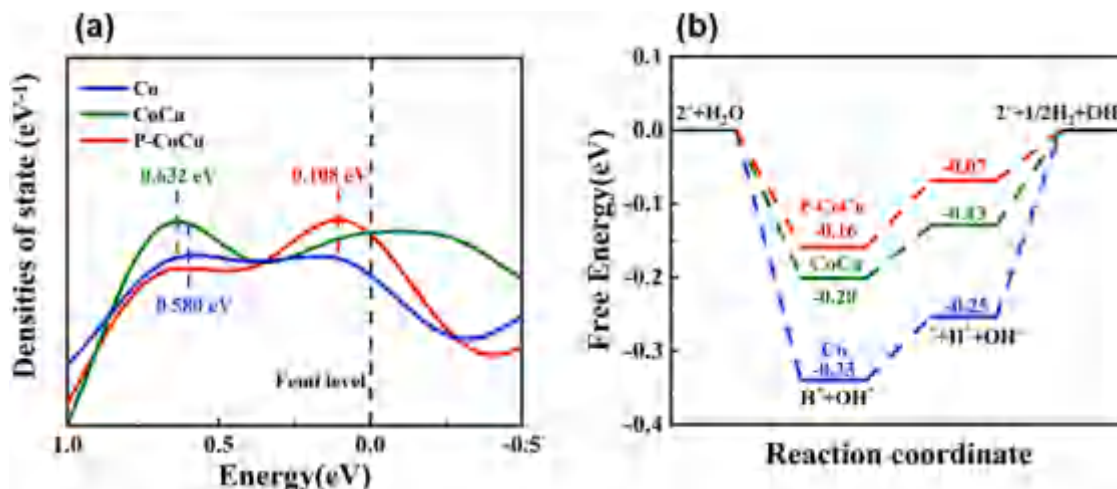


Fig. 6. Calculated DOS of Co, CoCu and P-CoCu aerogels (a). Free energy at each step of HER in alkaline medium (b).

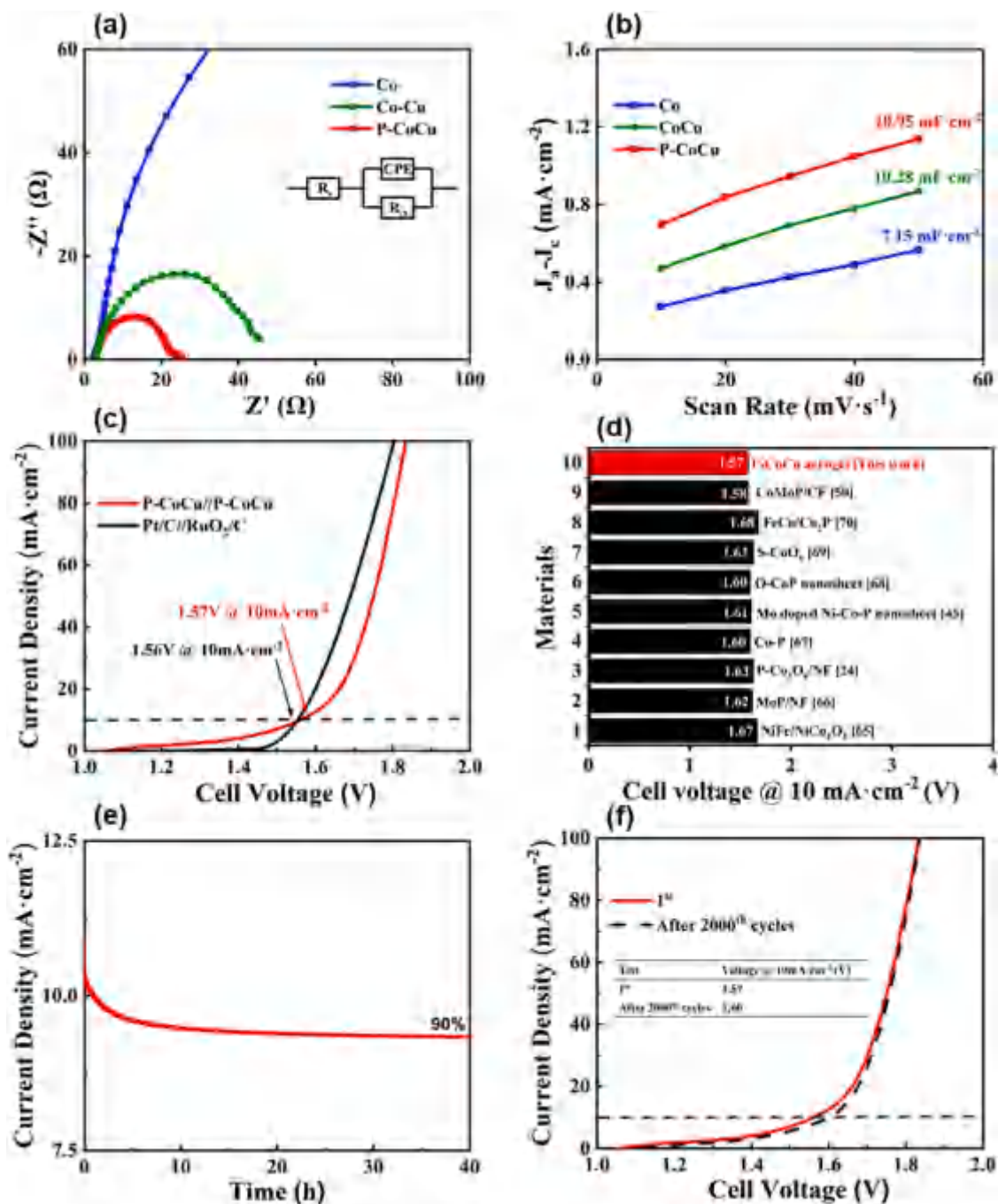


Fig. 7. Electrocatalytic activity tests of P-CoCu toward OWS: EIS measurements of prepared samples (a). C_{dl} curves and values of prepared samples (b). Polarization LSV curves of the devices based on P-CoCu//P-CoCu electrodes and Pt/C//RuO₂/C electrodes in 1.0M KOH (c). Comparison of OWS cell voltage between P-CoCu and previous reports (d). Chronoamperometric measurement (e). Cyclic stability (f).

CRediT authorship contribution statement

Hongchen Liu: Writing – review & editing, Writing – original draft, Formal analysis, Investigation, Conceptualization. **Fan Yang:** Writing – review & editing, Writing – original draft, Formal analysis, Conceptualization. **Zhusong Xu:** . **Xingru Yan:** Data curation, Writing – original draft. **Fengjiang Chen:** Investigation, Writing – review & editing. **Chong Xu:** Investigation, Formal analysis. **Sai Che:** Investigation, Formal analysis. **Yongfeng Li:** Writing – review & editing, Writing – original draft, Supervision.

Declaration of Competing Interest

The authors declare that they have no known competing financial interests or personal relationships that could have appeared to influence the work reported in this paper.

Data Availability

The data that has been used is confidential.

Acknowledgements

We gratefully thank for the National Natural Science Foundation of China (Nos. 21776302 and 21776308) and the Science Foundation of China University of Petroleum, Beijing (No. 2462020YXZZ033).

Supplementary materials

Supplementary material associated with this article can be found, in the online version, at doi:[10.1016/j.electacta.2022.141075](https://doi.org/10.1016/j.electacta.2022.141075).

References

- [1] J. Schmidt, K. Gruber, M. Klingler, C. Klöckl, L. Ramirez Camargo, P. Regner, O. Turkovska, S. Wehrle, E. Wetterlund, A new perspective on global renewable energy systems: Why trade in energy carriers matters, *Energy Environ. Sci.* 12 (2019) 2022–2029, <https://doi.org/10.1039/c9ee00223e>.
- [2] I. Staffell, D. Scamman, A. Velazquez Abad, P. Balcombe, P.E. Dodds, P. Ekins, N. Shah, K.R. Ward, The role of hydrogen and fuel cells in the global energy system, *Energy Environ. Sci.* 12 (2019) 463–491, <https://doi.org/10.1039/c8ee01157e>.
- [3] J. Zhu, L. Hu, P. Zhao, L.Y.S. Lee, K.Y. Wong, Recent advances in electrocatalytic hydrogen evolution using nanoparticles, *Chem. Rev.* 120 (2020) 851–918, <https://doi.org/10.1021/acs.chemrev.9b00248>.
- [4] E. Fabbri, A. Habereeder, K. Waltar, R. Köt, T.J. Schmidt, Developments and perspectives of oxide-based catalysts for the oxygen evolution reaction, *Catal. Sci. Technol.* 4 (2014) 3800–3821, <https://doi.org/10.1039/c4cy00669k>.
- [5] Y. Luo, L. Tang, U. Khan, Q. Yu, H.M. Cheng, X. Zou, B. Liu, Morphology and surface chemistry engineering toward pH-universal catalysts for hydrogen evolution at high current density, *Nat. Commun.* 10 (2019) 1–9, <https://doi.org/10.1038/s41467-018-07792-9>.
- [6] Y. Tian, X. Xue, Y. Gu, Z. Yang, G. Hong, C. Wang, Electrodeposition of Ni3Se2/ MoS₂ as a bifunctional electrocatalyst towards highly-efficient overall water splitting, *Nanoscale* 12 (2020) 23125–23133, <https://doi.org/10.1039/d0nr07227c>.
- [7] P. Rekha, S. Yadav, L. Singh, A review on cobalt phosphate-based materials as emerging catalysts for water splitting, *Ceram. Int.* 47 (2021) 16385–16401, <https://doi.org/10.1016/j.ceramint.2021.02.215>.
- [8] R.A. Ciuffo, S. Han, M.E. Floto, J.E. Eichler, G. Henkelman, C.B. Mullins, Hydrogen desorption from the surface and subsurface of cobalt, *Phys. Chem. Chem. Phys.* 22 (2020) 15281–15287, <https://doi.org/10.1039/d0cp02410d>.
- [9] A. Badruzzaman, A. Yuda, A. Ashok, A. Kumar, Recent advances in cobalt based heterogeneous catalysts for oxygen evolution reaction, *Inorganica Chim. Acta.* 511 (2020), 119854, <https://doi.org/10.1016/j.ica.2020.119854>.
- [10] K. Dai, N. Zhang, L. Zhang, L. Yin, Y. Zhao, B. Zhang, Self-supported Co/CoO anchored on N-doped carbon composite as bifunctional electrocatalyst for efficient overall water splitting, *Chem. Eng. J.* 414 (2021), 128804, <https://doi.org/10.1016/j.cej.2021.128804>.
- [11] G.B. Darband, M. Aliofkhazraei, A.S. Rouhaghdam, M.A. Kiani, Three-dimensional Ni-Co alloy hierarchical nanostructure as efficient non-noble-metal electrocatalyst for hydrogen evolution reaction, *Appl. Surf. Sci.* 465 (2019) 846–862, <https://doi.org/10.1016/j.apsusc.2018.09.204>.
- [12] Y. Zhou, B. Tang, S. Wang, J. Long, Cu-MOF@Co-MOF derived Co-Cu alloy nanoparticles and N atoms co-doped carbon matrix as efficient catalyst for enhanced oxygen reduction, *Int. J. Hydrogen Energy.* 45 (2020) 15785–15795, <https://doi.org/10.1016/j.ijhydene.2020.04.049>.
- [13] M. Chen, D. Liu, B. Zi, Y. Chen, D. Liu, X. Du, F. Li, P. Zhou, Y. Ke, J. Li, K.H. Lo, C. T. Kwok, W.F. Ip, S. Chen, S. Wang, Q. Liu, H. Pan, Remarkable synergistic effect in cobalt-iron nitride/alloy nanosheets for robust electrochemical water splitting, *J. Energy Chem.* 65 (2021) 405–414, <https://doi.org/10.1016/j.jechem.2021.05.051>.
- [14] J. Greeley, T.F. Jaramillo, J. Bonde, I. Chorkendorff, J.K. Nørskov, Computational high-throughput screening of electrocatalytic materials for hydrogen evolution, *Nat. Mater.* 5 (2006) 909–913, <https://doi.org/10.1038/nmat1752>.
- [15] A. Kumar, V.Q. Bui, J. Lee, A.R. Jadhav, Y. Hwang, M.G. Kim, Y. Kawazoe, H. Lee, Modulating interfacial charge density of NiP₂-FeP₂ via coupling with metallic Cu for accelerating alkaline hydrogen evolution, *ACS Energy Lett.* 6 (2021) 354–363, <https://doi.org/10.1021/acscenergylett.0c02498>.
- [16] Y.S. Park, W.S. Choi, M.J. Jang, J.H. Lee, S. Park, H. Jin, M.H. Seo, K.H. Lee, Y. Yin, Y. Kim, J. Yang, S.M. Choi, Three-dimensional dendritic Cu-Co-P electrode by one-step electrodeposition on a hydrogen bubble template for hydrogen evolution reaction, *ACS Sustain. Chem. Eng.* 7 (2019) 10734–10741, <https://doi.org/10.1021/acssuschemeng.9b01426>.
- [17] S. Li, M. Li, Y. Ni, Grass-like Ni/Cu nanosheet arrays grown on copper foam as efficient and non-precious catalyst for hydrogen evolution reaction, *Appl. Catal. B Environ.* 268 (2020), 118392, <https://doi.org/10.1016/j.apcatb.2019.118392>.
- [18] Z. Liu, X. Yu, H. Xue, L. Feng, A nitrogen-doped CoP nanoarray over 3D porous Co foam as an efficient bifunctional electrocatalyst for overall water splitting, *J. Mater. Chem. A.* 7 (2019) 13242–13248, <https://doi.org/10.1039/c9ta03201k>.
- [19] Y. Li, Z. Dong, L. Jiao, Multifunctional transition metal-based phosphides in energy-related electrocatalysis, *Adv. Energy Mater.* 10 (2020) 1–36, <https://doi.org/10.1002/aenm.201902104>.
- [20] A.R.J. Kucernak, V.N. Naranammalpuram Sundaram, Nickel phosphide: the effect of phosphorus content on hydrogen evolution activity and corrosion resistance in acidic medium, *J. Mater. Chem. A.* 2 (2014) 17435–17445, <https://doi.org/10.1039/c4ta03468f>.
- [21] A. Parra-Puerto, K.L. Ng, K. Fahy, A.E. Goode, M.P. Ryan, A. Kucernak, Supported transition metal phosphides: activity survey for HER, ORR, OER, and corrosion resistance in acid and alkaline electrolytes, *ACS Catal.* 9 (2019) 11515–11529, <https://doi.org/10.1021/acscatal.9b03359>.
- [22] Y.Y. Ma, C.X. Wu, X.J. Feng, H.Q. Tan, L.K. Yan, Y. Liu, Z.H. Kang, E.B. Wang, Y. G. Li, Highly efficient hydrogen evolution from seawater by a low-cost and stable CoMoP/C electrocatalyst superior to Pt/C, *Energy Environ. Sci.* 10 (2017) 788–798, <https://doi.org/10.1039/c6ee03768b>.
- [23] Y. Liu, P. Xu, Z. Ye, T. Cen, X. Peng, D. Yuan, H. Wu, P. doped CoMoO₄/RGO as an efficient hybrid catalyst for hydrogen evolution, *Int. J. Hydrogen Energy.* 45 (2020) 15157–15165, <https://doi.org/10.1016/j.ijhydene.2020.04.008>.
- [24] Z. Wang, H. Liu, R. Ge, X. Ren, J. Ren, D. Yang, L. Zhang, X. Sun, Phosphorus-Doped Co₃O₄ nanowire array: a highly efficient bifunctional electrocatalyst for overall water splitting, *ACS Catal.* 8 (2018) 2236–2241, <https://doi.org/10.1021/acscatal.7b03594>.
- [25] W. Chu, Z. Shi, Y. Hou, D. Ma, X. Bai, Y. Gao, N. Yang, Trifunctional of phosphorus-doped NiCo₂O₄ nanowire materials for asymmetric supercapacitor, oxygen evolution reaction, and hydrogen evolution reaction, *ACS Appl. Mater. Interfaces.* 12 (2020) 2763–2772, <https://doi.org/10.1021/acscami.9b13182>.
- [26] V.H. Hoa, D.T. Tran, D.C. Nguyen, D.H. Kim, N.H. Kim, J.H. Lee, Molybdenum and phosphorus dual doping in cobalt monolayer interfacial assembled cobalt nanowires for efficient overall water splitting, *Adv. Funct. Mater.* 30 (2020) 1–12, <https://doi.org/10.1002/adfm.202002533>.
- [27] Z. Meng, N. Chen, S. Cai, R. Wang, W. Guo, H. Tang, Co-N-doped hierarchically ordered macro/mesoporous carbon as bifunctional electrocatalyst toward oxygen reduction/evolution reactions, *Int. J. Energy Res.* 45 (2021) 6250–6261, <https://doi.org/10.1002/er.6247>.
- [28] B. Cai, A. Eychmüller, Promoting Electrocatalysis upon Aerogels, *Adv. Mater.* 31 (2019) 1–16, <https://doi.org/10.1002/adma.201804881>.
- [29] R. Du, W. Jin, R. Hübner, L. Zhou, Y. Hu, A. Eychmüller, Engineering Multimetallic aerogels for pH-Universal HER and ORR electrocatalysis, 1903857 (2020). [10.1002/aenm.201903857](https://doi.org/10.1002/aenm.201903857).
- [30] Z. Su, T. Chen, Porous noble metal electrocatalysts: synthesis, *Perform. Dev.*, 2005354 (2021) 1–28, <https://doi.org/10.1002/sml.202005354>.
- [31] W. Liu, P. Rodriguez, L. Borchardt, A. Foelske, J. Yuan, A.K. Herrmann, D. Geiger, Z. Zheng, S. Kaskel, N. Gaponik, R. Köt, T.J. Schmidt, A. Eychmüller, Bimetallic aerogels: High-performance electrocatalysts for the oxygen reduction reaction, *Angew. Chemie - Int. Ed.* 52 (2013) 9849–9852, <https://doi.org/10.1002/anie.201303109>.
- [32] C. Zhu, D. Wen, M. Oschatz, M. Holzschuh, W. Liu, A.K. Herrmann, F. Simon, S. Kaskel, A. Eychmüller, Kinetically controlled synthesis of PdNi bimetallic porous nanostructures with enhanced electrocatalytic activity, *Small* 11 (2015) 1430–1434, <https://doi.org/10.1002/sml.201401432>.
- [33] W. Liu, D. Haubold, B. Rutkowski, M. Oschatz, R. Hu, M. Werheid, C. Ziegler, L. Sonntag, S. Liu, Z. Zheng, A. Herrmann, D. Geiger, B. Terlan, T. Gemming, L. Borchardt, S. Kaskel, A. Czyska-filemonowicz, A. Eychmüller, Self-supporting hierarchical porous PtAg alloy nanotubular aerogels as highly active and durable electrocatalysts, (2016). [10.1021/acs.chemmater.6b01394](https://doi.org/10.1021/acs.chemmater.6b01394).
- [34] L. Liu, L.X. Chen, A.J. Wang, J. Yuan, L. Shen, J.J. Feng, Hydrogen bubbles template-directed synthesis of self-supported AuPt nanowire networks for improved ethanol oxidation and oxygen reduction reactions, *Int. J. Hydrogen Energy.* 41 (2016) 8871–8880, <https://doi.org/10.1016/j.ijhydene.2016.03.208>.
- [35] Q. Shi, C. Zhu, Y. Li, H. Xia, M.H. Engelhard, S. Fu, D. Du, Y. Lin, A facile method for synthesizing dendritic core-shell structured ternary metallic aerogels and their enhanced electrochemical performances, *Chem. Mater.* 28 (2016) 7928–7934, <https://doi.org/10.1021/acs.chemmater.6b03549>.
- [36] C. Zhu, Q. Shi, S. Fu, J. Song, H. Xia, D. Du, Y. Lin, Efficient SYNTHESIS of MCu (M = Pd, Pt, and Au) aerogels with accelerated gelation kinetics and their high Electrocatalytic activity, (2016) 1–5. [10.1002/adma.201602546](https://doi.org/10.1002/adma.201602546).
- [37] K. Deng, T. Ren, Y. Xu, S. Liu, Z. Dai, Z. Wang, X. Li, L. Wang, H. Wang, Transition metal M (M = Co, Ni, and Fe) and boron co-modulation in Rh-based aerogels for highly efficient and pH-universal hydrogen evolution electrocatalysis, *J. Mater. Chem. A.* 8 (2020) 5595–5600, <https://doi.org/10.1039/d0ta00398k>.
- [38] R. Du, J.O. Joswig, R. Hübner, L. Zhou, W. Wei, Y. Hu, A. Eychmüller, Freeze-thaw-promoted fabrication of clean and hierarchically structured noble-metal aerogels for electrocatalysis and photoelectrocatalysis, *Angew. Chemie - Int. Ed.* 59 (2020) 8293–8300, <https://doi.org/10.1002/anie.201916484>.
- [39] R. Du, J. Wang, Y. Wang, R. Hübner, X. Fan, I. Senkovska, Y. Hu, S. Kaskel, A. Eychmüller, Unveiling reductant chemistry in fabricating noble metal aerogels for superior oxygen evolution and ethanol oxidation, *Nat. Commun.* 11 (2020) 1–10, <https://doi.org/10.1038/s41467-020-15391-w>.
- [40] A.A. Dubale, Y. Zheng, H. Wang, R. Hübner, Y. Li, J. Yang, J. Zhang, N.K. Sethi, L. He, Z. Zheng, W. Liu, High-performance bismuth-doped nickel aerogel electrocatalyst for the methanol oxidation reaction, *Angew. Chemie - Int. Ed.* 59 (2020) 13891–13899, <https://doi.org/10.1002/anie.202004314>.
- [41] B. Zhang, F. Yang, X. Liu, N. Wu, S. Che, Y. Li, Phosphorus doped nickel-molybdenum aerogel for efficient overall water splitting, *Appl. Catal. B Environ.* (2021) 298, <https://doi.org/10.1016/j.apcatb.2021.120494>.
- [42] X. Yan, S. Che, F. Yang, Z. Xu, H. Liu, C. Li, L. Yan, N. Ta, S. Sun, Q. Wei, L. Fang, Y. Li, Highly efficient water splitting catalyst composed of N,P-Doped porous carbon decorated with Surface P-Enriched Ni₂P nanoparticles, *ACS Appl. Mater. Interfaces.* (2021), <https://doi.org/10.1021/acscami.1c14363>.

- [43] H. Lin, N. Liu, Z. Shi, Y. Guo, Y. Tang, Q. Gao, Cobalt-doping in molybdenum-carbide nanowires toward efficient electrocatalytic hydrogen evolution, *Adv. Funct. Mater.* 26 (2016) 5590–5598, <https://doi.org/10.1002/adfm.201600915>.
- [44] S. Wang, L. Xiong, J. Bi, X. Zhang, G. Yang, S. Yang, Structural and electronic stabilization of PtNi concave octahedral nanoparticles by P doping for oxygen reduction reaction in alkaline electrolytes, *ACS Appl. Mater. Interfaces*. 10 (2018) 27009–27018, <https://doi.org/10.1021/acsami.8b07742>.
- [45] J. Lin, Y. Yan, C. Li, X. Si, H. Wang, J. Qi, J. Cao, Z. Zhong, W. Fei, J. Feng, Bifunctional electrocatalysts based on Mo-Doped NiCoP nanosheet arrays for overall water splitting, *Nano-Micro Lett* 11 (2019) 1–11, <https://doi.org/10.1007/s40820-019-0289-6>.
- [46] P. Wang, Q. Shao, J. Guo, L. Bu, X. Huang, Promoting alkaline hydrogen evolution catalysis on P-decorated, Ni-Segregated Pt–Ni–P nanowires via a synergetic cascade route, *Chem. Mater.* 32 (2020) 3144–3149, <https://doi.org/10.1021/acs.chemmater.0c00172>.
- [47] J. Ma, M. Wang, G. Lei, G. Zhang, F. Zhang, W. Peng, X. Fan, Y. Li, Polyaniline derived N-Doped carbon-coated cobalt phosphide nanoparticles deposited on N-Doped graphene as an efficient electrocatalyst for hydrogen evolution reaction, *Small* 14 (2018) 1–9, <https://doi.org/10.1002/sml.201702895>.
- [48] Y. Li, S. Guo, T. Jin, Y. Wang, F. Cheng, L. Jiao, Promoted synergy in core-branch CoP@NiFe–OH nanohybrids for efficient electrochemical-/photovoltage-driven overall water splitting, *Nano Energy* 63 (2019), 103821, <https://doi.org/10.1016/j.nanoen.2019.06.017>.
- [49] X. Liu, J. Zang, S. Zhou, P. Tian, H. Gao, S. Song, R. Li, Y. Wang, Electroless deposition of Ni–Cu–P on a self-supporting graphene with enhanced hydrogen evolution reaction activity, *Int. J. Hydrogen Energy*. 45 (2020) 13985–13993, <https://doi.org/10.1016/j.ijhydene.2020.03.102>.
- [50] H. Huang, A. Cho, S. Kim, H. Jun, A. Lee, J.W. Han, J. Lee, Structural design of amorphous CoMoPx with Abundant active sites and synergistic catalysis effect for effective water splitting, *Adv. Funct. Mater.* 30 (2020) 1–9, <https://doi.org/10.1002/adfm.202003889>.
- [51] J. Liu, Y. Gao, X. Tang, K. Zhan, B. Zhao, B.Y. Xia, Y. Yan, Metal-organic framework-derived hierarchical ultrathin CoP nanosheets for overall water splitting, *J. Mater. Chem. A* 8 (2020) 19254–19261, <https://doi.org/10.1039/d0ta07616c>.
- [52] C.Z. Yuan, S.L. Zhong, Y.F. Jiang, Z.K. Yang, Z.W. Zhao, S.J. Zhao, N. Jiang, A. W. Xu, Direct growth of cobalt-rich cobalt phosphide catalysts on cobalt foil: An efficient and self-supported bifunctional electrode for overall water splitting in alkaline media, *J. Mater. Chem. A* 5 (2017) 10561–10566, <https://doi.org/10.1039/c7ta01776f>.
- [53] F. Paquin, J. Rivnay, A. Salleo, N. Stingelin, C. Silva, Multi-phase semicrystalline microstructures drive exciton dissociation in neat plastic semiconductors, *J. Mater. Chem. C* 3 (2015) 10715–10722, <https://doi.org/10.1039/b000000x>.
- [54] L. Jiao, Y.X. Zhou, H.L. Jiang, Metal-organic framework-based CoP/reduced graphene oxide: high-performance bifunctional electrocatalyst for overall water splitting, *Chem. Sci.* 7 (2016) 1690–1695, <https://doi.org/10.1039/c5sc04425a>.
- [55] Q. Guo, J. Mao, J. Huang, Z. Wang, Y. Zhang, J. Hu, J. Dong, S. Sathasivam, Y. Zhao, G. Xing, H. Pan, Y. Lai, Y. Tang, Reducing Oxygen Evolution Reaction Overpotential in Cobalt-Based Electrocatalysts via Optimizing the “Microparticles-in-Spider Web” Electrode Configurations, *Small* 16 (2020) 1–9, <https://doi.org/10.1002/sml.201907029>.
- [56] L. Yang, H. Ren, Q. Liang, K.N. Dinh, R. Dangol, Q. Yan, Ultrathin amorphous nickel doped cobalt phosphates with highly ordered mesoporous structures as efficient electrocatalyst for oxygen evolution reaction, *Small* 16 (2020) 1–7, <https://doi.org/10.1002/sml.201906766>.
- [57] S. Pan, X. Mao, J. Yu, L. Hao, A. Du, B. Li, B. Li, Remarkably improved oxygen evolution reaction activity of cobalt oxides by an Fe ion solution immersion process, *Inorg. Chem. Front.* 7 (2020) 3327–3339, <https://doi.org/10.1039/d0qi00385a>.
- [58] S. Liu, C. Che, H. Jing, J. Zhao, X. Mu, S. Zhang, C. Chen, S. Mu, Phosphorus-triggered synergy of phase transformation and chalcogenide vacancy migration in cobalt sulfide for an efficient oxygen evolution reaction, *Nanoscale* 12 (2020) 3129–3134, <https://doi.org/10.1039/c9nr09203j>.
- [59] C. Wang, Y. Li, C. Gu, L. Zhang, X. Wang, J. Tu, Active Co@CoO core/shell nanowire arrays as efficient electrocatalysts for hydrogen evolution reaction, *Chem. Eng. J.* 429 (2022), 132226, <https://doi.org/10.1016/j.cej.2021.132226>.
- [60] N. Chen, W. Zhang, J. Zeng, L. He, D. Li, Q. Gao, Plasma-Engineered MoP with nitrogen doping: electron localization toward efficient alkaline hydrogen evolution, *Appl. Catal. B Environ.* 268 (2020), 118441, <https://doi.org/10.1016/j.apcatb.2019.118441>.
- [61] F. Ye, Y. Yang, P. Liu, Y. Feng, Y. Cao, D. Cao, L. Ta, X. Ma, C. Xu, In-situ porous flake heterostructured NiCoP/Ni foam as electrocatalyst for hydrogen evolution reaction, *Electrochim. Acta*. 423 (2022), 140578, <https://doi.org/10.1016/j.electacta.2022.140578>.
- [62] F. Xiang, X. Zhou, X. Yue, Q. Hu, Q. Zheng, D. Lin, An oxygen-deficient cobalt-manganese oxide nanowire doped with P designed for high performance asymmetric supercapacitor, *Electrochim. Acta*. 379 (2021), 138178, <https://doi.org/10.1016/j.electacta.2021.138178>.
- [63] X.D. Wang, H.Y. Chen, Y.F. Xu, J.F. Liao, B.X. Chen, H.S. Rao, D. Bin Kuang, C. Y. Su, Self-supported NiMoP2 nanowires on carbon cloth as an efficient and durable electrocatalyst for overall water splitting, *J. Mater. Chem. A* 5 (2017) 7191–7199, <https://doi.org/10.1039/c6ta1188b>.
- [64] H. Yan, Y. Xie, A. Wu, Z. Cai, L. Wang, C. Tian, X. Zhang, H. Fu, Anion-modulated HER and OER activities of 3D Ni–V-based interstitial compound heterojunctions for high-efficiency and stable overall water splitting, *Adv. Mater.* 31 (2019) 1–9, <https://doi.org/10.1002/adma.201901174>.
- [65] C. Xiao, Y. Li, X. Lu, C. Zhao, Bifunctional porous NiFe/NiCo2O4/Ni foam electrodes with triple hierarchy and double synergies for efficient whole cell water splitting, *Adv. Funct. Mater.* 26 (2016) 3515–3523, <https://doi.org/10.1002/adfm.201505302>.
- [66] Y. Jiang, Y. Lu, J. Lin, X. Wang, Z. Shen, A hierarchical MoP nanoflake array supported on Ni Foam: a bifunctional electrocatalyst for overall water splitting, *Small Methods* 2 (2018) 1–10, <https://doi.org/10.1002/smt.201700369>.
- [67] X. Yu, M. Wang, X. Gong, Z. Guo, Z. Wang, S. Jiao, Self-supporting Porous CoP-based films with phase-separation structure for ultrastable overall water electrolysis at large current density, *Adv. Energy Mater.* 8 (2018) 1–10, <https://doi.org/10.1002/aenm.201802445>.
- [68] G. Zhou, M. Li, Y. Li, H. Dong, D. Sun, X. Liu, L. Xu, Z. Tian, Y. Tang, Regulating the electronic structure of CoP Nanosheets by O incorporation for high-efficiency electrochemical overall water splitting, *Adv. Funct. Mater.* 30 (2020) 1–8, <https://doi.org/10.1002/adfm.201905252>.
- [69] X. Yu, Z.Y. Yu, X.L. Zhang, P. Li, B. Sun, X. Gao, K. Yan, H. Liu, Y. Duan, M.R. Gao, G. Wang, S.H. Yu, Highly disordered cobalt oxide nanostructure induced by sulfur incorporation for efficient overall water splitting, *Nano Energy* 71 (2020), 104652, <https://doi.org/10.1016/j.nanoen.2020.104652>.
- [70] Q. Shi, Q. Liu, Y. Ma, Z. Fang, Z. Liang, G. Shao, B. Tang, W. Yang, L. Qin, X. Fang, High-performance trifunctional electrocatalysts based on FeCo/Co2P hybrid nanoparticles for Zinc–Air battery and self-powered overall water splitting, *Adv. Energy Mater.* 10 (2020) 1–11, <https://doi.org/10.1002/aenm.201903854>.

报告编号：2025-2296-1

论文收录引用

检索证明报告

中华人民共和国教育部科技查新站（SH01）

论文作者： 刘洪辰

委托单位： 中国石油大学（北京）

论文发表年限： 2022-2024 年

检索数据库：

SCI-EXPANDED	2001- present	网络版
--------------	---------------	-----

检索结果：（作者提供文章）

1） SCI-E 收录：有 4 篇被收录

（详细结果见附件）

特此证明！

检索报告人：



附件:

一、SCI-E 收录情况

第 1 条, 共 1 条

标题: Electronic synergy between CoP/NiCoP heterostructure and Co, Ni single atoms for efficient hydrogen evolution and overall water splitting

作者: Liu, HC (Liu, Hongchen); Yan, XR (Yan, Xingru); Yang, F (Yang, Fan); Che, S (Che, Sai); Wang, JF (Wang, Jianfeng); Qian, JX (Qian, Jinxiu); Zhang, XY (Zhang, Xiaoyun); Sun, SY (Sun, Siyuan); Sun, Y (Sun, Yang); Wu, N (Wu, Ni); Wang, SY (Wang, Shuyang); Li, YF (Li, Yongfeng)

来源出版物: INTERNATIONAL JOURNAL OF HYDROGEN ENERGY 卷: 56 页: 725-734 DOI: 10.1016/j.ijhydene.2023.12.250 Early Access Date: DEC 2023 Published Date: 2024 FEB 22

Web of Science 核心合集中的 "被引频次": 8

被引频次合计: 9

入藏号: WOS:001151718700001

文献类型: Article

地址: [Liu, Hongchen; Yan, Xingru; Yang, Fan; Che, Sai; Wang, Jianfeng; Qian, Jinxiu; Zhang, Xiaoyun; Sun, Siyuan; Sun, Yang; Wu, Ni; Li, Yongfeng] China Univ Petr, State Key Lab Heavy Oil Proc, Beijing 102249, Peoples R China.

[Wang, Shuyang] Beijing Co, China Petr Engn & Construct Corp, Beijing 100085, Peoples R China.

通讯作者地址: Yang, F; Li, YF (通讯作者), China Univ Petr, State Key Lab Heavy Oil Proc, Beijing 102249, Peoples R China.

电子邮件地址: yangfan@cup.edu.cn; yfli@cup.edu.cn

ISSN: 0360-3199

2024 年期刊的影响因子: 8.3

2025 年期刊中科院分区 (升级版): 大类 材料科学 -2

第 2 条, 共 4 条

标题: Interface and electronic structure regulation of Mo-doped NiSe₂-CoSe₂ heterostructure aerogel for efficient overall water splitting

作者: Liu, HC (Liu, Hongchen); Yang, F (Yang, Fan); Chen, FJ (Chen, Fengjiang); Che, S (Che, Sai); Chen, N (Chen, Neng); Sun, SY (Sun, Siyuan); Ta, N (Ta, Na); Sun, Y (Sun, Yang); Wu, N (Wu, Ni); Sun, YK (Sun, Yankun); Li, YF (Li, Yongfeng)

来源出版物: JOURNAL OF COLLOID AND INTERFACE SCIENCE 卷: 640 页: 1040-1051 DOI: 10.1016/j.jcis.2023.02.154 Early Access Date: MAR 2023 Published Date: 2023 JUN 15

Web of Science 核心合集中的 "被引频次": 39

被引频次合计: 39

入藏号: WOS:000971275000001

文献类型: Article

地址: [Liu, Hongchen; Yang, Fan; Chen, Fengjiang; Che, Sai; Chen, Neng; Sun, Siyuan; Ta, Na; Sun, Yang; Wu, Ni; Sun, Yankun; Li, Yongfeng] China Univ Petr, State Key Lab Heavy Oil Proc, Beijing 102249, Peoples R China.

通讯作者地址: Yang, F; Li, YF (通讯作者), China Univ Petr, State Key Lab Heavy Oil Proc, Beijing 102249, Peoples R China.

电子邮件地址: yangfan@cup.edu.cn; yfli@cup.edu.cn

ISSN: 0021-9797

2024 年期刊的影响因子: 9.7

2025 年期刊中科院分区 (升级版): 大类 化学 1 TOP

第 3 条, 共 4 条

标题: Bimetallic Ni-Co selenide heterostructure aerogel for highly efficient overall water splitting

作者: Liu, HC (Liu, Hongchen); Yang, F (Yang, Fan); Chen, FJ (Chen, Fengjiang); Che, S (Che, Sai); Chen, N (Chen, Neng); Xu, C (Xu, Chong); Wu, N (Wu, Ni); Wei, WK (Wei, Wenkai); Li, YF (Li, Yongfeng)

来源出版物: MATERIALS CHEMISTRY FRONTIERS 卷: 7 期: 7 页: 1365-1373 DOI: 10.1039/d2qm01082h Early Access Date: JAN 2023 Published Date: 2023 MAR 27

Web of Science 核心合集中的 "被引频次": 29

被引频次合计: 29

入藏号: WOS:000930087600001

文献类型: Article

地址: [Liu, Hongchen; Yang, Fan; Chen, Fengjiang; Che, Sai; Chen, Neng; Xu, Chong; Wu, Ni; Wei, Wenkai; Li, Yongfeng] China Univ Petr, State Key Lab Heavy Oil Proc, Beijing 102249, Peoples R China.

通讯作者地址: Yang, F; Li, YF (通讯作者), China Univ Petr, State Key Lab Heavy Oil Proc, Beijing 102249, Peoples R China.

电子邮件地址: yangfan@cup.edu.cn; yfli@cup.edu.cn

eISSN: 2052-1537

2024 年期刊的影响因子: 6.5

2025 年期刊中科院分区 (升级版): 大类 材料科学 3

第 4 条, 共 4 条

标题: P-doped CoCu aerogel as a bifunctional electrocatalyst for efficient overall water splitting

作者: Liu, HC (Liu, Hongchen); Yang, F (Yang, Fan); Xu, ZS (Xu, Zhusong); Yan, XR (Yan, Xingru); Chen, FJ (Chen, Fengjiang); Xu, C (Xu, Chong); Che, S (Che, Sai); Li, YF (Li, Yongfeng)

来源出版物: ELECTROCHIMICA ACTA 卷: 430 文献号: 141075 DOI: 10.1016/j.electacta.2022.141075 Early Access Date: AUG 2022 Published Date: 2022 OCT 20

Web of Science 核心合集中的 "被引频次": 18

被引频次合计: 18

入藏号: WOS:000863278000003

文献类型: Article

地址: [Liu, Hongchen; Yang, Fan; Xu, Zhusong; Yan, Xingru; Chen, Fengjiang; Xu, Chong; Che, Sai; Li, Yongfeng] China Univ Petr, State Key Lab Heavy Oil Proc, Beijing 102249, Peoples R China.

通讯作者地址: Yang, F; Li, YF (通讯作者), China Univ Petr, State Key Lab Heavy Oil Proc, Beijing 102249, Peoples R China.

电子邮件地址: yangfan@cup.edu.cn; yfli@cup.edu.cn

ISSN: 0013-4686

2024 年期刊的影响因子: 5.6

2025 年期刊中科院分区 (升级版): 大类 化学 2

(End)

经委托人确认签字:



主持校科研基金（青年拔尖人才项目）

基本信息			
项目名称	新型碱性电解水催化材料的研发及微观形貌对气体产物生成-解离过程机理的研究	项目编号	ZX20250050
负责人	刘洪辰	负责人职工号	2024880053
负责人类型	本校教师	第二负责人	
所属校区	校本部	所属学院	理学院
项目分类	校基金-师资博士后	项目级别	校级
项目来源单位		经费总额（含税）	40 万元
自筹经费	万元	合作经费	0 万元
立项日期	2025	校内立项年度	2025-01-01
开始日期	2025-01-01	计划结项日期	2028-12-31
计划书中完成时间		委托方合同编号	2462025SZBH003
委托方名称	中国石油大学（北京）	个人备注	
合同基本信息			
合同返还状态	已返还	合同返还日期	2025-03-17
合同登记类型		合同登记编号	
技术合同交易额	万元		
返还合同备注	2025年获批拔尖，追加20万。2025.7.11		

其他科研项目（企业横向课题）

基本信息

合同名称	低成本电解水制氢实验室建设及催化剂创制	合同编号	HX20241192
负责人姓名	刘洪辰	负责人职工号	2024880053
负责人类型	本校教师	负责人电话	18513355916
所属单位	理学院	所属校区	校本部
经费卡别	科研卡	是否按预算执行	否
合同类别	横向非财政-技术咨询	合同经费	30 万元
合作经费	0 万元	进行状态	进行
签订日期	2024-12-01	开始日期	2024-12-01
计划完成日期	2025-11-30	是否用章	是
原单位名称	理学院		

委托方信息

委托方合同编号		委托方名称	河北金盾麟瑞通信科技有限公司
委托方性质	民营企业	委托方地区（一级）	河北省
委托方地区（二级）	石家庄市	境外地区（国家）	